Dissertation

Terahertz spectroscopy of high density electron and hole systems in Si and Ge under the magnetic field and uniaxial stress

（テラヘルツ分光法による磁場下一軸性圧力下におけるSiおよびGeの高密度電子正孔系の研究）

December, 2013

The University of Tokyo
Department of Physics

35 117064　Jeyoon Yoo

Abstract

Photoexcited electron-hole (e-h) systems of semiconductors exhibit various phases depending on the temperature and density. At low density region, due to their Coulomb interaction, an electron and a hole form a bound state like a hydrogen atom, which is referred to as an exciton. Because excitons are approximately recognized as the composite bosons, Bose Einstein condensation (BEC) of exciton has been expected at low temperature. The critical temperature of BEC depends on the mass of particle, degeneracy factor, and the density of particle. With lighter mass, lower degeneracy, and higher density, higher critical temperature will be achieved. Because of their light masses, the exciton BEC is expected to be realized at the critical temperature about three orders of magnitude higher than the hydrogen atom under the same density.

Because excitons are photoexcited quasi-particles composed of electrons and holes, they finally recombine to the ground state, radiatively or non-radiatively, within their finite lifetime. In order to realize such a macroscopic quantum condensate, it is very important that the excitons can cool down below the critical temperature of BEC after the photoexcitation within their finite lifetime. Excitons in Si and Ge have lifetime longer than μs, due to the indirect gap nature. From this merit, we have paid attention to Si and Ge as candidate systems for the exciton BEC. However, in the case of indirect gap semiconductor such as Si or Ge, photoexcited carriers form a e-h droplet (EHD) at low temperature. Once this metallic EHD is formed under the critical temperature of EHD, the accumulation of exciton is prevented. Therefore, the suppression of EHD formation is crucial for the realization of the exciton BEC in Si or Ge. Furthermore, high degeneracy of excitons in Si or Ge reduces the critical temperature of the exciton BEC. These problems can be overcome by the magnetic field and an uniaxial stress.

The formation of EHD is suppressed by uniaxial stress. By applying the uniaxial stress stronger than 300 MPa (100 MPa), the conduction and valence band degeneracy of Si (Ge) [ν_e,ν_h] is reduced from [6,2] to [2,1] (from [4,2] to [1,1]) with results in the suppression of EHD. Correspondingly, the band degeneracy of excitons is also lifted by applying the uniaxial stress. Furthermore, in the presence of the magnetic field, the spin degeneracy of excitons is lifted. In the case of excitons in Si or Ge, the spin degeneracy is lifted by the magnetic field higher than 3 T at 1.6 K.

In this study, we performed the optical pump and terahertz (THz) probe (OPTP) spectroscopy in order to investigate electron-hole system in Si or Ge quantitatively under the uniaxial stress and strong magnetic field. Observation of e-h system in Si and Ge in near-infrared (NIR) regime is difficult because of their indirect transition

nature. THz spectroscopy has shed a new light on this problem recently. From the energy scale of the binding energy of an exciton and the surface plasmon resonance of EHD, we can investigate an exciton and EHD quantitatively by THz spectroscopy.

First, we have investigated the magnetic field effect and the lifetime of the excitons in Si. To lift the spin degeneracy of the excitons, the magnetic field is indispensable. However, the magnetic field effect on the excitons in Si has not fully been resolved. Therefore, we investigated the magnetic field effect by using the photoluminescence and OPTP spectroscopy. Furthermore, to observe the excitons which are accumulated under the magnetic field, we have developed a long-temporal-range OPTP spectroscopy scheme with a quasi-CW optical pump pulse, and investigated the lifetime of the excitons under the magnetic field.

Next, to lift the band degeneracy of excitons, we developed the OPTP spectroscopy scheme under the magnetic field up to 7 T and an uniaxial stress stronger than 300 MPa. For the THz spectroscopy under the uniaxial stress, we have developed an anvil cell. By applying the uniaxial stress, we confirmed that the carrier density inside EHD is largely reduced in Si, indicating the band degeneracy is reduced successfully. Also, EHD in Ge disappeared by applying the uniaxial stress. In this way, we found that the excitons sustain at low temperature below the critical temperature of EHD formation. In the case of Si, the experimental result indicates the exciton population of 3×10^{15} cm^{-3} is accumulated at 1.6 K under 7 T which is about a one-third of critical density of the exciton BEC. Furthermore, the population of the magnetoexcitons in Ge was evaluated as 2.8×10^{15} cm^{-3} at the magnetoexciton temperature of 2.3 K under 4 T. With this density, the phase space density is calculated to be 0.25 and the critical temperature of 0.9 K is expected.

Contents

1 Introduction **5**
- 1.1 Electron and hole system in photoexcited semiconductors 5
  - 1.1.1 Exciton 6
  - 1.1.2 Electron hole droplet 7
- 1.2 Motivation 9
- 1.3 Framework of this thesis 9

2 Optical properties and external field effects on Si and Ge **11**
- 2.1 Optical properties of Si and Ge 11
  - 2.1.1 Si 11
  - 2.1.2 Ge 14
- 2.2 Uniaxial stress 16
  - 2.2.1 Conduction band 16
  - 2.2.2 Valence band 17
  - 2.2.3 Suppression of EHD 19
  - 2.2.4 Previous studies of an uniaxial stress effect 22
- 2.3 Magnetic field effect on exciton 25
  - 2.3.1 Weak field regime 25
  - 2.3.2 Strong field regime 27
  - 2.3.3 Previous studies of the magnetic field effect 30
- 2.4 Exciton BEC 33

3 Experimental methods **37**
- 3.1 Broadband terahertz spectroscopy 37
  - 3.1.1 Emission of THz wave 37
  - 3.1.2 Detection of THz wave 38
- 3.2 Experimental Setup 40
  - 3.2.1 Optical pump - THz probe spectroscopy system 40
  - 3.2.2 Superconducting magnet 45
  - 3.2.3 Vacuum pump for single shot method 47
- 3.3 Spectral analysis 49
- 3.4 THz spectroscopy system under the uniaxial stress 50
  - 3.4.1 Pressure anvil cell for OPTP measurement under the uniaxial stress 50
- 3.5 Polarization measurement method 51

4 The magnetic field effect and lifetime measurement of the excitons in Si under the ambient pressure 55
4.1 Evaluation of the impurity concentration . . . 55
4.2 The magnetic field effect . . . 57
4.2.1 PL spectroscopy . . . 57
4.2.2 OPTP spectroscopy . . . 60
4.3 Quasi-CW pump and THz probe spectroscopy . . . 62
4.3.1 Pile up and relaxation dynamics of free carriers at room temperature . . . 64
4.4 Lifetime measurement of exciton by OPTP spectroscopy . . . 65
4.5 Lifetime of spin-forbidden excitons . . . 69
4.6 Summary . . . 70

5 Electron and hole system under the magnetic field and uniaxial stress in Si 71
5.1 Photoexcited dynamics of e-h system in stressed-Si . . . 72
5.2 Excitation power dependence . . . 75
5.3 Density of the excitons under the magnetic field . . . 79
5.4 Summary . . . 83

6 Electron and hole system under the magnetic field and an uniaxial stress in Ge 85
6.1 Sample and experimental setup . . . 85
6.2 Evaluation of e-h pair density at high temperature under the uniaxial stress . . . 86
6.3 Intra-exciton transition and suppression of EHD at low temperature under the uniaxial stress . . . 87
6.4 Cyclotron resonance of free carriers under the uniaxial stress . . . 88
6.5 Magnetoexcitons in the low density regime . . . 91
6.5.1 Magnetic field dependence . . . 91
6.5.2 Temperature dependence under the magnetic field . . . 93
6.6 Evaluation of the temperature of magnetoexcitons . . . 96
6.7 Formation dynamics of the magnetoexcitons . . . 97
6.8 Magnetoexcitons in high density regime . . . 100
6.8.1 Invalidity of the OPTP spectroscopy under the magnetic field 100
6.8.2 Excitation power dependence . . . 101
6.9 Summary . . . 110

7 Summary and Outlook 112
7.1 Summary . . . 112
7.2 Outlook . . . 113

A Diffusion of excitons 114

Reference 116

Chapter 1

Introduction

1.1 Electron and hole system in photoexcited semiconductors

The property of photoexcited e-h system in semiconductors depends on the temperature and the density. At low temperature and low density region, an e-h pair forms a bound state by Coulomb interaction, which is referred to as exciton. Since excitons are charge neutral quasiparticles, the exciton gas system is insulating. When the pair density increases, the Coulomb interaction between the electron and the hole is screened, and the excitons are dissociated into unbound electrons and holes, resulting in a metallic electron-hole plasma (EHP) phase. This phase transition or crossover is referred to as "Mott transition" after N. F. Mott [1]. In the case of indirect semiconductors such as Si or Ge, the e-h liquid phase is stabilized at high density and low temperature, which usually takes the form of e-h droplet (EHD). Furthermore, at very low temperature, the quantum degenerated states such as the Bose Einstein condensation (BEC) of excitons or e-h BCS has been anticipated to exist theoretically [2]. Figure 1.1 shows the phase diagram of the e-h system in Si [3]. In Fig. 1.1, the blue dotted line (aqua dotted-dashed line) represents the Mott transition density calculated by Debye-Hückel theory (random phase approximation). The pink dashed line is represents the critical curve for the exciton BEC by assuming that the exciton is an ideal boson, the red solid line is the coexistence curve of the excitons and the EHDs, indicating that the emergence of the exciton BEC in Si is prevented due to the formation of EHD. One can see that the BEC phase locates deep inside the coexistence curve of EHD. However, as we will discuss later, the coexistence region can be largely suppressed by applying an uniaxial stress. In this chapter, we describe about the basic formalism of the excitons and the EHDs.

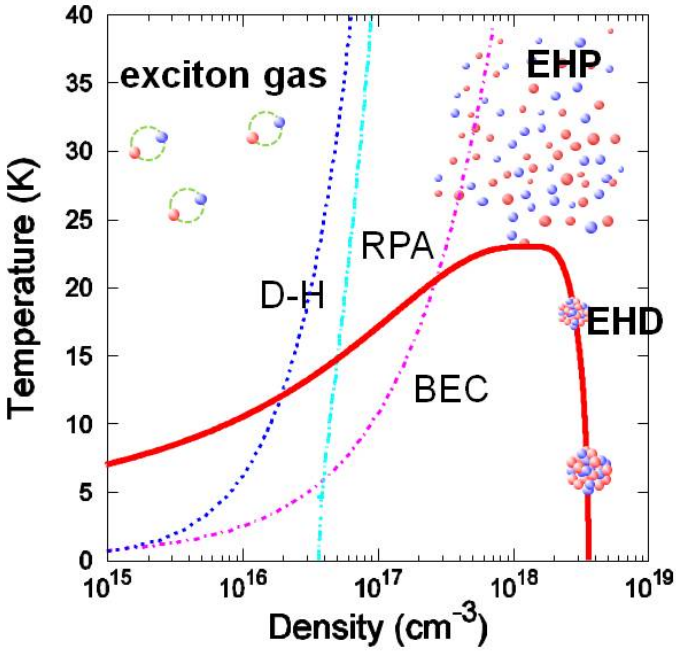

Figure 1.1: Phase diagram of electron and hole system in Si. The blue dotted line (aqua dotted-dashed line) represents the critical curve of Mott transition calculated by Debye-Hückel theory (random phase approximation), the pink dashed line is the critical curve of the exciton BEC, the red solid line is the coexistence curve of exciton and e-h droplet [3].

1.1.1 Exciton

In photoexcited semiconductors, an electron and a hole attract each other by Coulomb interaction, and form a bound state which is referred to as "exciton". An exciton is a charge neutral composite particle, which obeys approximately the Bose-Einstein statics. The exciton is analogous to the hydrogen atom while the Coulomb interaction is screened as, $\frac{1}{4\pi\epsilon_0}\frac{e^2}{\epsilon_b r}$, where ϵ_b is the relative background dielectric constant. The eigenenergies of exciton are given by

$$E_j^{exc} = E_g - \frac{e^4\mu}{2\hbar^2\epsilon_b^2 j^2} \ . \tag{1.1}$$

Here、$j = 1, 2, 3\ldots$ is the quantum number,

$$\frac{1}{\mu} = \frac{1}{m_e} + \frac{1}{m_h} \tag{1.2}$$

represents the reduced mass of exciton. In the case of Si, $\mu = 0.123\ m_0$ [4], $\epsilon_b = 11.7$, and the binding energy of exciton is as small as 14.7 meV. Likewise, in the case of Ge, with $\mu = 0.046\ m_0$ and $\epsilon_1 = 15.6$, and the binding energy of exciton is 4.2 meV.

Bohr radius $a_B = \hbar^2\epsilon/\mu e^2$, the reduced mass, and the binding energy of an exciton in Si and Ge are shown in Table 1.1.

	a_B(nm)	μ/m_0 [4]	E_b(meV) [5]
Si	4.9	0.123	14.7
Ge	11	0.046	4.2

Table 1.1: Parameters of exciton in Si and Ge

1.1.2 Electron hole droplet

In the case of the indirect gap semiconductor, e-h pairs are spatially condensed into electron-hole droplets (EHDs) at high density and low temperature. The total energy per e-h pair in the e-h system ϵ_g is represented by the sum of kinetic (ϵ_k), exchange (ϵ_x), and correlation (ϵ_c) energies, i. e., $\epsilon_g = \epsilon_k + \epsilon_x + \epsilon_c$. When ϵ_g is lower than exciton binding energy, EHD becomes the ground state.

In the case of isotropic two bands (electrons and holes) model, with the equal electron and hole masses, the kinetic and exchange energies are given by

$$\epsilon_k = \frac{3}{5}\left(\frac{k_F^2}{2m_e} + \frac{k_F^2}{2m_h}\right) = \frac{3}{5}\frac{9\pi}{4}^{2/3}\frac{1}{r_s^2} = \frac{2.21}{r_s^2} \tag{1.3}$$

$$\epsilon_x = -\frac{3e^2}{2\pi\kappa}k_F = -\frac{3}{\pi}\frac{9\pi}{4}^{1/3}\frac{1}{r_s} = -\frac{1.832}{r_s}\ , \tag{1.4}$$

where k_F is the Fermi momentum and $r_s = r/a_B$ is the dimensionless parameter with $(4\pi/3)r^3 = 1/n$ (n is the density of electrons (holes)), which describes interparticle distance normalized by the Bohr radius [6].

Further, by considering the real band structure of Si and Ge such as degeneracy and anisotropy, the sum of kinetic and exchange energies has been calculated as [6]

$$\epsilon_k + \epsilon_x = \frac{0.727}{r_s^2} - \frac{1.157}{r_s} \quad \text{(for Si)}\ , \tag{1.5}$$

$$= \frac{0.468}{r_s^2} - \frac{1.136}{r_s} \quad \text{(for Ge)}\ . \tag{1.6}$$

In contrast, the exact form of the correlation energy cannot be obtained. Brinkman and Rice calculated the correlation energy by using the single-component electron gas approximation which is proposed by Hubbard [6]. The calculated values of correlation energy at different r_s for Si and Ge are shown in Table. 1.2

Besides, Vashishta *et al*. found that the sum of the exchange and the correlation energies of EHD can be fitted by [7]

$$\epsilon_x(r_s) + \epsilon_c(r_s) = \frac{a + br_s}{c + dr_s + r_s^2}\ . \tag{1.7}$$

with a = -4.8316, b = -5.0879, c = 0.0152, and d = 3.0426.

Figure 1.2 shows the calculated ground state energies ϵ_g for Si and Ge by the Hubbard approximation (HA) and fully self-consistent approximation (FSC), with

	$r_s = 0.5$	1.0	1.5	2.0	2.5
Si	-1.64	-1.12	-0.89	-0.76	-0.65
Ge	-1.52	-1.07	-0.86	-0.73	-0.64

Table 1.2: Correlation energy for Si and Ge [6].

(ANISO) and without (ISO) the anisotropy in the conduction band. The existence of energy minimum below the binding energy of the exciton indicates that the ground state of e-h system is an e-h liquid phase.

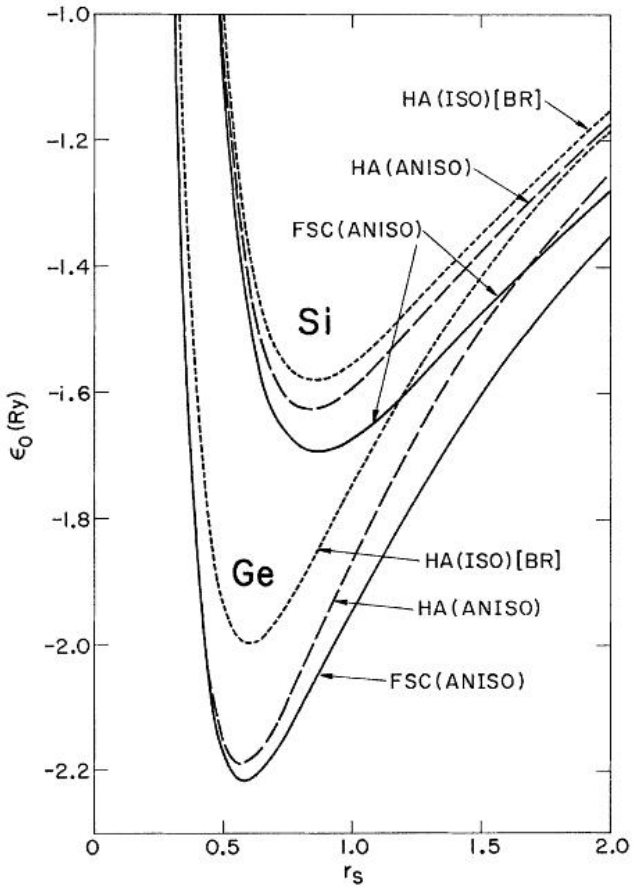

Figure 1.2: Ground state energy ϵ_g of e-h system in Si and Ge as a function of normalized inter-particle distance, r_s. The vertical axis is plotted in the unit of exciton binding energy [8].

The calculated carrier density and the work function of EHD for Si and Ge are represented in Table 1.3. For details of calculation, see Ref. [6].

	Si	Ge
n_{EHD}	3.4×10^{18} cm^{-3}	1.8×10^{17} cm^{-3}
ϕ	5.7 meV	1.7 meV

Table 1.3: Ground state parameter for Si and Ge [6]

1.2 Motivation

The e-h systems in Si or Ge are very intriguing object from the standpoint of the quantum degenerated phases because of the long lifetime of photoexcited e-h pairs. However, the existence of stable EHD phase prevents the realization of the quantum degenerated phases such as exciton BEC and e-h BCS. To overcome this intrinsic difficulty, we tried to suppress the formation of EHD by applying an uniaxial stress to the crystals. Furthermore, to lift the spin degeneracy of excitons, which should increase the critical temperature of BEC, and also to realize the quantum limit where both electrons and holes stay in the lowest Landau levels in the high density region above the Mott density, we applied the magnetic field to the crystals. To realize the quantitative investigation of photoexcited dynamics, exciton fine structure and the evaluation of densities of the excitons and the free carriers, we introduced a newly developed spectroscopy technique of terahertz (THz) time-domain spectroscopy. In particular, we developed the optical pump and THz probe measurement system under the uniaxial stress and strong magnetic field.

1.3 Framework of this thesis

The framework of this thesis is as follows;

In Chapter 2, we explain the physical background of this study. The optical properties of Si and Ge, the excitons and the EHD are described. Furthermore, the uniaxial stress effect and the magnetic field effect are explained with examples of previous reports. The exciton BEC is briefly introduced.

In Chapter 3, we introduce the experimental method used in this study. The generation and detection of THz wave, the experimental setup and the analysis methods are described. Also, the developments of the experimental techniques for low temperature and uniaxial stress are described.

In Chapter 4, we describe the measurement of the magnetic field effect on the excitons in Si under ambient pressure. We observed $1S$ exciton by photoluminescence spectroscopy and intra-exciton transition by optical pump and THz probe spectroscopy. Exciton lifetime is also discussed. By developing the quasi-continuous-wave optical pump and THz probe spectroscopy system, we performed the lifetime measurement of e-h system in Si in μs temporal region. Finally, we discuss about the lifetime of spin-forbidden (triplet) excitons in Si through the magnetic field dependence.

In Chapter 5, the e-h system in uniaxially-stressed Si is discussed. Under the uniaxial stress, we observed the suppression of EHD formation at low temperature. Also, we applied the magnetic field to crystal to lift the spin degeneracy. From the spectral analysis, we evaluate the maximum density of excitons accessible under the uniaxial stress and the magnetic field.

In Chapter 6, the e-h system in uniaxially-stressed Ge is discussed. Under the strong magnetic field limit, we performed the measurement of the magnetoexcitons. Furthermore, we discuss about the high density excitation phenomena of magnetoexcitons, based on the THz polarization measurement.

Finally, we conclude the thesis with summary and outlook in Chapter 7.

Chapter 2

Optical properties and external field effects on Si and Ge

In this Chapter, we describe about the uniaxial stress effect and the magnetic field effect on the e-h systems. Then, we describe the expected phase diagram of exciton BEC in Si and Ge.

2.1 Optical properties of Si and Ge

The effect of the uniaxial stress can be described by the deformation of the band structure. Here, we introduce the band structures and the band parameters of Si and Ge.

2.1.1 Si

Band structure

The crystal structure of Si is a diamond cubic. Figure 2.1 shows the band structure of Si by local-pseudopotential calculation [9]. As shown in Fig 2.1, Si is an indirect gap semiconductor where the energy maximum in the valence and minimum in the conduction bands do not exist at the same momentum.

The energy maximum of the valence band exists at Γ point and the principal conduction band minima are located along the [100], [010], and [001] directions at a distance of about 85 % from the Γ point to the X points. The band gap at Γ point is 4.185 eV [10] and the indirect gap is 1.1558 eV at 4 K [11]. The interband transition of the indirect gap must be phonon-assisted transition due to the momentum conservation, and as a result the transition probability becomes small compared to the direct transition.

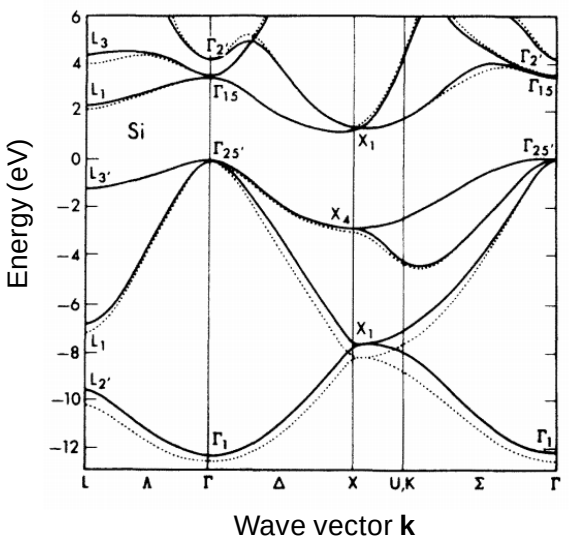

Figure 2.1: Band structure of Si [9].

Conduction band

Let set the direction of X axis as the main axis of the vector $\mathbf{k}$ and set the origin $\mathbf{k} = 0$ is at the energy minimum in conduction band. The energy of the conduction band is written by

$$E(\mathbf{k}) = \frac{\hbar^2}{2m_t}(k_x^2 + k_y^2) + \frac{\hbar^2}{2m_l}k_z^2 \ . \tag{2.1}$$

Here, m_t and m_l represent the transverse mass and longitudinal mass, respectively. Then, the constant-energy surface of the conduction band is represented in Fig. 2.2. It is called multi-valley structure, and the constant-energy surface around the minima of the conduction band is plural as shown in Fig. 2.2.

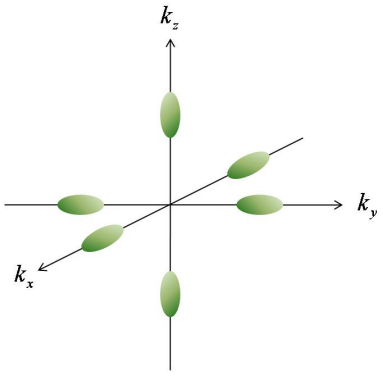

Figure 2.2: Multiple valley structure of conduction band in Si

When we calculate the density of state for single band with anisotropic masses, the density of state mass m_{de} is used which is defined by the geometric mean of masses. Also in the dielectric function and the optical conductivity, the harmonic mean of masses is used, which is called the optical mass m_{oe}. In the case of conduction band in Si, the density of state mass and the optical mass are given by

$$m_{de} = m_t^{2/3} m_l^{1/3} \ , \tag{2.2}$$

$$\frac{1}{m_{oe}} = \frac{2}{m_t} + \frac{1}{m_l} \ . \tag{2.3}$$

Valence band

The maximum of the valence band with $J = 3/2$ exists at Γ point. From the $\mathbf{k} \cdot \mathbf{p}$ perturbation, in the vicinity of $\mathbf{k} = 0$, the energy of $J = 3/2$ hole is given by [12]

$$E(\mathbf{k}) = -\frac{\hbar^2}{2m_0}[Ak^2 \pm \sqrt{B^2k^4 + C^2(k_x^2k_y^2 + k_y^2k_z^2 + k_z^2k_x^2)}] \ , \tag{2.4}$$

where A, B, and C is the inverse mass band parameter. Here, the sign of square root term indicates either heavy or light hole (the positive case is the light hole and the negative case is the heavy hole).

Besides, the energy of the $J = 1/2$ hole is also given by [12]

$$E(\mathbf{k}) = -Ak^2 + E_{SO} \ , \tag{2.5}$$

with the spin-orbit splitting energy E_{SO}.

The band parameters of Si are summarized in Table 2.1.

Physical quantity	Symbol	Value	Unit	Reference
Conduction band parameters				
Longitudinal mass	m_l	0.9163	m_0	[6]
Transverse mass	m_t	0.1905	m_0	[6]
Density of state mass	m_{de}	0.32	m_0	[6]
Optical mass	m_{oe}	0.26	m_0	[6]
Valence band parameters				
Heavy hole mass	m_{hh}	0.523	m_0	[6]
Light hole mass	m_{lh}	0.153	m_0	[6]
A		4.28		[6]
B		0.75		[6]
C		4.85		[6]
Spin-orbit splitting	E_{SO}	44	meV	[13]

Table 2.1: The band parameters for Si

2.1.2 Ge

Band structure

Ge is also an indirect gap semiconductor. Since Ge has larger permittivity compared to that of Si, the binding energy of the excitons becomes smaller than Si. The energy maximum of the valence band and the energy minimum of the conduction band of Ge are located at Γ point and L point, respectively.

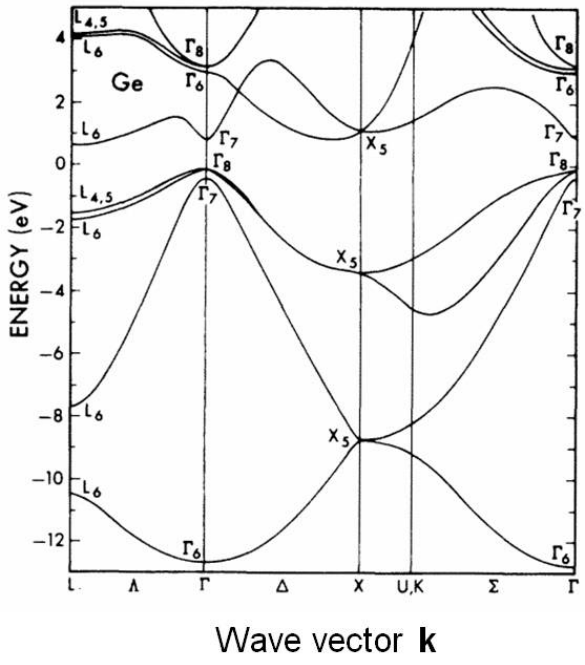

Figure 2.3: Band structure of Ge [9].

In the case of Ge, the energy difference between the direct gap at Γ point and the indirect gap is relatively small ($E_g^{\text{direct}} = 0.898$ eV and $E_g^{\text{indirect}} = 0.744$ eV at 1.5 K [14]). Figure 2.3 shows the band structure of Ge. The formalism of effective masses is same as the case of Si. We summarize the band parameters in Table 2.2.

Physical quantity	Symbol	Value	Unit	Reference
Conduction band parameters				
Longitudinal mass	m_l	1.58	m_0	[6]
Transverse mass	m_t	0.082	m_0	[6]
Density of state mass	m_{de}	0.22	m_0	[6]
Optical mass	m_{oe}	0.12	m_0	[6]
Valence band parameters				
Heavy hole mass	m_{hh}	0.347	m_0	[6]
Light hole mass	m_{lh}	0.042	m_0	[6]
A		13.38		[6]
B		8.48		[6]
C		13.15		[6]
Spin-orbit splitting	E_{SO}	282	meV	[15]

Table 2.2: The band parameters for Ge

2.2 Uniaxial stress

Based on the band structure, we describe the effect of uniaxial stress on the crystals. The uniaxial stress effect can be understood by introducing the deformation potential Hamiltonian. Here, we describe about the calculation reported by Balslev [16] by using formalism introduced by Herring and Vogt [17] for the conduction band, and the calculation reported by Kelso [18]. Then we introduce the previous studies of the uniaxial stress effect on the e-h systems in Si and Ge.

2.2.1 Conduction band

The degenerated-valley of conduction band is split by applying uniaxial stress. With the dilatation deformation potentials Σ_d and uniaxial deformation potentials Σ_u, introduced by Herring and Vogt [17], the energy shift of valley vi is described by [16]

$$\Delta E_c^{vi} = \Sigma_d \mathbf{I} \cdot \epsilon + \Sigma_u \{\mathbf{a}_i, \mathbf{a}_i\} \cdot \epsilon \ , \tag{2.6}$$

where $\mathbf{I}$ denotes the unit tensor, $\mathbf{a}_i$ is unit vector parallel to the $\mathbf{k}$ vector of valley, $\{\ \}$ is a dyadic product, and ϵ is the second-rank stress tensor. The mean energy shift of the band minimum is given by

$$\Delta E_c^0 = \left(\Sigma_d \mathbf{I} + \frac{1}{3} \Sigma_u \right) \cdot \epsilon \ . \tag{2.7}$$

The valley splitting introduced by applying the uniaxial stress can be obtained by $\Delta E_c^{spl} = \Delta E_c^{vi} - \Delta E_c^0$. The energy shifts of conduction band in the uniaxially-stressed Si along <100> direction and Ge along <111> direction are shown in Table

$< 001 >$-stressed Si		$< 111 >$-stressed Ge	
Valley	ΔE_c^{spl}	Valley	ΔE_c^{spl}
$< 00 \pm 1 >$	$\frac{2}{3}(S_{11} - S_{12})\Sigma_u T$	$< 111 >$	$\frac{1}{3}S_{44}\Sigma_u T$
$< \pm 100 >, < 0 \pm 10 >$	$-\frac{1}{3}(S_{11} - S_{12})\Sigma_u T$	$< -111 >, < 1 - 11 >, < 11 - 1 >$	$-\frac{1}{9}S_{44}\Sigma_u T$

Table 2.3: Energy shift of conduction band valley in uniaxially-stressed Si and Ge [16].

2.3. In Table 2.3, the representation of stress T and compliance coefficients S_{11},S_{12}, and S_{44} are used. In the case of Si, the conduction band degeneracy is lifted to 4 by the uniaxial stress along <110>, and is not lifted by the uniaxial stress along <111>. In Ge, it is lifted to 2 by the uniaxial stress along <110>, and not lifted by the uniaxial stress along <100>.

2.2.2 Valence band

From the $\mathbf{k} \cdot \mathbf{p}$ perturbation formalism, under the uniaxial stress, the energy dispersion of the valence band near $\mathbf{k} = 0$ is given by [18]

$$E(k) = Ak^2 + |E_{\epsilon\epsilon}| \pm (E_{kk}^2 + E_{\epsilon k}^2 + E_{\epsilon\epsilon}^2)^{1/2} \ , \tag{2.8}$$

where

$$E_{\epsilon\epsilon}^2 = \frac{1}{2}b^2[(\epsilon_{xx} - \epsilon_{yy})^2 + (\epsilon_{yy} - \epsilon_{zz})^2 + (\epsilon_{zz} - \epsilon_{xx})^2] + d^2(\epsilon_{xy}^2 + \epsilon_{yz}^2 + \epsilon_{zx}^2) \tag{2.9}$$

$$E_{kk}^2 = B^2k^4 + C^2(k_x^2k_y^2 + k_y^2k_z^2 + k_z^2k_x^2) \tag{2.10}$$

$$\begin{aligned} E_{\epsilon k}^2 \ &= Bb[3(k_x^2\epsilon_{xx} + k_y^2\epsilon_{yy} + k_z^2\epsilon_{zz}) - k^2(\epsilon_{xx} + \epsilon_{yy} + \epsilon_{zz})] &(2.11)\\ &\quad +2Dd(k_xk_y\epsilon_{xy} + k_yk_z\epsilon_{yz} + k_zk_x\epsilon_{zx}) &(2.12)\end{aligned}$$

with A, B, and C the inverse mass parameters [19], $D^2 = 3B^2 + C^2$, b and d the deformation potential, ϵ_{ij} the components of the strain tensor [20]. Equations 2.9 and 2.12 can be deformed in the presence of <001> stress,

$$E_{\epsilon\epsilon} = \frac{b\sigma_{001}}{C_{11} - C_{12}} \tag{2.13}$$

$$E_{\epsilon k}^2 = BE_{\epsilon\epsilon}(3k_z^2 - k^2) \ , \tag{2.14}$$

and, for <111> stress,

$$E_{\epsilon\epsilon} = \frac{d\sigma_{111}}{2\sqrt{3}C_{44}} \tag{2.15}$$

Splitting	Si	Ge
$-E^h_{\rm spl}/\sigma_{001}$	0.272 meV mm^2/kgf	0.528 meV mm^2/kgf
$-E^h_{\rm spl}/\sigma_{111}$	0.218 meV mm^2/kgf	0.362 meV mm^2/kgf

Table 2.4: Energy splitting between heavy hole and light hole band in Si and Ge [18].

$$E^2_{\epsilon k} = \frac{2}{\sqrt{3}} D E_{\epsilon\epsilon}(k_x k_y + k_y k_z + k_z k_x) \ . \tag{2.16}$$

Here, σ_{klm} represents the stress along $< klm >$ direction, and C_{ij} are the stiffness constants. In contrast to the ambient pressure case (eq.2.5), the label of valence band is represented by quantum number M_J instead of heavy and light hole. The energy splitting $E^h_{\rm spl} = 2|E_{\epsilon\epsilon}|$ between the $M_J = \pm 3/2$ and the $M_J = \pm 1/2$ band is shown in Table 2.4.

Furthermore, when the valence bands become ellipsoidal under the complete band splitting in the infinite stress limit, the longitudinal and the transverse mass can be described as

$$m_l = \frac{1}{A+B} m_0 \tag{2.17}$$

$$m_{t1} = m_{t2} = \frac{1}{A - B/2} m_0 \ , \tag{2.18}$$

for <001> stress,

$$m_l = \frac{1}{A + D/\sqrt{3}} m_0 \tag{2.19}$$

$$m_{t1} = m_{t2} = \frac{1}{A - D/2\sqrt{3}} m_0 \ , \tag{2.20}$$

for <111> stress, respectively. Table 2.5 shows the effective masses of the e-h system in <001>-stressed Si and <111>-stressed Ge.

	m_{el}	m_{et}	m_{oe}	m_{de}	m_{hl}	m_{ht}	m_{oh}	m_{dh}	μ
Si	0.9163	0.1905	0.2588	0.3216	0.198	0.256	0.234	0.235	0.123
Ge	1.58	0.082	0.120	0.2198	0.040	0.130	0.075	0.088	0.046

Table 2.5: Effective masses of the e-h system for Ge [1,1] and Si [2,1] in unit of m_0 [21]

	Critical temperature	Density
<100> Si	21.8 K	4.47×10^{16} cm^{-3}
<111> Ge	4.9 K	1.11×10^{16} cm^{-3}

Table 2.6: The critical temperature and the carrier density inside EHD in <100>-stressed Si and <111>-stressed Ge [22].

2.2.3 Suppression of EHD

As discussed in Chapter 1, the ground energy of EHD is determined by the kinetic, exchange, and correlation energies of the e-h pairs. Therefore, when the band degeneracy is lifted under the uniaxial stress, the kinetic energy term increases and the ground state energy of EHD is changed.

With considering the conduction band degeneracy and mass anisotropy, the kinetic and exchange energies are deformed as [22]

$$\epsilon_k = \frac{2.2099}{r_s^2}\left(\frac{\mu}{\nu^{2/3}m_{de}} + \frac{\mu}{m_{dh}}\right) \epsilon_x = \frac{0.9163}{r_s}(\nu^{-1/3}\phi(\rho_e) + \phi(\rho_h)) \ , \tag{2.21}$$

where

$$\phi(\rho) \quad = \rho^{1/6}\left(\frac{\sin^{-1}[(1-\rho)^{1/2}]}{(1-\rho)^{1/2}}\right) \quad \text{for } \rho < 1 \tag{2.22}$$

$$= \rho^{1/6}\left(\frac{\sinh^{-1}[(\rho-1)^{1/2}]}{(\rho-1)^{1/2}}\right) \quad \text{for } \rho > 1 \ . \tag{2.23}$$

Here, μ is the reduced mass, m_{de} (m_{dh}) is the density of state mass of the electrons (holes), ν is the degeneracy factor of the conduction band, and $\rho = m_t/m_l$ is the ratio of the transverse and the longitudinal masses. In the case of <100>-stressed Si and <111>-stressed Ge, the sum of the kinetic and exchange energies are calculated by [22]

$$\epsilon_k + \epsilon_x \quad = \frac{1.6846}{r_s^2} - \frac{1.6052}{r_s} \quad \text{for } < 100 > \text{Si} \tag{2.24}$$

$$= \frac{1.6180}{r_s^2} - \frac{1.6594}{r_s} \quad \text{for } < 111 > \text{Ge} \ . \tag{2.25}$$

With the calculation of the correlation energy by the analogous method to the one-component plasma, the critical temperature and the density of EHD in stressed Si and Ge are calculated as shown in Table 2.6.

To confirm the lifting of the band degeneracy, we calculated the Fermi surface of the electrons in EHD for Ge. It can be calculated from the energy of electrons eq. 2.1 is equal to the Fermi energy. Figures 2.4(a) and (b) show the change of the Fermi surface of electrons in EHD by the uniaxial stress of 500 MPa along <111>

direction, viewing from $(k_x, k_y, k_z) = (1, -1, 0)$. For the ambient pressure and under 500 MPa, the Fermi energy of 3.2 meV and 0.8 meV were used, respectively each of which corresponds to the reported value of the Fermi energy inside the EHD [23]. For ambient pressure, eight degenerated valleys are identified. In contrast, under the uniaxial stress, the bands which exist at $< k_x k_y k_z >$ = <111> and <-1-1-1>, split from other bands with the splitting energy of $S_{44} \sum_u T$ as shown in Fig. 2.4(b). Since these Fermi surfaces are around the L point, one can see that the electrons occupy only one split band.

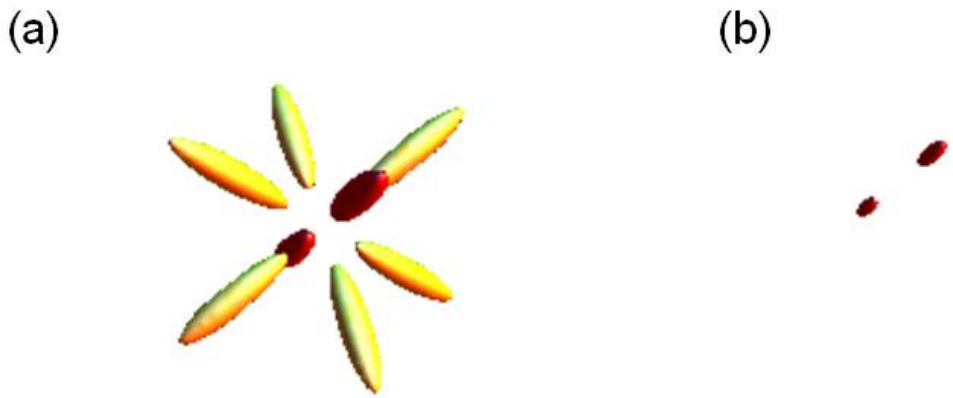

Figure 2.4: The Fermi surfaces of the electrons in Ge under (a) ambient pressure (b) 500 MPa along <111> direction. The viewing angle is $(k_x, k_y, k_z) = (1, -1, -0)$.

Likewise, the Fermi surface of holes can be calculated by the energy of holes eq.2.8. With the Fermi energy of 4.2 meV and 1.9 meV which correspond to the hole Fermi energy inside the EHD under the ambient pressure and under 500 MPa [23], the Fermi surface of the holes in EHD was calculated as shown in Figs. 2.5(a) and (b). In Figs. 2.5(a) and (b), the viewing point is $(k_x, k_y, k_z) = (1.5, 0.7, 0.7)$. In the case of ambient pressure, both Fermi surface of the heavy hole (outside) and the light hole (inside) exist. Under 500 MPa, the Fermi surface of heavy hole disappears and only that of light hole sustains at $E_{\mathrm{F}} = 1.9$ meV. By taking into account the fact that the conduction bands of <111> and <-1-1-1> are equivalent, the band degeneracy of Ge can be reduced from [4,2] to [1,1] with applying the stress along <111>.

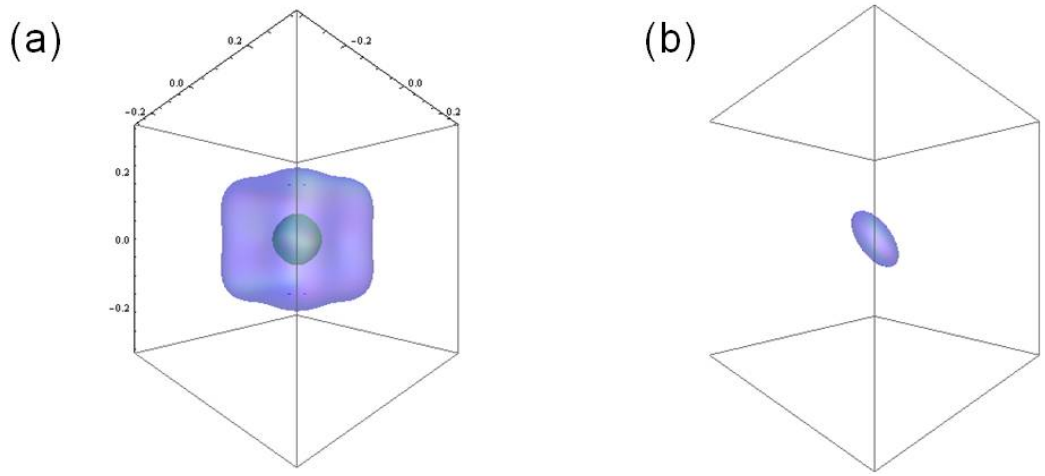

Figure 2.5: The Fermi surfaces of the holes in Ge under (a) ambient pressure (b) 500 MPa along <111> direction. The viewing angle is $(k_x, k_y, k_z) = (1.5, 0.7, 0.7)$.

2.2.4 Previous studies of an uniaxial stress effect

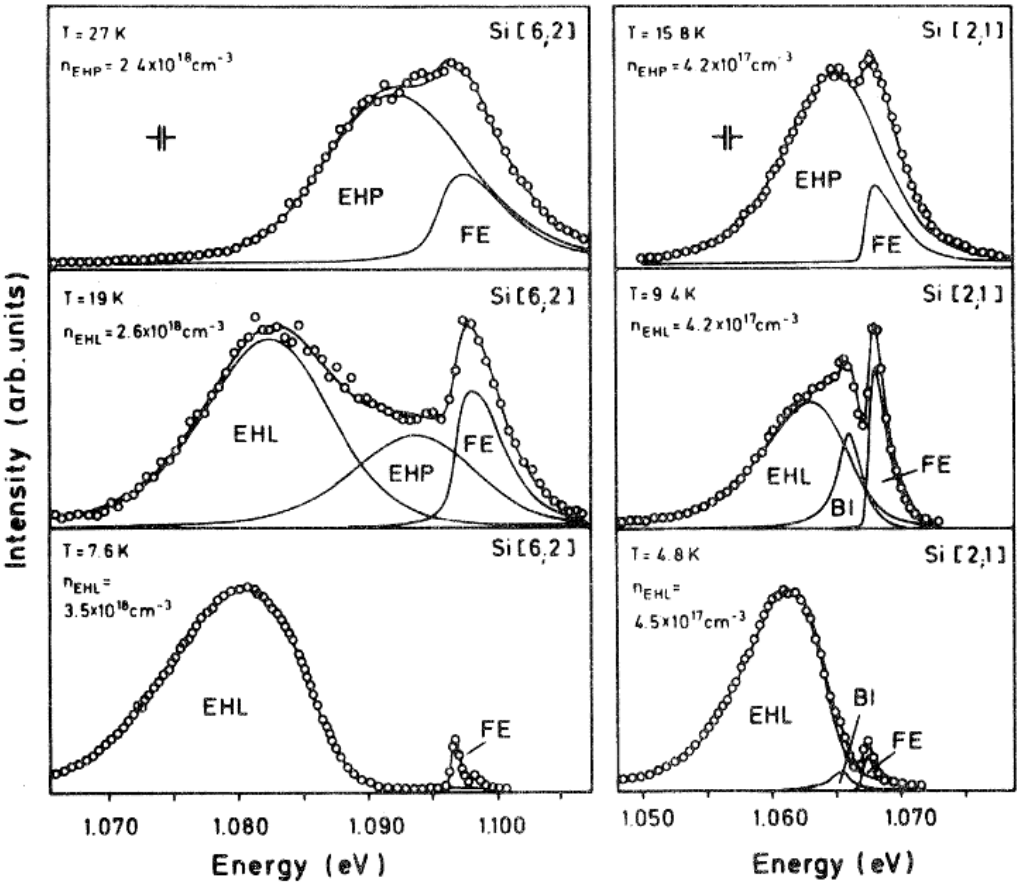

Figure 2.6: PL spectra of unstressed Si and uniaxially-stressed Si along <100> direction [24].

Forchel *et al*. measured the uniaxial stress effect in Si by the PL spectroscopy [24]. Figure 2.6 shows the PL spectra of unstressed Si and uniaxially-stressed Si along <100> direction at different temperature [24]. The band degeneracy factor is represented in Fig. 2.6 as $[\nu_e,\nu_h]$, where ν_e denotes the band degeneracy factor of the conduction band and ν_h is that of the valence band. The magnitude of the stress was about 370 MPa. In the case of unstressed Si, the peaks of the e-h plasma (EHP) and the exciton (FE) are observed at high temperature. With the decrease of the temperature, the peak of EHD (EHL) appears and EHP disappears. On the other hand, under the uniaxial stress, the PL spectrum changes significantly. In the case of stressed Si, first, the biexciton (BI) appears at low temperature. The biexciton is a molecule which is consisted of two excitons. Second, the energies of all components decrease (Note that the horizontal axis range is different with the spectra of the unstressed case). It is attributed to the narrowing of the energy gap by the uniaxial stress. Third, the energy separation between the EHD and the

free exciton decreases, indicating that the work function of EHD is reduced by the uniaxial stress. From the spectral analysis, the carrier density inside the EHD was evaluated as 3.5×10^{18} cm^{-3} at the ambient pressure and 4.5×10^{17} cm^{-3} under the uniaxial stress. The reduction of critical temperature from 29 K to 17.4 K and the work function of the EHD from 7.4 meV to 1.95 meV due to the uniaxial stress have been reported [24].

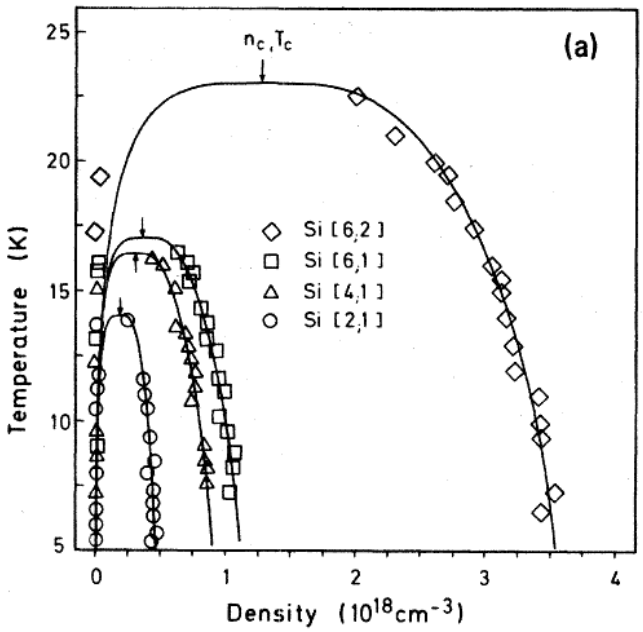

Figure 2.7: Change of the coexistence curves of excitons and EHD in Si under the uniaxial stress with different direction [24].

Figure 2.7 shows the coexistence curve of the unstressed Si as well as under that the different stress directions. From Fig. 2.7, one can see that the coexistence curve shrinks by the uniaxial stress. Furthermore, the shrinking of the coexistence curve is the most noticeable with the stress along <100> direction, which is appropriate for our purpose.

Simon *et al.* performed the PL spectroscopy of uniaxially-stressed Ge along <111> direction. Figure 2.8(a) shows the PL spectra of EHD with the different magnitude of the stress. The peak energy of EHD decreases from 709 to 643 meV and the density of EHD also decreases from 2.1×10^{17} cm^{-3} to 9.8×10^{15} cm^{-3} with the stress of 87 kgf/mm^2 ($\sim$ 850 MPa). The stress-dependence of the carrier density inside EHD is shown in Fig. 2.8(b). The experimental result is in good agreement with the calculation by fully self-consistent approximation and Wigner-type contribution form reported by Kelso [25].

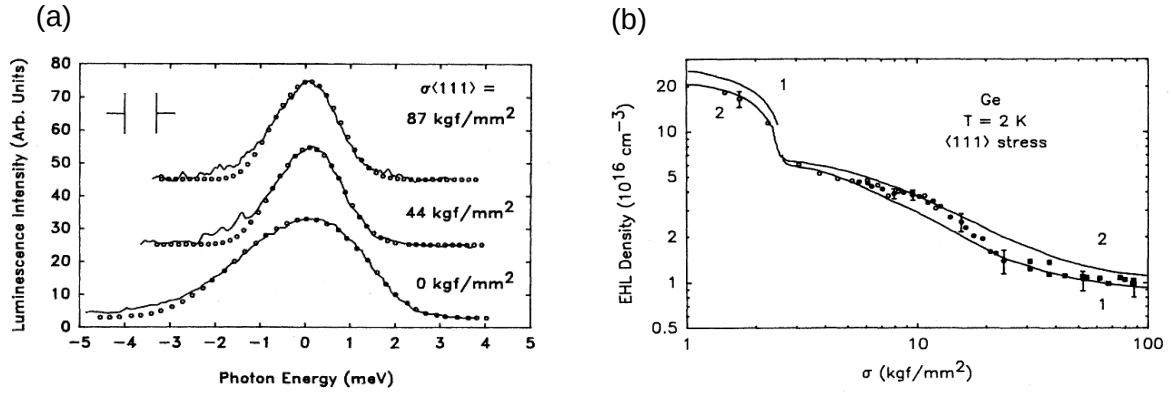

Figure 2.8: PL spectra of uniaxially-stressed Ge along <111> direction [23]. (b) Density of EHD in uniaxially-stressed Ge as a function of the uniaxial stress [23].

Labrie *et al*. observed the intra transition of the excitons in stressed-Si and -Ge with high resolution by far-infrared absorption spectroscopy [26, 27]. Figure 2.9(a) shows the infrared absorption spectra of the excitons in Si under the uniaxial stress of 580 MPa along <001> direction [26]. The upper side of Fig. 2.9(a) shows the spectra with the polarization of probe beam perpendicular to the stress direction and the lower side shows the spectra with the polarization of the probe beam parallel to the stress axis. Furthermore, spectra under both high-excitation and low-excitation are shown. By changing the polarization of the probe beam, the splitting of $nP_0 - nP_\pm$ is clearly resolved where the subscript 0 and $\pm$ denote the angular momentum of nP exciton $m = 0$ and $m = \pm 1$. From the excitation dependence of the peaks A - D, these peaks are assigned to biexcitons. Figure 2.9(b) shows the infrared absorption spectra of the excitons in Ge with different values of uniaxial stress of along <111> direction [27]. In Fig. 2.9(b), the polarized probe beam is also used. The stress dependence of the transition energies are measured from 90 to 370 MPa. From the extrapolation of the stress dependence of $1S$ to $2P$ transition energy, the transition energies are evaluated as 2.09 and 2.02 meV for $1S$-$2P_0$ and $1S$-$2P_\pm$, respectively.

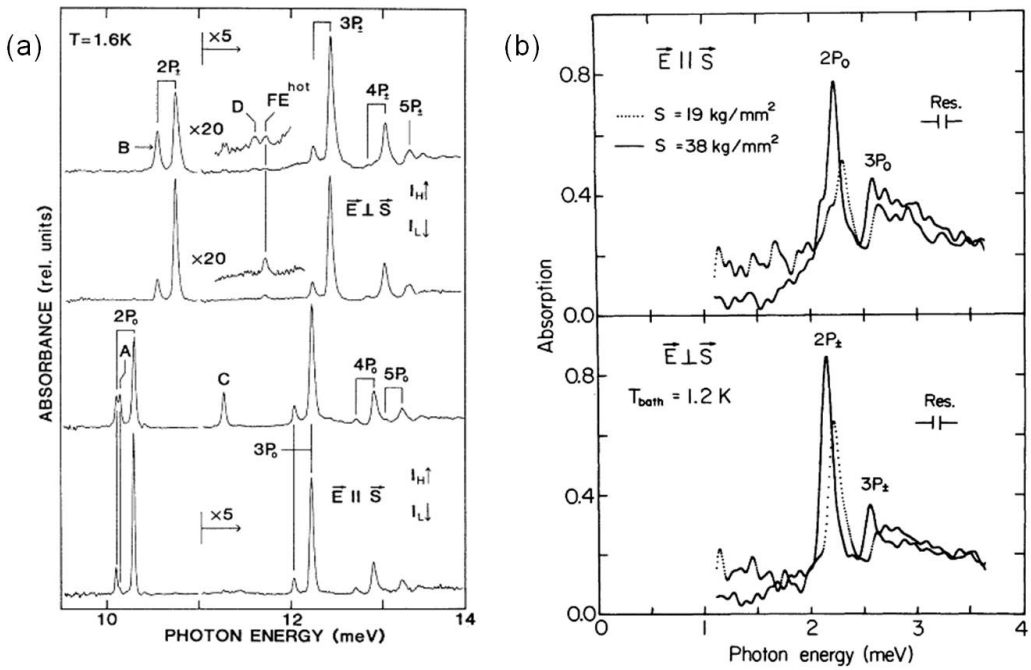

Figure 2.9: The infrared absorption spectra in (a) stressed-Si [26] and (b) -Ge [27].

2.3 Magnetic field effect on exciton

As the indication of the strength of the magnetic field, we introduce a dimensionless parameter

$$\gamma = \frac{\frac{1}{2}\hbar\omega_c}{R_y^*} = \frac{\hbar^3\epsilon^2}{m^{*2}e^3}B_0 \ . \tag{2.26}$$

When $\gamma \ll 1$, the effect of the magnetic field can be treated by perturbation. In contrast, the region of $\gamma \gg 1$ is called as the strong magnetic field regime in which the Coulomb interaction is treated as a perturbation to the Landau-quantized states. In the case of $1S$ excitons in Si, $\gamma \geq 1$ requires the magnetic field higher than 30 T. In contrast, for $1S$ excitons in Ge, γ exceeds 1 with the magnetic field above 3 T [28]. Hence, for our experimental condition (0 to 7 T), we can access only the weak field limit in the case of Si, whereas we can study both the weak and strong limit in the case of Ge.

2.3.1 Weak field regime

First, we consider the case that the magnetic field effect is substantially small in terms of the exciton binding energy. The energy level of exciton under the magnetic field

$$\mathbf{A}(\mathbf{r}) = \frac{1}{2}(\mathbf{B}_0 \times \mathbf{r}) \tag{2.27}$$

is derived from the effective mass equation

$$\left(\frac{1}{2m_e}[\mathbf{P}_e - e\mathbf{A}(\mathbf{r}_e)]^2 + \frac{1}{2m_h}[\mathbf{P}_h - e\mathbf{A}(\mathbf{r}_h)]^2 - \frac{e^2}{4\pi\epsilon_0\epsilon|\mathbf{r}|}\right)\psi = E\psi \ , \tag{2.28}$$

with A the vector potential, $\mathbf{r}_e$ ($\mathbf{r}_h$) the coordinate of an electron (a hole), and m_e (m_h) the mass of an electron (a hole). By the writing the wave function with separation of variables

$$\psi(\rho, \mathbf{r}) = \exp\{i[K - \frac{e}{\hbar}\mathbf{A}(\mathbf{r})] \cdot \rho\}\phi(\mathbf{r}) \ , \tag{2.29}$$

with the center of mass coordinate ρ and the relative coordinate $\mathbf{r}$

$$\rho = \frac{m_e^*\mathbf{r}_e + m_h^*\mathbf{r}_h}{m_e^* + m_h^*} \tag{2.30}$$

$$\mathbf{r} = \mathbf{r}_e - \mathbf{r}_h \ , \tag{2.31}$$

eq. 2.28 will be deformed as

$$[-\frac{\hbar^2}{2\mu}\nabla^2 - \frac{e^2}{4\pi\epsilon_0\epsilon r} - \frac{e}{2}(\frac{1}{m_e^*} - \frac{1}{m_h^*})\mathbf{B}_0 \cdot \mathbf{L} + (g_e\mu_B\mathbf{S}_e + g_h\mu_B\mathbf{J}_h) \cdot \mathbf{B}_0 + \\ + \frac{e^2(x^2+y^2)}{8\mu}B_0^2 - \{\frac{\hbar\mathbf{K}}{(m_e^*+m_h^*)} \times \mathbf{B}_0\} \cdot \mathbf{r}]\phi = [\varepsilon - \frac{\hbar^2K^2}{2(m_e^*+m_h^*)}]\phi \ . \tag{2.32}$$

Here、 $\mu = (1/m_e^* + 1/m_h^*)^{-1}$ refer to the reduced mass of exciton and $\mathbf{L} = \mathbf{r} \times (\hbar/i)\nabla$ is the angular momentum operator, and $\mathbf{K}$ is the center of mass momentum. Fourth and fifth term of LHS in eq. 2.32 represent the Zeeman splitting and diamagnetic shift, respectively.

The value of g-factor of the conduction band in Si is $g_e = 1.99875$ [29]. With the assumption $g_h = 2$, the Zeeman splitting of the 1S excitons in Si is calculated as

$$\mu_B(g_eS_z + g_hJ_z)B_0 = \begin{cases} \pm 1.2 \times 10^{-1}B_0 \text{ (meV)} & \text{for } |\pm\frac{1}{2}, \mp\frac{3}{2}\rangle \\ \pm 2.3 \times 10^{-1}B_0 \text{ (meV)} & \text{for } |\pm\frac{1}{2}, \pm\frac{3}{2}\rangle \end{cases} \ . \tag{2.33}$$

with $|S_z, J_z\rangle$. Likewise, with $g_e = 1.0$ and $g_h = 4$ for exciton in Ge [30], the Zeeman splitting of the 1S excitons in Ge can be calculated as

$$\mu_B(g_eS_z + g_hJ_z)B_0 = \begin{cases} \pm 3.2 \times 10^{-1}B_0 \text{ (meV)} & \text{for } |\pm\frac{1}{2}, \mp\frac{3}{2}\rangle \\ \pm 3.8 \times 10^{-1}B_0 \text{ (meV)} & \text{for } |\pm\frac{1}{2}, \pm\frac{3}{2}\rangle \end{cases} \ . \tag{2.34}$$

Here, with the zero spin of crystal ground state (no optical excitation), we followed the definition that the photoexcited electron and hole have opposite spin. Then, due to the selection rule, an exciton composed by parallel spin e-h pair is optically-forbidden (spin-forbidden). From eqs. 2.33 and 2.34, one knows that the spin-forbidden exciton state exists below the lowest optically-allowed exciton state

S_z	J_z	Zeeman coefficient (meV/T)		Selection rule
		Si	Ge	
$\frac{1}{2}$	$\frac{3}{2}$	2.3×10^{-1}	3.8×10^{-1}	Forbidden
$-\frac{1}{2}$	$\frac{3}{2}$	1.2×10^{-1}	3.2×10^{-1}	Allowed
$\frac{1}{2}$	$-\frac{3}{2}$	-1.2×10^{-1}	-3.2×10^{-1}	Allowed
$-\frac{1}{2}$	$-\frac{3}{2}$	-2.3×10^{-1}	-3.8×10^{-1}	Forbidden

Table 2.7: Zeeman coefficients and selection rule for optical transition of exciton states in Si and Ge under the magnetic field.

under the magnetic field. The schematic of energy level splitting of excitons by the magnetic field is shown in Fig. 2.10. Additionally, the coefficient of diamagnetic shift is calculated as 0.9×10^{-2} (meV/T^2) for Si and 1.2×10^{-1} (meV/T^2) for Ge. Calculated Zeeman coefficients and selection rule for optical transition of each combination of electron and hole states are shown in Table 2.7.

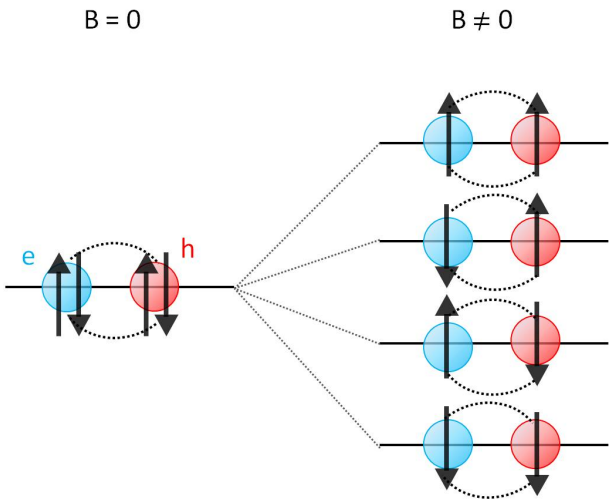

Figure 2.10: The schematic of energy levels of excitons with and without the magnetic field.

2.3.2 Strong field regime

In the strong magnetic field limit, the energy levels of an electron and a hole become discrete, and form Landau levels. Then, the contribution of the magnetic field plays a main role in the Hamiltonian, and the Coulomb interaction between an electron and a hole can be treated by perturbation. An exciton under such strong magnetic field is called "magnetoexciton". Equation 2.35 shows the effective mass Hamiltonian of the magnetoexciton [31, 32].

$$\mathcal{H}_{\rm ex} = -\frac{\hbar^2}{2\mu_t}(\nabla_x^2+\nabla_y^2)-\frac{\hbar^2}{2\mu_l}\nabla_z^2-\frac{ie\hbar}{2}(\frac{1}{m_{et}}-\frac{1}{m_{ht}})\mathbf{B}_0\cdot(\mathbf{r}\times\nabla)+\frac{e^2}{8\mu_t}(\mathbf{B}_0\times\mathbf{r})^2-(\frac{e^2}{4\pi\epsilon_0\epsilon r}) \ . \tag{2.35}$$

Here, μ_t (μ_l) denotes the transverse (longitudinal) reduced mass of exciton, and m_{et} (m_{ht}) is the transverse mass of an electron (a hole), as detected in terms of the direction of the magnetic field.

In the absence of Coulomb interaction term, $-e^2/4\pi\epsilon_0\epsilon r$, the wavefunction is analytically obtained, separating the motion parallel (z-axis) and perpendicular to the $\mathbf{B}_0$, as [31]

$$\Psi_{NM}(\rho,\phi)\frac{1}{\sqrt{L_z}}\exp(ikz) \tag{2.36}$$

$$= \left[\frac{(N-M)!}{2\pi l_B^2 L_z (N!)^3}\right](-i)^2\exp(iM\phi)\sigma^{M/2}\exp(-\sigma/2)L_N^M(\sigma) \tag{2.37}$$

$$\times\exp(ikz)\ (M\geq 0)$$

$$= \left[\frac{N!}{2\pi l_B^2 L_z (N-M)!^3}\right](-i)^2\exp(iM\phi)\sigma^{-M/2}\exp(-\sigma/2)L_{N-M}^{-M}(\sigma) \tag{2.38}$$

$$\times\exp(ikz)\ (M\leq 0)\ ,$$

where N is Landau quantum number which takes zero or positive integer, M is the angular quantum number which is integer in the range $-N\leq M\leq N$, $l_B=\sqrt{\hbar/eB_0}$ is the magnetic length, $\sigma=\rho^2/2l_B^2$ and L_z is the length of the crystal along the direction of the magnetic field, and $L_N^M(\sigma)$ is associated Laguerre polynomial. Here, the cylindrical coordinate (ρ,ϕ,z) was used with the direction of the magnetic field is along z.

However, in the presence of Coulomb interaction term, the Schrödinger equation cannot be solved analytically in 3 dimensional case. Elliott and Loudon have shown that the equation can be solved by introducing the effective Coulomb potential $V_{NM}(z)$ as [33, 31],

$$\left[-\frac{\hbar^2}{2\mu}\frac{d}{dz^2}+V_{NM}(z)\right]\zeta_{NM}^{\lambda}(z)=E_c^{NM\lambda}\zeta_{NM}^{\lambda}(z)\ , \tag{2.39}$$

where

$$V_{NM}(z)=-\int\int\Psi_{NM}^*(\rho,\phi)\frac{e^2}{4\pi\epsilon_0\epsilon\sqrt{\rho^2+z^2}}\Psi_{NM}(\rho,\phi)\rho d\rho d\phi\ . \tag{2.40}$$

λ is related to the quantum number of excitons in the direction of the magnetic field [31, 32]. Then, the eigenvalue of magnetoexciton is written by

$$E^{NM\lambda}=e\hbar B_0\left[\frac{1}{\mu_t}\left(N+\frac{1}{2}\right)-\frac{1}{m_{ht}}M\right]+E_c^{NM\lambda}\ . \tag{2.41}$$

In the case of 2 dimensional system, however the z-component vanishes from Schrödinger equation of exciton eq. 2.35. Then the Coulomb corrections (magnetoexcitons) with center of mass momentum $\mathbf{K}$ can be expressed by [34]

$$E_{NM}(\mathbf{K}) = -\langle NM|\frac{e^2}{4\pi\epsilon_0\epsilon|\mathbf{r}+\mathbf{r}_0|}|NM\rangle \ , \tag{2.42}$$

where

$$\mathbf{r}_0 = \left[\frac{\mathbf{B}_0}{B_0}\times\mathbf{K}\right]\frac{1}{eB_0} \ . \tag{2.43}$$

The results of calculation of eq. 2.42 for $(NM) = (00), (01), (10)$ are shown in Fig. 2.11(a). The dispersion relations for the magnetoexcitons near $K = 0$ are asymptotically quadratic to K,

$$E_{00}(K) \sim -E_0 + \frac{K^2}{2M_{00}} \ , \tag{2.44}$$

$$E_{10}(K) \sim -\frac{1}{2}E_0 + \frac{K^2}{2M_{10}} \ , \tag{2.45}$$

where $M_{00} = 2\hbar^2/E_0 l_B^2$ and $M_{10} = -2M_{00}$ [34, 35]. Due to the negative effective mass of the magnetoexciton $|10\mathbf{K}\rangle$, the transition energy from $|00\mathbf{K}\rangle$ to $|10\mathbf{K}\rangle$,

$$E_{00\to 10} = \hbar\omega_{ce} + \frac{1}{2}E_0 - \frac{K^2}{2M_{00}}(1+\frac{M_{00}}{|M_{10}|}) \tag{2.46}$$

decreases with increasing K

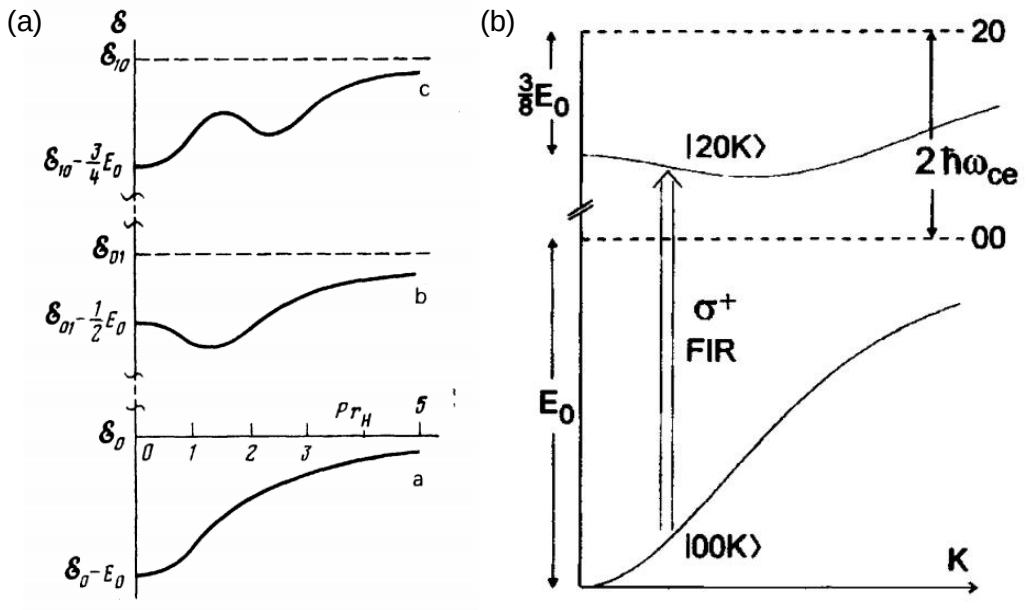

Figure 2.11: The magnetoexciton dispersion in 2 dimension [34]. (b) The intra-transition of the magnetoexcitons [35].

2.3.3 Previous studies of the magnetic field effect

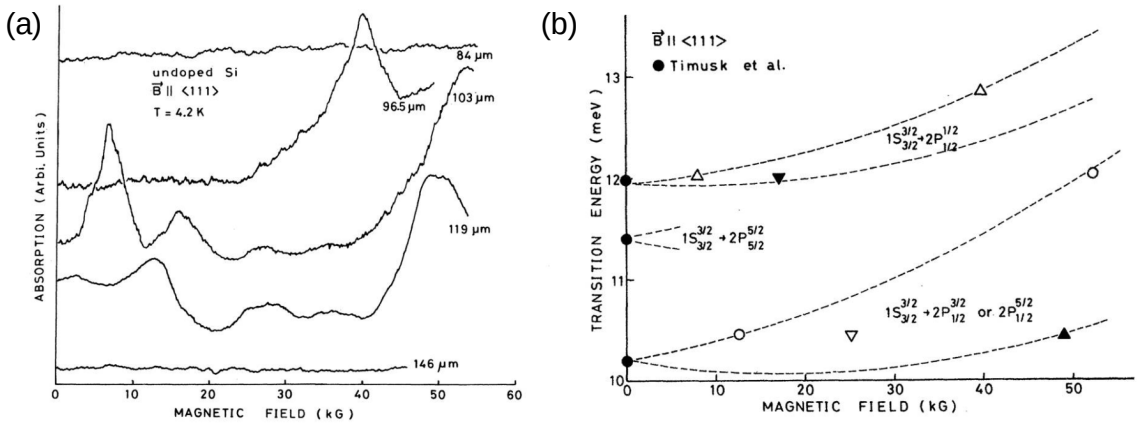

Figure 2.12: (a) The magnetoabsorption spectra of intra-exciton transition in Si with different probe wavelengths. (b) The magnetic field dependence of $1S - 2P$ transition energies of the excitons [36].

Ohyama *et al.* measured the magnetic field effect of the intra-exciton transition in Si by the magnetoabsorption measurement with infrared gas laser [36]. Figure 2.12(a) shows the magnetoabsorption spectra with different probe wavelengths. The magnetic field was applied along <111> direction. Measured absorptions are plotted in Fig. 2.12(b) as a function of the magnetic field. In Fig. 2.12(b), the exciton state is represented by the $nL^F_{F_z}$) which is introduced by Lipari and Altarelli [5], where n is the quantum number and $\mathbf{F} = \mathbf{L} + \mathbf{J}$ is the sum of the angular momentum of the exciton envelope function (**L**)and the total spin of the hole (**J**) corresponding to the valence-band degeneracy. To explain the magnetic field effect on the energy of the intra-exciton transition, a magnetic-field-dependent energy

$$E = a^F + b^F_{F_z} B_0 + c^F_{F_z} B_0^2. \tag{2.47}$$

was used in the fitting. In eq. 2.47, the coefficients $b^F_{F_z}$ and $c^F_{F_z}$ correspond to the magnitude of the Zeeman splitting and the diamagnetic effect on 1S to 2P transition of excitons, respectively. The coefficients $b^F_{F_z}$ was estimated to 0.062 and 0.15 meV/T for $1S^{3/2}_{\pm 3/2} \rightarrow 2P^{1/2}_{\pm 1/2}$ and $1S^{3/2}_{\pm 3/2} \rightarrow (2P^{3/2}_{\pm 1/2}, 2P^{5/2}_{\pm 1/2})$, respectively. Besides, the coefficient $c^F_{F_z}$ was obtained as 0.041 meV/T^2.

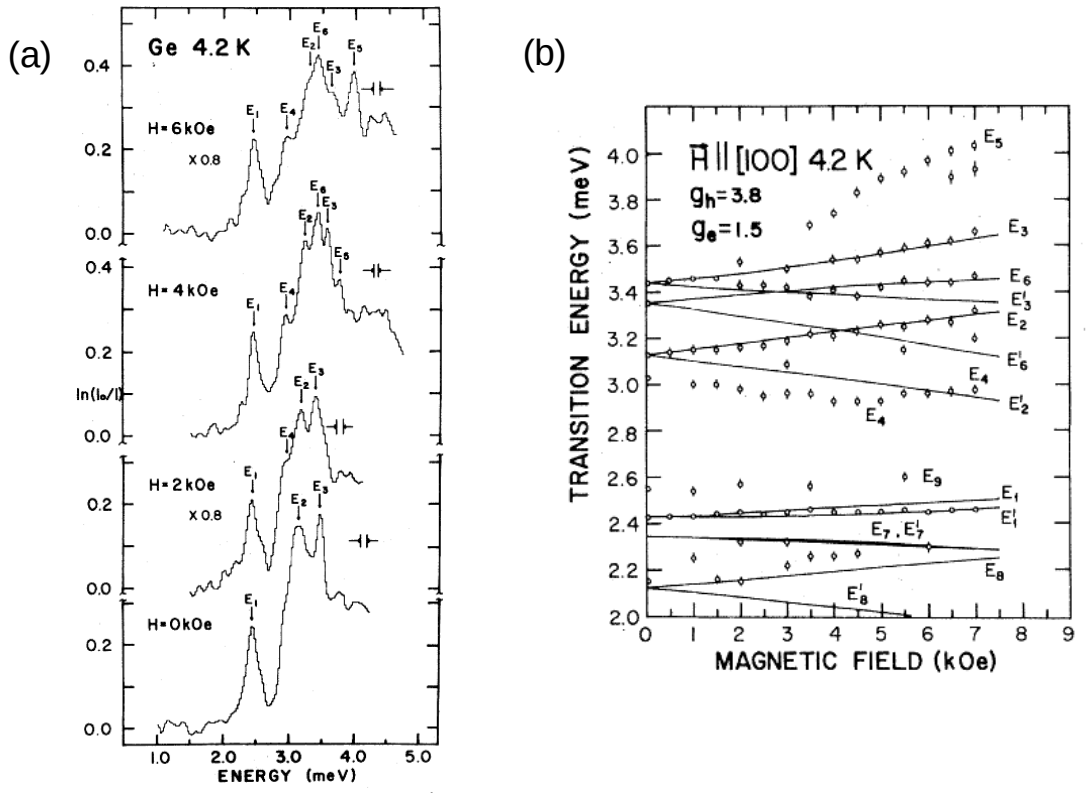

Figure 2.13: (a) Far-infrared absorption spectra of Ge under the magnetic field. The magnetic field was applied along <100> direction. (b) The magnetic field dependence of the intra-exciton transition energy. [37]

Navarro and Timusk measured the Zeeman effect of the excitons in Ge by far-infrared absorption measurement [37]. The magnetic field was applied along <100> direction and the range of the magnetic field was 0 to 0.7 T which can be treated by the perturbation theory. Figure 2.13(a) shows the far-infrared absorption spectra under the magnetic field. At zero magnetic field, three peaks E_1, E_2, and E_3 are observed. Under the magnetic field, more absorption peaks can be seen labeled E_1 to E_6 due to the fine structure of the excitons. The magnetic field dependence of each absorption is plotted in Figure 2.13(b) as a function of the magnetic field. The magnetic field dependence was explained by the Zeeman splitting

$$H_z(B_0) = -g_e \mathbf{L} \cdot \mathbf{B}_0 + g_h \mathbf{F} \cdot \mathbf{B}_0 - g_e \mathbf{S}_e \cdot \mathbf{B}_0 \tag{2.48}$$

with the $\mathbf{F}$ representation which is already described in the magnetic field effect in Si. The effect of the diamagnetic shift was neglected due to the weak magnetic field range. With the theoretical calculation which took into account the anisotropy of both conduction and valence bands, and the degeneracy of valence band, reported by Lipari *et al.* [38], each absorption peak were assigned as shown in Fig. 2.14.

From the fitting by using eq. 2.48, the authors found the values of g-factor as $g_e = 1.5 \pm 0.3$ and $g_h = 3.8 \pm 0.2$.

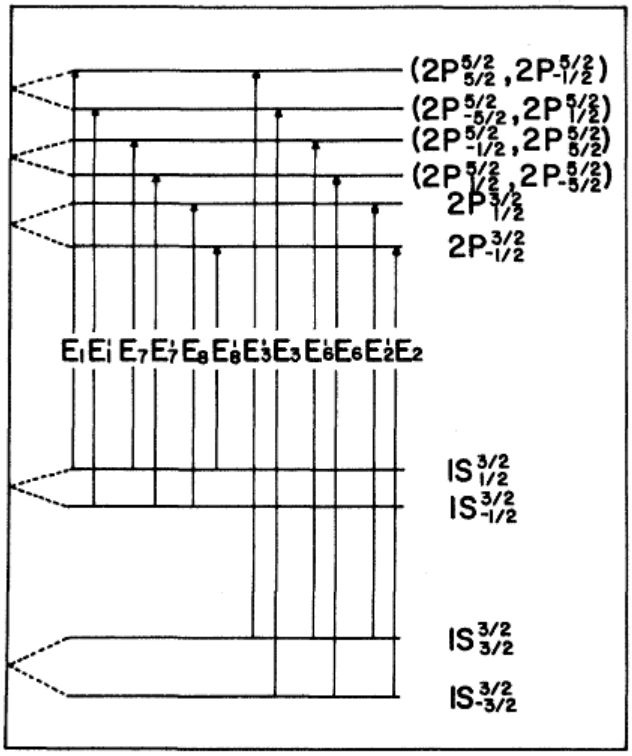

Figure 2.14: Identification of each transition observed in Fig. 2.13. [37]

Besides, Timofeev *et al.* performed the PL spectroscopy on stressed-Ge under the magnetic field with the stresses along <001> and <111> direction, [30]. Figure 2.15(a) shows the phase diagram for (1) unstressed Ge, (2) <111>-stressed Ge (400 MPa), and (3) <∼001>-stressed Ge (300 MPa) under zero magnetic field. The critical curve of Mott transition for unstressed and stressed Ge are also shown by the dotted-dashed lines a and b, respectively. The authors argued that the EHD can be suppressed more efficiently by applying the uniaxial stress along <001> direction than along <111>, as much as the band degeneracy of the conduction band is not resolved. Figure 2.15(b) shows the PL spectra of uniaxially-stressed Ge under the magnetic field. The stress was applied along <001> direction, and the numbers 1-4 in Fig. 2.15(b) represent the applied magnetic field of 0, 0.4, 0.8, and 1.2 T. In Fig. 2.15(b), one can see that the PL intensity of the biexciton (M) reduces under the magnetic field, whereas the intensity of the excitons (FE) increases. This result indicates that the biexcitons become unstable under the magnetic field. From the magnetic field dependence of PL peaks, the g-factors and diamagnetic susceptibilities were determined. These authors classified the g-factor to the case of the free carrier and the excitons. Then, the values of g-factors and the diamagnetic susceptibilities

stress	g-factors				diamagnetic susceptibilites	
	free carrier		excitons		excitons	biexcitons
	g_e	g_h	g_e	g_h	d_{ex}	d_{bi}
<111>	0.8	6.8	1.0	-4	0.54	
<001>	1.57	7.2	1.6	-4	0.35	0.94

Table 2.8: g-factors and the diamagnetic susceptibilities on stressed-Ge [30].

are determined as shown in Table 2.8. Because the diamagnetic susceptibility of the biexciton d_{bi} is larger than $2d_{ex}$, the energy of the biexciton becomes larger than that of two excitons. Therefore, it was calculated that the biexcitons become unstable under the magnetic field.

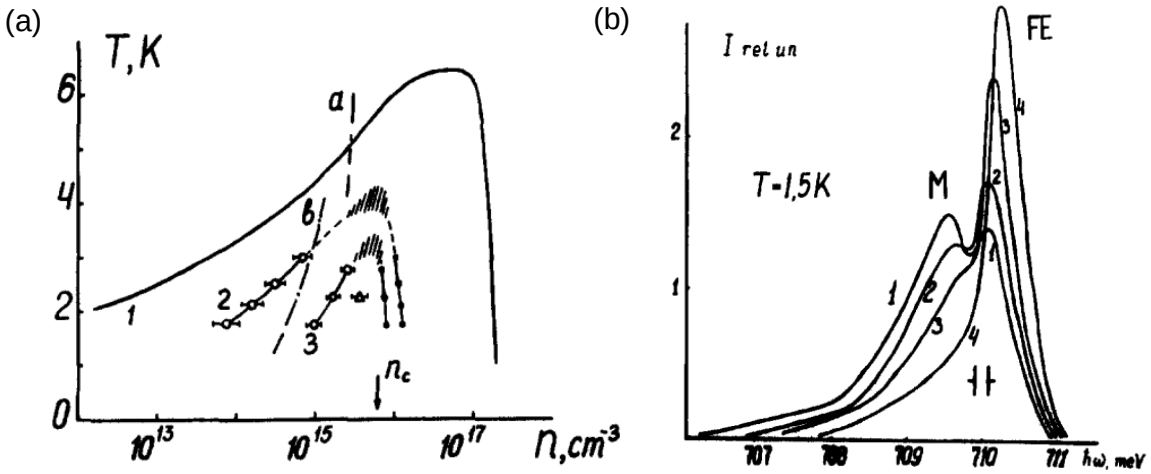

Figure 2.15: (a) The phase diagram for (1) unstressed Ge, (2) <111>-stressed Ge (400 Mpa), and (3) <001>-stressed Ge (300 Mpa). The dotted-dashed lines a and b show the critical curve of Mott transition for unstressed and stressed Ge, respectively. (b) PL spectra of stressed-Ge under different magnetic field. The uniaxial stress was applied along <001> direction [30].

2.4 Exciton BEC

Since the exciton is approximately a composite boson, it obeys the Bose-Einstein static. Hence, Bose-Einstein condensation (BEC) of the excitons is expected theoretically. By assuming the ideal Bose gas distribution, the critical temperature of the exciton BEC is given by [39]

$$T_c = (\frac{2\pi\hbar^2}{Mk_B})(\frac{n}{\xi(\frac{3}{2},1)g})^{2/3} \ , \tag{2.49}$$

with n the exciton density, g the degeneracy factor, $\xi(\frac{3}{2},1) = 2.612$ Riemann Zeta function. At the critical temperature the chemical potential equals to zero. BEC is the condensate state of particles at momentum $\hbar k = 0$ [39].

Due to the light effective mass of an exciton, the critical temperature of the exciton BEC could be much higher about three orders of magnitude than atoms system under same density [40]. Besides, from eq. 2.49, the critical temperature of the BEC depends on the degeneracy factor of the ground state. The critical temperatures of the exciton BEC in the case of (a) Si and (b) Ge are plotted in Fig. 2.16 as a function of the exciton density at different degeneracy factors by using eq. 2.49. Here, for the masses of an exciton M, in the case of the ambient pressure, we used a sum of the density of state mass of the electron and a density of state average $(m_{lh}^{3/2} + m_{hh}^{3/2})^{2/3}$ of the light hole and heavy hole (Tables 2.1 and 2.2). Under the uniaxial stress, the sum of the density of state masses of the electron and the hole are used (Table 2.5). As discussed previously, the total degeneracy factor of excitons in Si (Ge) is 48 (32). In the presence of an uniaxial stress, in the high stress limit the band degeneracy in Si and Ge reduces from [6,2] to [2,1] and from [4,2] to [1,1], respectively. Then the degeneracy factor of the excitons in Si (Ge) reduces to 8 (4). Furthermore, the spin degeneracy of 4 is lifted by applying the magnetic field in both Si and Ge. Then, the total degeneracy of the excitons in Si and Ge decreases to 2 and 1, respectively. In Fig. 2.16, each degeneracy factor represents the effect of the magnetic field and the uniaxial stress. At the temperature of 1.6 K, the critical densities of the exciton BEC are expected as 1.1×10^{16} cm^{-3} and 2.2×10^{15} cm^{-3} for degeneracy-lifted excitons in g=2 Si and g=1 Ge, respectively.

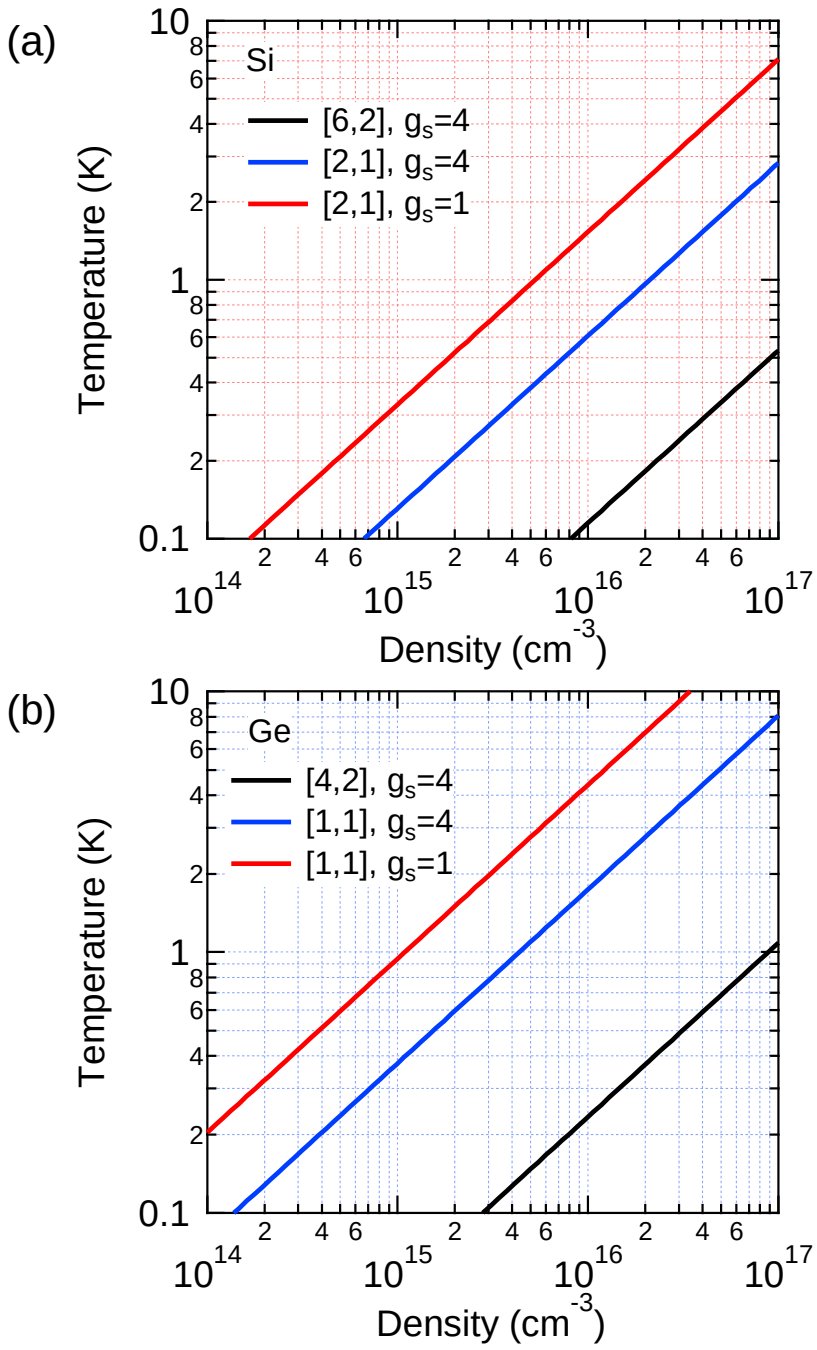

Figure 2.16: Critical temperature of the exciton BEC in (a) Si and (b) Ge. The different colors represent the degeneracy factor under the ambient pressure (black), under the uniaxial stress (blue), and under the uniaxial stress and the magnetic field.

In the strong magnetic field limit where the magnetoexcitons are formed, the

mass of the magnetoexcitons becomes the function of the magnetic field. Namely, the mass increases with the magnetic field. The mass of the magnetoexciton increases with the increase of the magnetic field, as given by $M_{00} = 2\hbar^2/E_0 l_B^2$ in 2-dimensional case [35]. In the case of Ge, the magnetoexcitons appears at the magnetic field above 3 T. Although the mass of the magnetoexcitons in 3-dimensional case cannot be expressed in an analytic form, we approximate it with that of 2-dimensional one, according to Elliott and Loudon [31]. For the magnetic field of 4 T and 7 T, the mass of the magnetoexciton is calculated as M = 0.63 and 0.90 m_0 with the in-plane mass $M_{00} = 0.39$ and 0.67 m_0, respectively. Here, the mass M was calculated by the geometric mean of the transverse and the longitudinal masses of the magnetoexciton ($\mathrm{M} = M_{00}^{2/3}(m_{el} + m_{hl})^{1/3}$) with $m_{el} = 1.58\ m_0$ and $m_{hl} = 0.04\ m_0$ [21]. The critical temperature under 4 T and 7 T is shown in Fig. 2.17

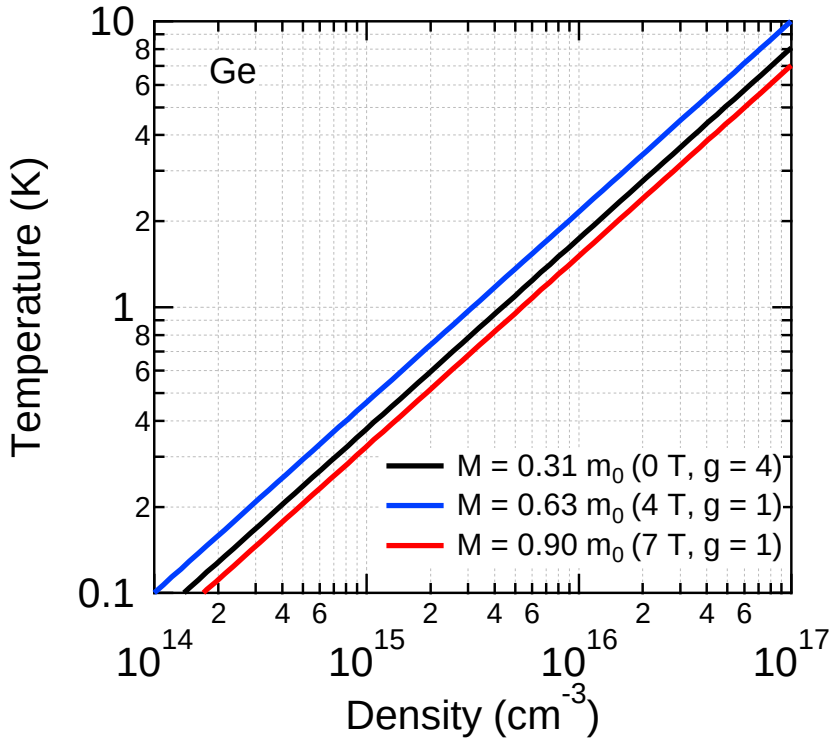

Figure 2.17: Critical temperature of the magnetoexciton BEC in Ge under zero magnetic field (black), 4 T (blue), and 7 T (red). g is the spin degeneracy.

Chapter 3

Experimental methods

In this chapter, we will describe the details of the experimental technique. Firstly, we describe the fundamentals of the THz generation and detection scheme used in the THz time-domain spectroscopy. We also describe the optical pump and THz probe measurements scheme. Details of the low temperature cryogenic system used in the experiment, the development of a pressure-anvil cell, the polarization measurement method are also described.

3.1 Broadband terahertz spectroscopy

3.1.1 Emission of THz wave

For the emission of the THz wave, we used the optical rectification method which is 2nd-order nonlinear optical effect with the crystal of (110)-oriented GaP. By irradiating the optical pulse to the nonlinear optical crystal, the 2nd-order nonlinear polarization is induced as,

$$P_i^{(2)}(t) = \sum_{jk} \chi_{ijk}^{(2)} E_j(t) E_k^*(t) \tag{3.1}$$

From this time-dependent nonlinear polarization, THz wave is irradiated. The phenomenon can be viewed as the different frequency generation (DFG) within the optical pulse, and therefore the bandwidth of the generated THz pulse is determined by the spectral width of optical pulse. Electric field of the irradiated THz wave is proportional to the 2nd derivative of eq. 3.1. Hence,

$$E_i^{\mathrm{rad}}(t) \propto \frac{\partial^2}{\partial t^2} P_i^{(2)}(t) \ . \tag{3.2}$$

In the frequency domain, from Fourier transformation of eq. 3.1, we obtain

$$P_i^{(2)}(\Omega) = \sum_{jk} \chi_{ijk}^{(2)} \int E_j(\omega + \Omega) E_k^*(\omega) d\omega \ . \tag{3.3}$$

Here, we assumed that susceptibility tensor of the nonlinear optical crystal does not depend on the frequency. From eq. 3.3, one knows that "Ω" is the frequency of the generated THz electric field. In reality, the bandwidth of generated THz wave is limited by the phase matching condition.

3.1.2 Detection of THz wave

There are two common methods to detect THz wave; the photoconductive sampling method and electro-optical (EO) sampling method. In this study, we used the EO sampling method for the detection of THz wave. When the THz pulse is irradiated to a nonlinear optical crystal, the refractive index is changed proportionately by the amplitude of electric field of the THz pulse (Pockels effect). Here, we consider the case of (110) GaP which is used in our experiments. First, we assume that the THz electric field $\mathbf{E}' = (0, -E\sin\phi, E\cos\phi)$ in the coordinate of the THz electric field (x',y',z'). Because the surface of GaP is (110), the crystal coordinate (x,y,z) and THz E-field coordinate (x',y',z') is related by rotation of 45 degrees along z-axis. When one introduces the new crystal coordinate (X,Y,Z) which is distorted by THz electric field (THz E-field) inducing, the refractive index in (X,Y,Z) coordinate can be written as

$$
\begin{aligned}
n_X^2 &\sim n(1 - \frac{1}{2}n^2 r E\cos\phi) \\
n_Y^2 &\sim n(1 - \frac{1}{2}n^2 r E\frac{-\cos\phi + \sqrt{1+3\sin^2\phi}}{2}) \\
n_Z^2 &\sim n(1 - \frac{1}{2}n^2 r E\frac{\cos\phi + \sqrt{1+3\sin^2\phi}}{2}) \ ,
\end{aligned}
\tag{3.4}
$$

where the THz E-field is sufficiently weak regime. Here, n is the refractive index of the GaP crystal without the induction of THz E-field and r is the electrooptical coefficient of the GaP crystal. The angle α between (Y,Z) axis and (y',z') axis is in relation as

$$
\begin{aligned}
\cos 2\alpha &= \frac{\cos\phi}{\sqrt{1+3\sin^2\phi}} \\
\sin 2\alpha &= \frac{-2\sin\phi}{\sqrt{1+3\sin^2\phi}} \ .
\end{aligned}
\tag{3.5}
$$

The coordinates (x',y',z') and (X,Y,Z) are shown in Fig. 3.1(a).

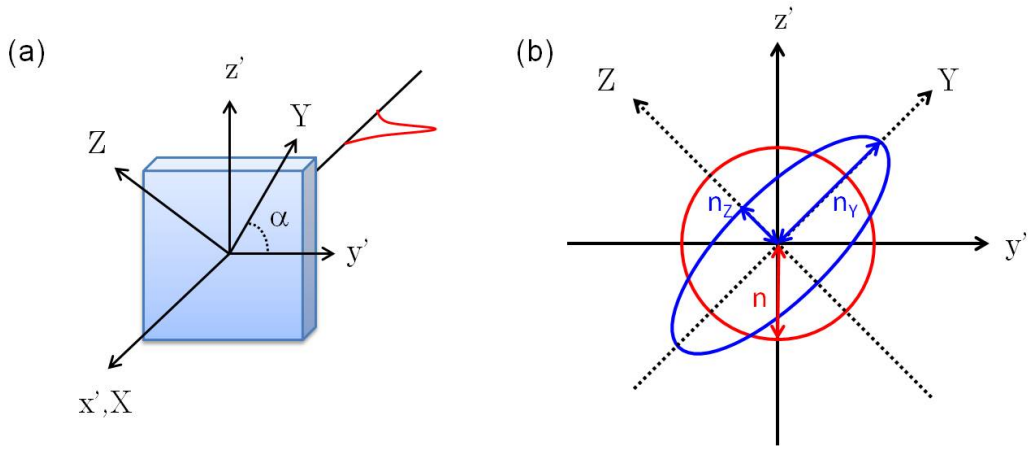

Figure 3.1: (a) The coordinates of the THz electric field (x',y',z') and the distorted EO crystal (X,Y,Z). (b) The distortion of polarization by the THz electric field. The circular polarization (red) is distorted to ellipsoid (blue) by Pockels effect.

Since the direction of THz E-field is defined along x' (=X) axis, the amplitude of the THz electric field is in YZ plane. From the different of refractive index between Y axis and Z axis (n_Y - n_Z), there arises the phase difference between the Y and Z component of gate pulse as

$$\Gamma = \frac{1}{2c}\omega n^2 r d E^{\mathrm{THz}} \sqrt{1 + 3\sin\phi} \ . \tag{3.6}$$

By this phase difference, the circular polarization of gate pulse without THz E-field will be elliptical by induction of THz E-field (Fig. 3.1(b)). The ellipticity can be obtained by difference of Y and Z component, separated by Wollaston prism. The separated Y and Z component are received by two photodiodes. When the intensities of Y and Z component is same (circular polarization), the current difference of photodiodes is zero. However, when distortion of the polarization occurs by induction of THz E-field, the current difference becomes non-zero. By detecting the current difference, we can obtain the signal of THz E-field, which is referred to as balance detection. In the case of circular polarization, the amplitude of THz E-field is given by

$$E = \frac{\lambda}{2\pi d n^3 r} \frac{\Delta I}{I} \ , \tag{3.7}$$

where ΔI is the difference of currents of two photodiodes, I is the current of a photodiode, which flows by irradiating the gate pulse.

3.2 Experimental Setup

3.2.1 Optical pump - THz probe spectroscopy system

In this study, we used an optical pump and THz probe (OPTP) spectroscopy, by combining the THz time-domain spectroscopy (THz-TDS) with the optical pulse excitation. Figure 3.2 shows an experimental setup used in this study. The laser pulse from Ti:Sapphire modelocked laser (Micra, Coherent Inc.) with the repetition frequency of 80 MHz, the bandwidth of 80 nm, and the center wavelength of 800 nm was amplified by the regenerative amplifier (Legend Elite USX, Coherent Inc.) to the pulse energy of 2.7 mJ, the repetition frequency of 1 kHz, the bandwidth of 70 nm, the pulse width of 25 fs, and the center wavelength of 800 nm. The amplified laser pulse was divided into three paths for the generation of the THz wave, the detection of the THz wave, and the optical pump. For the experiments in Ge, we used the output of the optical parametric amplifier as the optical pump with the photon energy of 0.83 eV or 0.86 eV. The THz pulse was generated by the optical rectification of the laser pulse in a 350 μm-thick (110) GaP crystal and was detected by free-space EO sampling method with a (110) GaP crystal for broadband THz spectrum [41].

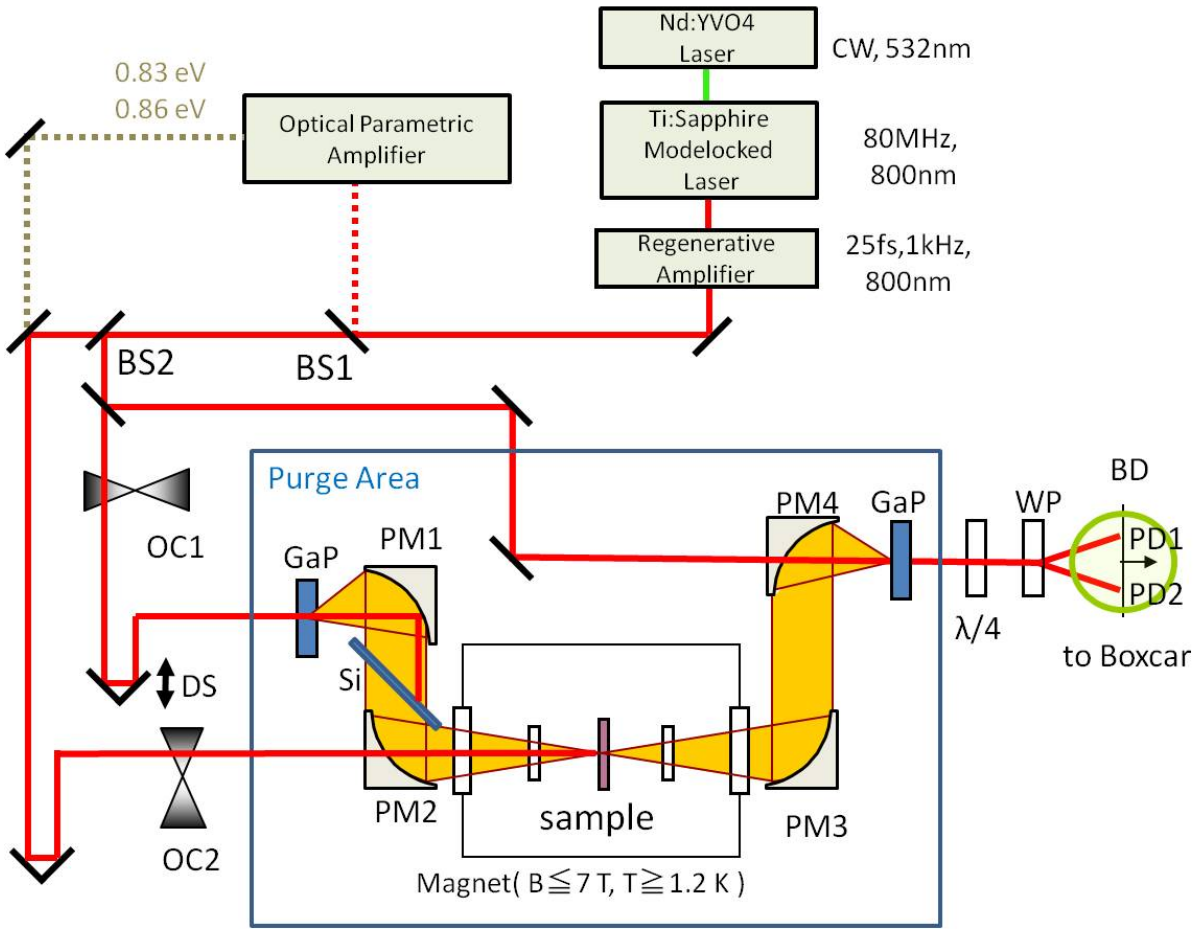

Figure 3.2: Optical pump - THz probe (OPTP) spectroscopy setup. In the experiments in Ge, we used the output of the optical parametric amplifier as a optical pump. BS : Beam Splitter, OC : Optical Chopper, DS : Delay Stage, PM : Parabolic Mirror, WP : Wollaston Prism, BD : Balance Detector, PD : Photodiode

To observe the fine structure of the intra-exciton transition, we improved the spectral resolution. In the THz-TDS, the spectral resolution is determined by the inverse of the temporal scanning range in the measurement of the THz waveform. Therefore, the long scanning range is the key issue for the high spectral resolution. For example, to realize the resolution as high as 0.2 meV (= 0.05 THz), the scanning temporal range must be longer and 1/(0.05 THz) = 20 ps. However, in the case of such a long-range scan, other delayed THz pulses are also observed after the main THz pulse. These delayed THz pulses originate in the reflection from the back surface of EO crystal, the windows of the cryostat, and the sample itself, and then the interference of these multiple THz pulses makes the spectral analysis significantly complicated. To avoid the multiple reflection inside the EO crystal and to obtain the high spectral resolution, a thick EO crystal is required.

On the other hand, due to the phase match condition between the THz pulse and optical pulse, thick EO crystals for THz generation and detection would prevent us from generating the THz pulse efficiently and detecting the electric waveform

accurately. Therefore, we measured the THz wave signal by using different GaP crystals with various thicknesses both for the THz wave generation and detection. Figure 3.3 shows the detected waveforms of the THz electric field and their power spectra with various thicknesses d of the GaP crystals.

Figure 3.3(a) and (b) show the experimental results by using $d = 350$ μm GaP crystal for the THz detection. When we use the $d = 350$ μm GaP crystal also for the THz generation, the broad power spectrum up to 7 THz is obtained as shown in the red curve in Fig. 3.3(b) with slight dip at around 4 THz. In case that d=1 and 2 mm GaP crystals are used for the THz generation, smooth and broad power spectra are obtained as shown in Fig. 3.3(b).

However, when we use $d = 1$ and 2 mm GaP crystals for the THz detection, as shown in Fig. 3.3(c)-(f), the temporal waveform of the THz electric field becomes very complicated, and the large dips appear in the power spectra.

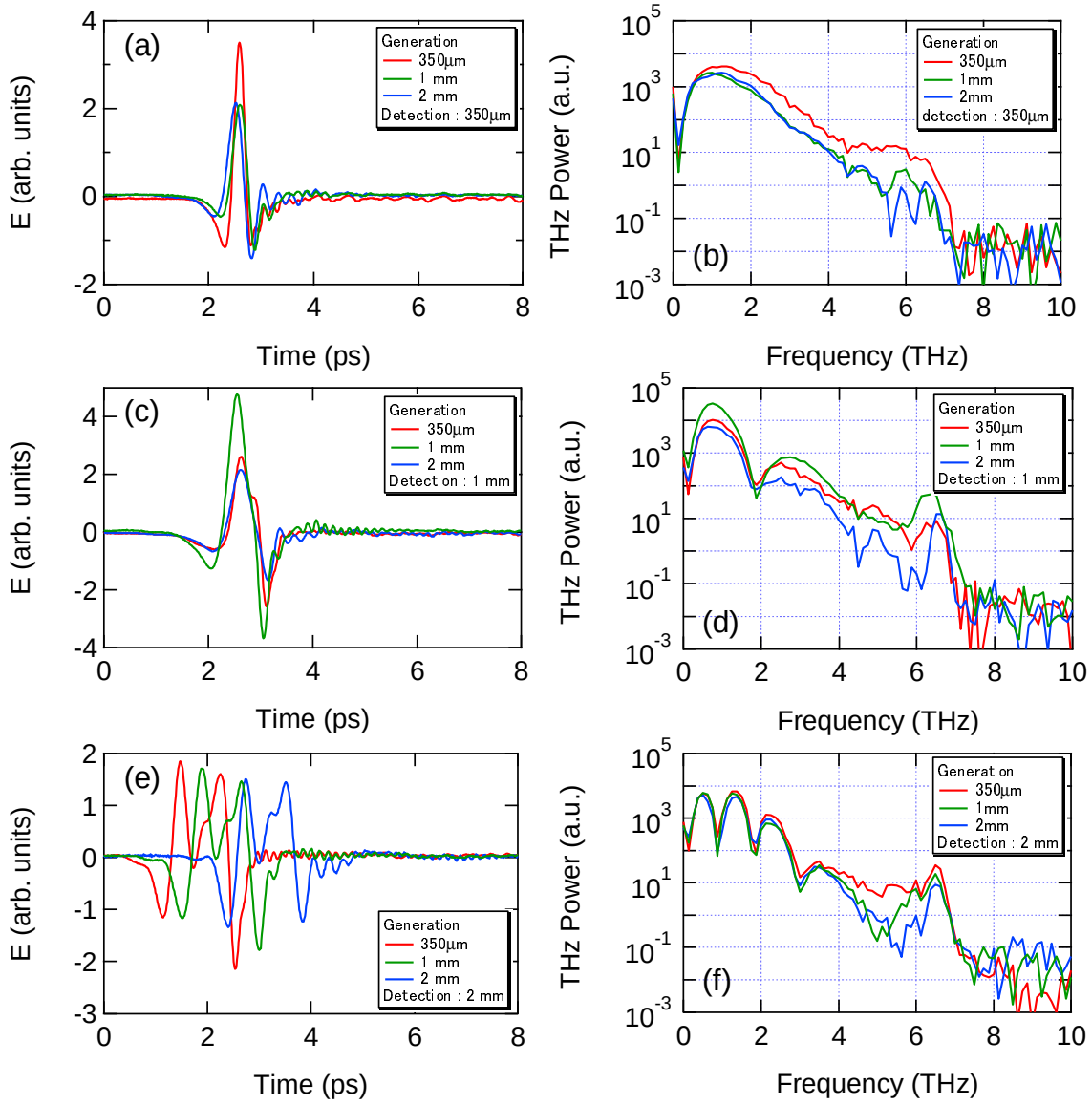

Figure 3.3: Electric field waveforms ((a),(c),(e)) and the Fourier transformed spectra ((b),(d),(f)) with different thickness of the generation and the detection GaP crystals.

These results can be understood by the group velocity mismatch (GVM). When the THz pulse and the gate optical pulse copropagate within the EO crystal, the accumulated GVD time is expressed as [41, 42]

$$\delta(\Omega) = \frac{n_g(\lambda_0) - n(\Omega)}{c} d \tag{3.8}$$

where $n_g(\lambda_0)$ is the refractive index for the group velocity of the optical pulse with the wavelength of λ_0,

$$n(\Omega) = \sqrt{\epsilon_\infty \left[1 + \frac{(\hbar\Omega_{\rm LO})^2 - (\hbar\Omega_{\rm TO})^2}{(\hbar\Omega_{\rm TO})^2 - (\hbar\Omega)^2 - i\hbar\gamma\Omega}\right]} \tag{3.9}$$

is the refractive index for the phase velocity of the THz pulse with the frequency of Ω. As a result, GVD induces the modulation of the frequency response function represented as

$$G(\Omega) = \frac{t(\Omega)}{\delta(\Omega)} \int_0^{\delta(\Omega)} e^{i2\pi\Omega t} dt = t(\Omega) \frac{e^{i2\pi\Omega\delta(\Omega)} - 1}{i2\pi\Omega\delta(\Omega)} \ , \tag{3.10}$$

where $t(\Omega) = 2/[n(\Omega) + 1]$ is the Fresnel transmission coefficient.

We calculated the frequency responses of the GaP crystal $|G(\Omega)|$ with different thickness by using eq. 3.10. Figure 3.4 shows the calculated result. The crystal-thickness dependence of $|G(\Omega)|$ is consistent with our experimental result. For the calculation, we used the values $epsilon_\infty = 9.075$, $\hbar\Omega_{\rm LO} = 50.0$ meV, $\hbar\Omega_{\rm TO} = 45.5$ meV [42], $\lambda_0 = 800$ nm, $n_g(800\text{nm}) = 3.56$ [43].

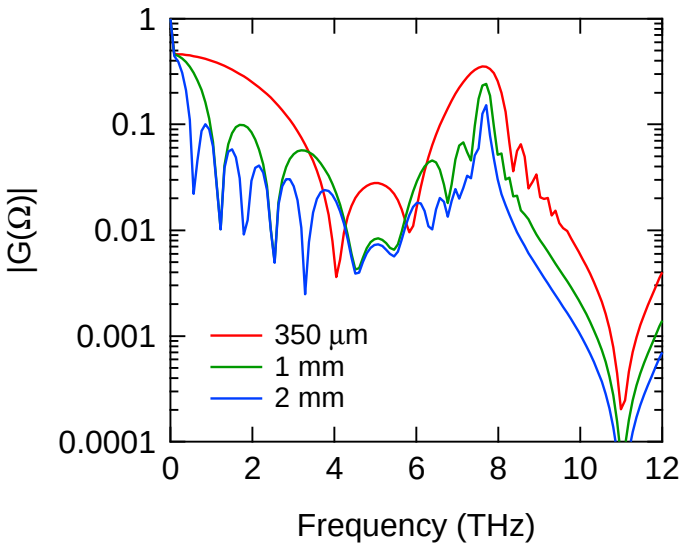

Figure 3.4: Group velocity mismatch in GaP with different thickness calculated by eq. 3.10 [41].

Consequently, we cannot use the (110) GaP crystal thicker than 1 mm for the THz detection because of the phase mismatching. To overcome this problem, we bonded the (110) GaP crystal with d =350 μm with another thick (100) GaP crystal with $d = 3$ mm by the van der Waals force. Since the (100) GaP crystal has same refraction index with (110) GaP, the reflection from the boundary between these two crystals is negligible. The interaction between the THz pulse and the (100) GaP does not contribute to the detected EO sampling signal because of the orientation

of the crystal. The delay time between the main THz pulse and the reflected THz pulse from the (110)-(100) bonded GaP crystal is calculated as $n_{\mathrm{GaP}} \times d \times 2/c$, where $n_{\mathrm{GaP}} \sim 3$ is the refractive index of GaP at THz frequency, d is the thickness of the GaP crystal and c is the speed of light. This way, we can avoid the reflection from the back surface of the EO crystal with keeping the delay time long. In this study, the spectral resolution was 0.2 meV, which was limited by the thickness of the cryostat window instead of the GaP crystal. Figure 3.5 shows the finally-obtained THz waveform and spectrum by using the (110)-(100) bonded GaP crystal.

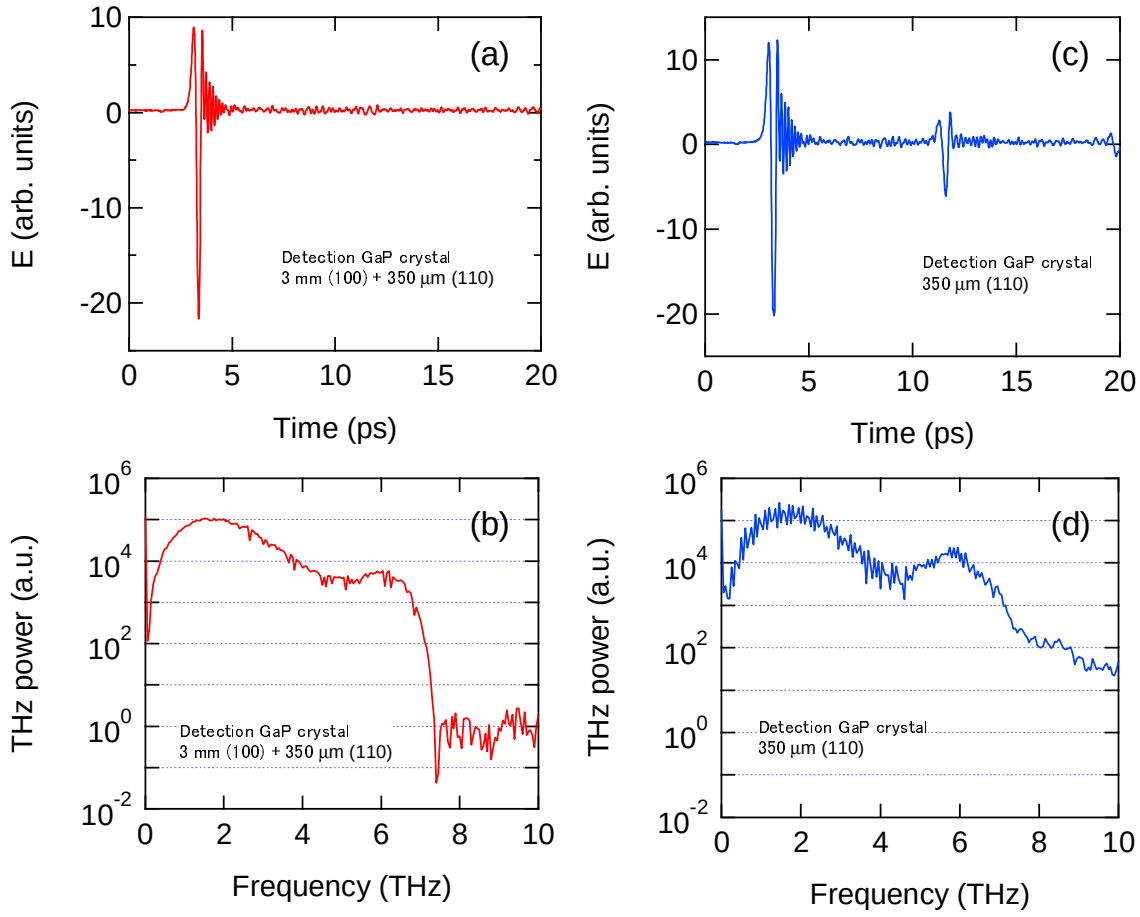

Figure 3.5: (a) THz waveform and (b) the power spectrum by using the 3 mm (100) GaP-bonded 350 μm (110) GaP crystal as a THz detection. (c), (d) That of by using the 350 μm (110) GaP crystal.

3.2.2 Superconducting magnet

For the measurement under the magnetic field at low temperature, we used a cryostat embedded in a superconducting magnet (Spectromag 4000, Oxford Instruments.).

This magnet can apply the magnetic field parallel or perpendicular to the incident THz wave by a split-type coil. In this study, we apply the magnetic field parallel to the THz beam and perpendicular to the sample surface (Faraday configuration). The maximum magnetic field is 7 T. Also, the temperature of variable temperature insert (VTI) can be controlled from 1.5 K to 300 K. By decreasing the pressure of liquid helium with vacuum pumping, the temperature cools down to 1.2 K. Because a sample chamber is separated from outside of the cryostat by the vacuum chamber, the optically-transparent windows are necessary for optical measurements. For the THz beam transmission, the diamond windows with a thickness of 1 mm are used between the sample chamber and the vacuum chamber. Moreover, SiO_2 windows have been initially set up between the vacuum chamber and outside of the cryostat.

Measurable regime of the superconducting magnet was limited by SiO_2 window. SiO_2 is transmissive only from 0.5 to 2 THz. To measure higher frequency regime, we replaced the window from SiO_2 to Tsurupica. Figure 3.6 shows the transmitted THz waveform and spectrum with SiO_2 windows and Tsurupica windows, respectively. The cut off at 7 THz in Fig. 3.6(d) is due to the generation and the detection with GaP, and not due to the Tsurupica window.

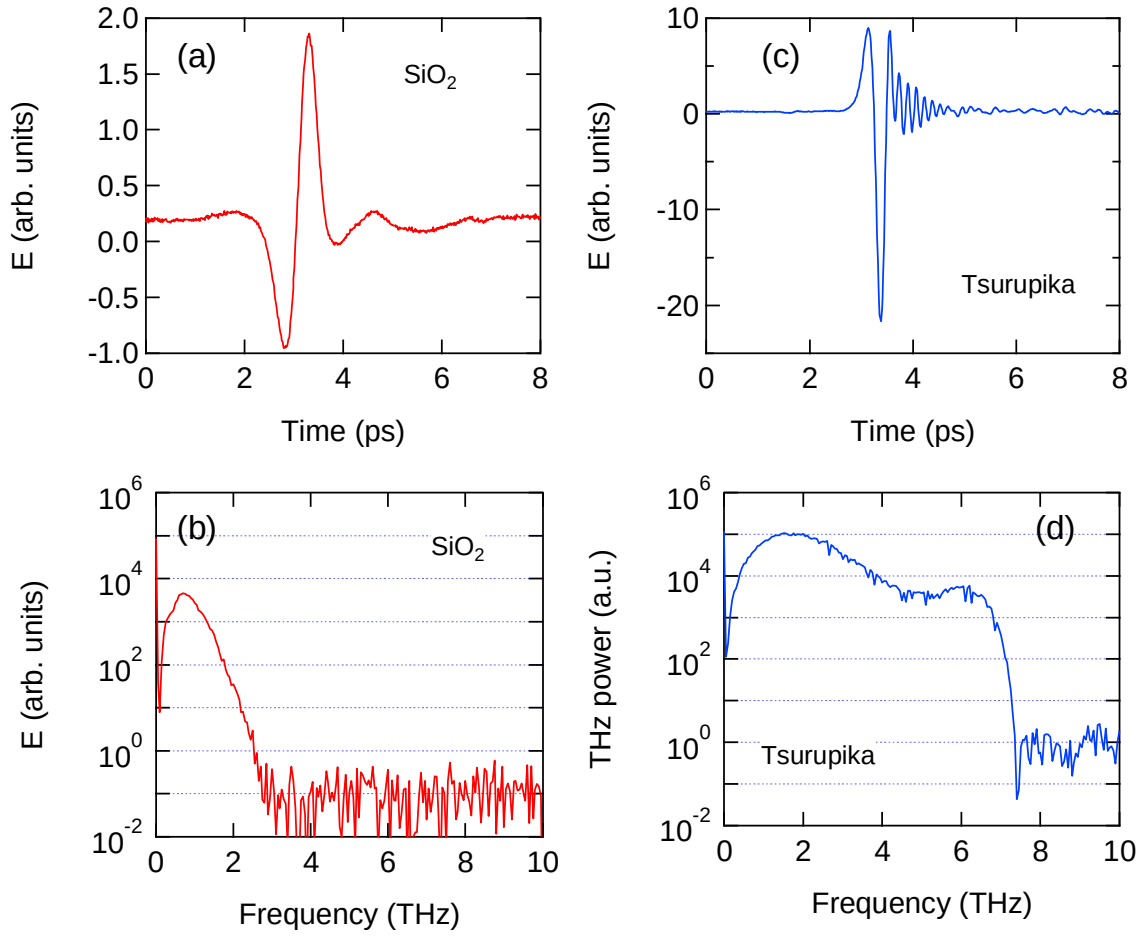

Figure 3.6: The temporal waveform and the power spectrum of the THz pulse by using SiO_2 ((a),(b)) and Tsurupica ((c),(d)) as the windows of the cryostat.

3.2.3 Vacuum pump for single shot method

To cool the samples (Si or Ge) below the liquid helium temperature, we performed the single shot method. At first, we used a rotary pump E2M28 (Edwards). The design exhaust velocity at 50 Hz and the effective exhaust velocity (50 Hz) of E2M28 are 537 and 458 L/min, respectively. By pumping the liquid helium with E2M28, the temperature of 1.5 K was achieved. To realize lower temperature, we used a large size rotary pump E2M80 (Edwards) and the mechanical booster pump EH500 (Edwards). Combined with a back-pressure pump such as the rotary pump or dry pump, the mechanical booster pump enhances the exhaust velocity dramatically. By introducing hydrokinetic drive, EH500 can be switched on simultaneously with back-pressure pump. By using this vacuum pump system, the temperature of 1.2 K is achieved. The specifications of E2M80 and EH500 are shown in Table 3.1. The vacuum pump system is connected to the sample chamber by the pipeline with

the length of 2 m. The standard connection flange of EH500 is ISO 100. To realize lower temperature, the diameter of pumping line is important to improve evacuation efficiency. By using the pumping line combination of 1 m pipelines with the standard of ISO 100 and with the standard of NW25, the temperature reached to only 1.32 - 1.35 K. Also, by replacing the pumping line of NW25 to NW40, the achieving temperature was 1.27 K. The temperature of 1.20 K was achieved by using the 0.63 m pumping line of ISO 100. In the last 0.3 m, the diameter conversion of pumping line was ineluctable to avoid the interference with the cryostat. The setup of single shot measurement is shown in Fig. 3.7

Rotary (E2M80)	
Operating temperature range.	12 - 40 °C
Surface temperature of pump body (Operating)	50 - 70 °C
Design exhaust velocity (50 Hz)	1,333 L/min
Effective exhaust velocity (50 Hz)	1,233 L/min
Accessible pressure	1×10^{-4} Pa
Mechanical Booster (EH500)	
Operating temperature range.	-20 - 40 °C
Design exhaust velocity (50 Hz)	505 m^3/h
Pump rotation	0 - 2900 r $\min^{-1}$
Max exhaust port pressure	1000 mbar (1×10^5 Pa)
Pressure difference	0 - 110 mbar (0 - 1×10^4 Pa)

Table 3.1: Performance of rotary pump E2M80 and mechanical booster pump EH500

Figure 3.7: Picture of a pumping line for the single shot measurement.

3.3 Spectral analysis

In the THz-TDS, we can obtain both the amplitude and phase of the THz pulse in the frequency domain by the Fourier transformation of the temporal waveform measured in the time domain. Then we calculated the response function of our samples as follows.

By considering the multiple reflections inside the sample, the THz electric field transmitted through the sample is written by

$$\begin{aligned} E_{\text{sample}}(\omega) &= E_{\text{in}}(\omega)\frac{2\hat{n}(\omega)}{\hat{n}(\omega)+1}\text{Exp}\left(i\frac{\hat{n}(\omega)\omega d}{c}\right)\frac{2}{\hat{n}(\omega)+1}\sum_{j=0}^{\infty}\left[\left(\frac{2\hat{n}(\omega)}{\hat{n}(\omega)+1}\right)^2\text{Exp}\left(i\frac{2\hat{n}(\omega)\omega d}{c}\right)\right]^j \\ &= E_{\text{in}}(\omega)\frac{2\hat{n}(\omega)}{\hat{n}(\omega)+1}\text{Exp}\left(i\frac{\hat{n}(\omega)\omega d}{c}\right)\frac{2}{\hat{n}(\omega)+1}\frac{1}{1-\left(\frac{2\hat{n}(\omega)}{\hat{n}(\omega)+1}\right)^2\text{Exp}\left(i\frac{2\hat{n}(\omega)\omega d}{c}\right)}\ , \end{aligned} \quad (3.11)$$

where E_{in} is the incident electric field, $\hat{n}(\omega)$ is the complex refractive index, d is the sample thickness.

In this study, we investigated the change of the complex dielectric function induced by the photoexcitation. The ratio of the electric field transmitted the sample with optical pump to that without optical pump is represented as

$$\frac{E_{\mathrm{pump}}^{\mathrm{Exp}}}{E_{\mathrm{ref}}^{\mathrm{Exp}}} = \frac{\frac{2\hat{n}'(\omega)}{\hat{n}'(\omega)+1}\mathrm{Exp}\left(i\frac{\hat{n}'(\omega)\omega d}{c}\right)\frac{2}{\hat{n}'(\omega)+1}\frac{1}{1-\left(\frac{2\hat{n}'(\omega)}{\hat{n}'(\omega)+1}\right)^2\mathrm{Exp}\left(i\frac{2\hat{n}'(\omega)\omega d}{c}\right)}}{\frac{2\hat{n}(\omega)}{\hat{n}(\omega)+1}\mathrm{Exp}\left(i\frac{\hat{n}(\omega)\omega d}{c}\right)\frac{2}{\hat{n}(\omega)+1}\frac{1}{1-\left(\frac{2\hat{n}(\omega)}{\hat{n}(\omega)+1}\right)^2\mathrm{Exp}\left(i\frac{2\hat{n}(\omega)\omega d}{c}\right)}}, \tag{3.12}$$

where $\hat{n}'(\omega)$ is the complex refractive index changed by the optical pump. We numerically solved this equation to obtain $\hat{n}'(\omega)$. Then we calculated the photo-induced dielectric function $\Delta\epsilon(\omega)$ and the optical conductivity spectra $\Delta\sigma(\omega)$, which indicate the optical response of the photoexcited e-h system in semiconductors.

3.4 THz spectroscopy system under the uniaxial stress

As mentioned in Chapter 2, the presence of an uniaxial stress is indispensable to suppress the formation of EHD. To investigate the response of e-h system in such a condition, we developed the OPTP system under the uniaxial stress.

3.4.1 Pressure anvil cell for OPTP measurement under the uniaxial stress

For the THz spectroscopy under the uniaxial stress, two conditions must be implemented. At first, for the homogeneous distribution of photoexcited e-h system, we used thin films Si and Ge as samples. Here the term "thin" means that the thickness of the sample is comparable to the penetration depth of optical pump. Then, uniaxial stress must be applied along the direction of the light propagation. Therefore, the anvil cell must be transparent in both optical pump and THz probe frequency region. Secondly, a large-area anvil cell is required because the spot size of THz beam is large due to the long wavelength of THz wave. From these conditions, we developed an pressure anvil cell by collaboration in laboratory. Figure 3.8(a) shows the structure of anvil cell. The anvil cell (aqua trapezoids in Fig 3.8(a)) presses the sample from both forward and backward direction in a circle. To apply the homogeneous stress, we screw the anvil cell holder at two opposite sides by clockwise and anti-clockwise. Furthermore, to keep the parallelism of the anvil cells, we added the metal bars which is shown in Fig 3.8(a) as blue squares. The size of the anvil cell is shown in Fig. 3.8(b), where the unit is in mm. The surface with the diameter of 2 mm is contacted with sample. The anvil cell was designed as a cut-circular cone to increase the solid angle. The anvil cell was made by SiC which is transparent at both THz probe and optical pump wavelength regimes. By monitoring the Newton ring on sample by the microscope, we carefully applied the stress homogeneously. The picture of developed cell is shown in Figure. 3.8(c).

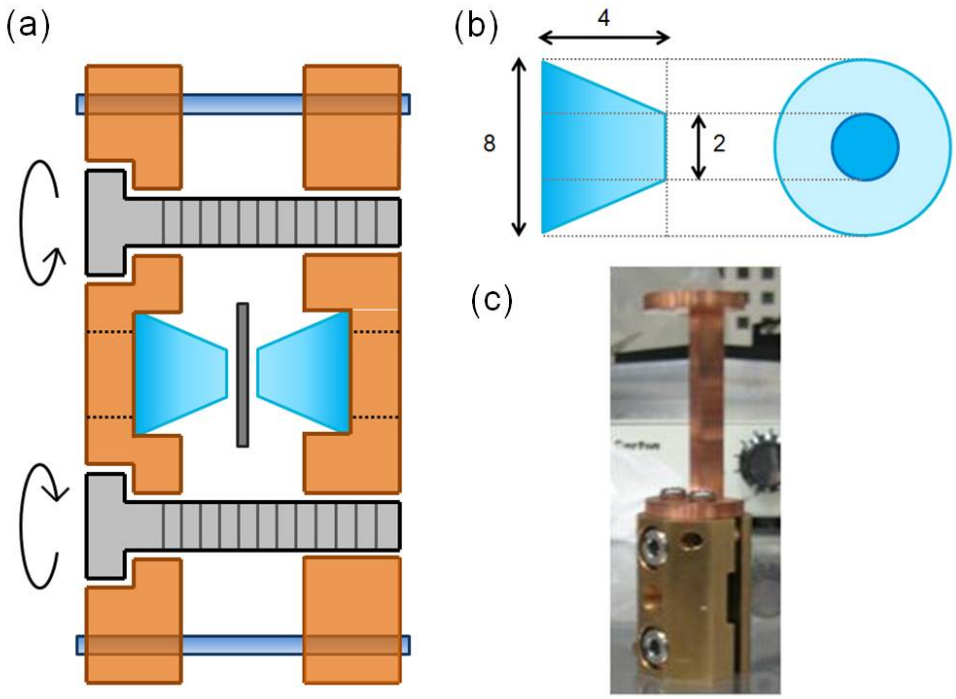

Figure 3.8: (a) The structure of the developed anvil cell. The stress is applied by screws. (b) The size of the anvil cell (in mm). the surface with the diameter of 2 mm is contacted with the samples. (c) Picture of the developed SiC anvil cell.

3.5 Polarization measurement method

We performed the polarization measurement of the THz pulse transmitted after the sample for the case of Ge under high magnetic field. For the polarization measurements of transmitted THz pulse, we used three wire grid polarizers (WGP) in the THz wave path. The WGP were made of Tungsten wire with a diameter of 10 μm and with the interval of 20 or 30 μm, and they transmits only the THz wave polarized perpendicular to the direction of the wires. First WGP was placed in front of a sample to fix the linear polarization of the incident THz wave. Second WGP was placed behind the sample. The direction of the second WPG was set either parallel or perpendicular to the first WPG to separate the parallel and perpendicular components of the THz wave which was induced by Faraday effect in the Ge sample (Fig. 3.9). Third WGP was placed behind the second WPG with the degree of 45° to avoid difference of THz detection efficiency between parallel and perpendicular polarization at EO sampling crystal.

Figure 3.10 shows (a) the electric fields and (b) the power spectra of the THz wave with x (red) and y (green) polarization. From the ratio of the power spectrum of perpendicular polarization to that of parallel polarization, the extinction ratio was evaluated (Fig. 3.10 (c)). The extinction ratio increases with increasing frequency

due to shortening of wavelength. In this study, the extinction rate was 10^{-4} to 10^{-2} in frequency regime of our measurement (0.5 to 5 THz).

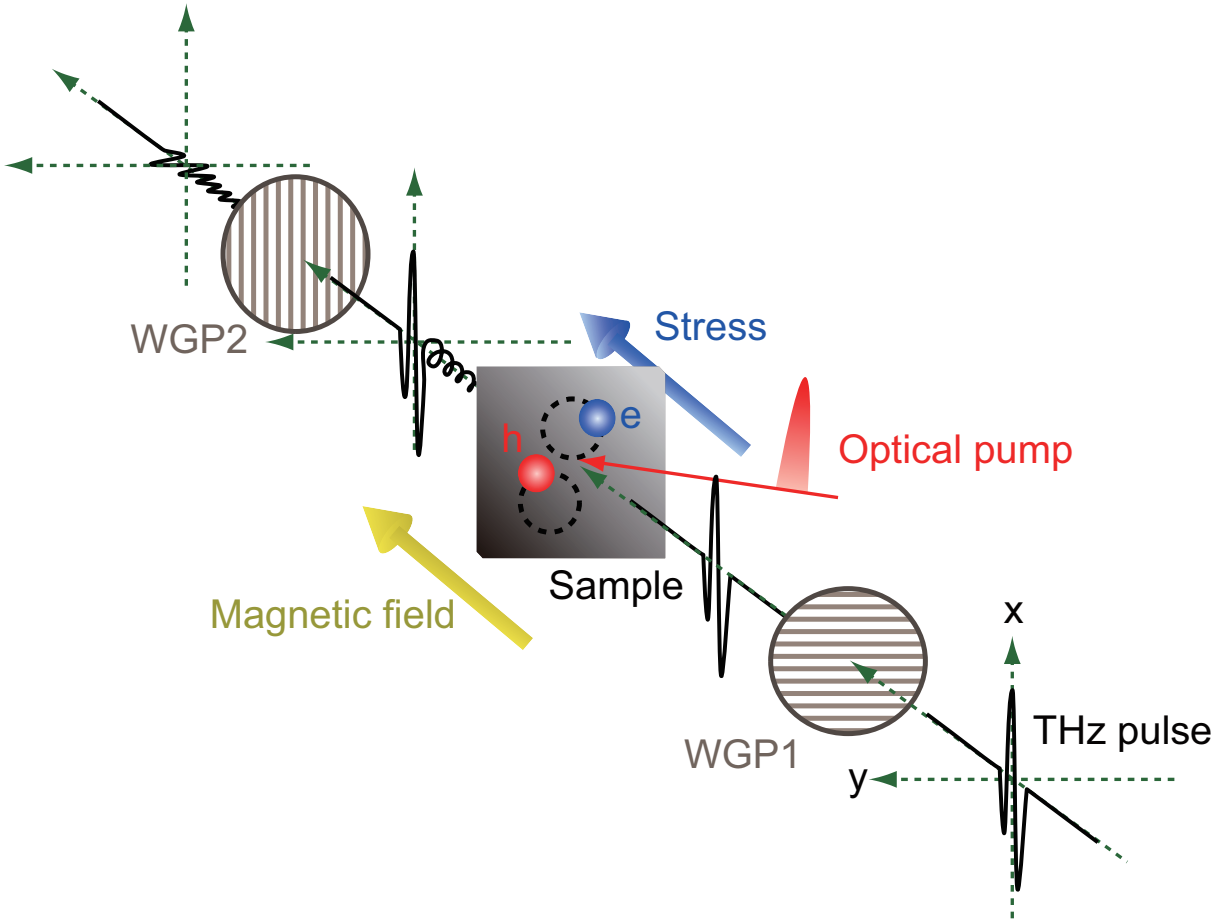

Figure 3.9: Schematic of polarization measurement on the OPTP spectroscopy. Parallel (x) and perpendicular (y) components of THz pulse can be obtained separately by rotating WGP2

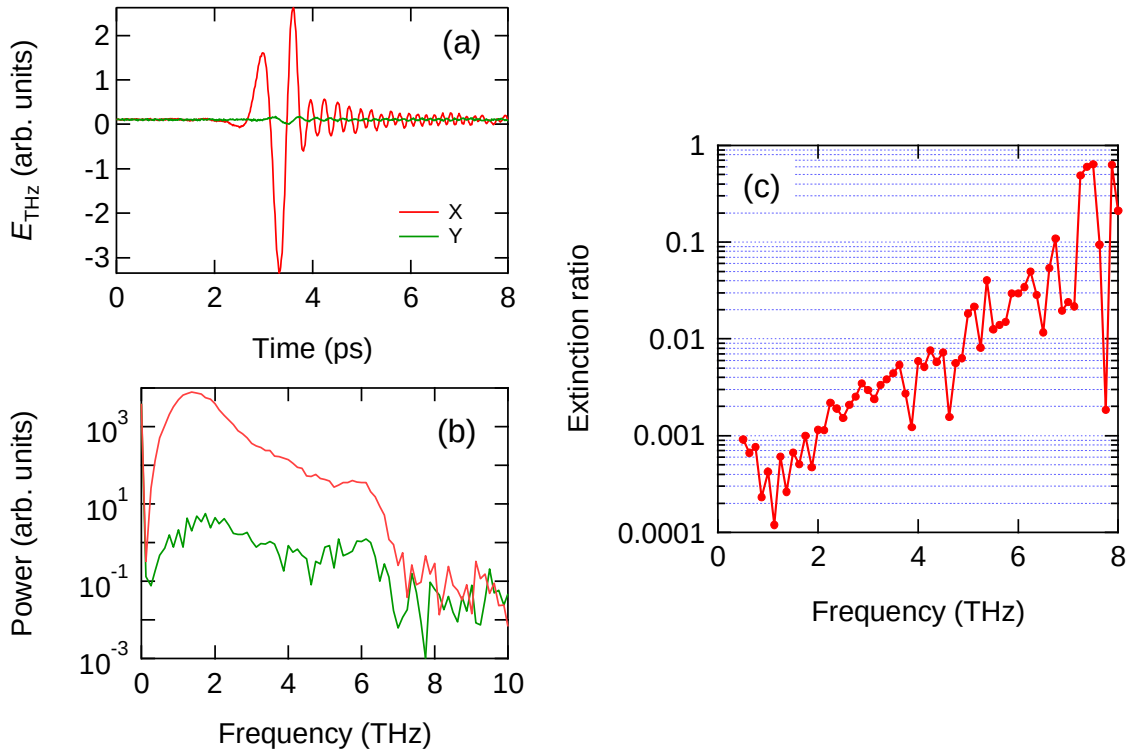

Figure 3.10: (a) Electric fields and (b) power spectra of x (red) and y (green) polarization component of THz wave. (c) Extinction ratio obtained from the ratio between the power of x and y components.

To investigate the response of photoexcited e-h pairs in Ge, we combined our OPTP system with the polarization measurement. Figures 3.11(a) and (b) ((c) and (d)) show the waveforms of THz pulse and the power spectra of E_x (E_y) component with and without optical pump under 7 T, respectively. It can be seen that the amplitude of the E_x component decreases by optical pump, whereas E_y component increases. This means that the polarization of THz wave is changed significantly by photoexcited carriers under the magnetic field. In such condition, the simple transmission measurement with a fixed polarization, e.g., $E_{xx}(\omega)$ which denotes the transmittance in the x-direction for the x-polarized incident beam, is in sufficient to discuss about the net absorption.

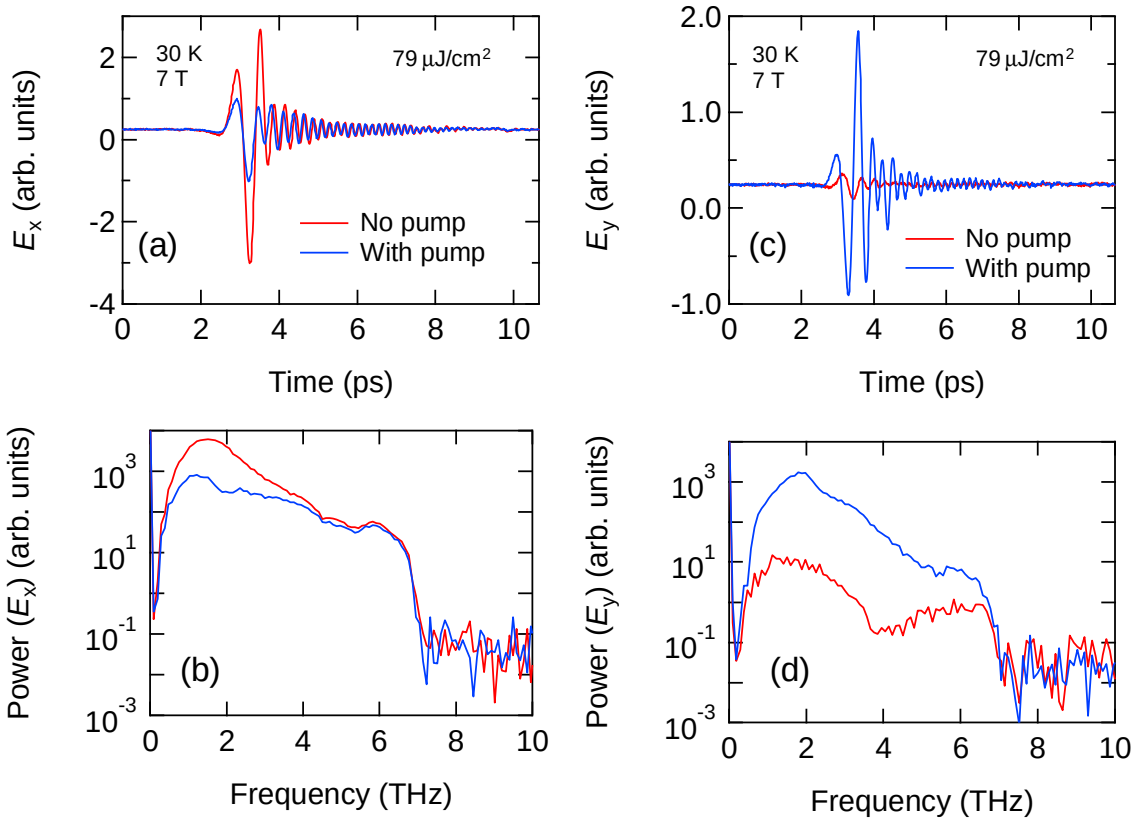

Figure 3.11: (a) Electric fields and (b) power spectra of the parallel polarization without (red) and with (blue) optical pump with and without optical pump. (c) Electric field and (d) power spectra of the perpendicular polarization with and without optical pump under 7 T. The temperature was 30 K.

To evaluate the change of polarization quantitatively, we measured both rotation angle and ellipticity which is caused by the Faraday effect. Here, we define the complex number χ

$$\chi = \frac{\tilde{E}_y(\omega)}{\tilde{E}_x(\omega)} = \frac{E_y}{E_x}\exp(\tau + \delta) \ . \tag{3.13}$$

Then the Faraday rotation angle θ and ellipticity angle η are given by

$$\tan(2\theta) = \frac{2\mathrm{Re}[\chi]}{1 - |\chi|^2} \tag{3.14}$$

$$\sin(2\eta) = -\frac{2\mathrm{Im}[\chi]}{1 + |\chi|^2} \ , \tag{3.15}$$

respectively [44, 45].

Chapter 4

The magnetic field effect and lifetime measurement of the excitons in Si under the ambient pressure

In this Chapter we investigated the magnetic field effect and the lifetime of the excitons in Si. To increase the critical temperature of the exciton BEC, we apply the magnetic field to lift the spin degeneracy. Firstly, we studied the magnetic field effect on the exciton fine structures in Si. Besides, due to the indirect band structure of Si, excitons have a long lifetime. Furthermore, the spin-triplet excitons accumulated under the magnetic field could have a crucially long lifetime due to the prohibition of the optical transition. However, the direct observation of the spin-forbidden excitons under the magnetic field by monitoring the interband transition such as PL spectroscopy is difficult. Therefore, we investigated the lifetime of excitons in Si, through the observation of intra-exciton transition in the THz frequency range. The measurements of the intra-exciton transition enable us to observe the exciton population qualitatively, even for the spin-forbidden excitons. We developed an OPTP spectroscopy scheme to study the dynamics of the long-lived excitons in a very long time scale from sub-microseconds to a millisecond regime as we explain as follows.

4.1 Evaluation of the impurity concentration

First, we evaluated the quality of the sample. We used (111)-oriented high resistivity (100 k Ω cm) undoped n-type Si single crystal grown by the float-zone method with the thickness of 925 μm as a sample. Since the conventional Hall measurements are difficult to estimate the dopant concentration for such high resistivity Si samples, we calibrated our sample by the PL intensity ratio between the free excitons and the bound excitons, which is the method reported by M. Tajima [46]. The concentration of the impurity P or B can be estimated from the intensity ratio between the free

exciton and the bound exciton as shown in Fig. 4.1 at liquid helium temperature.

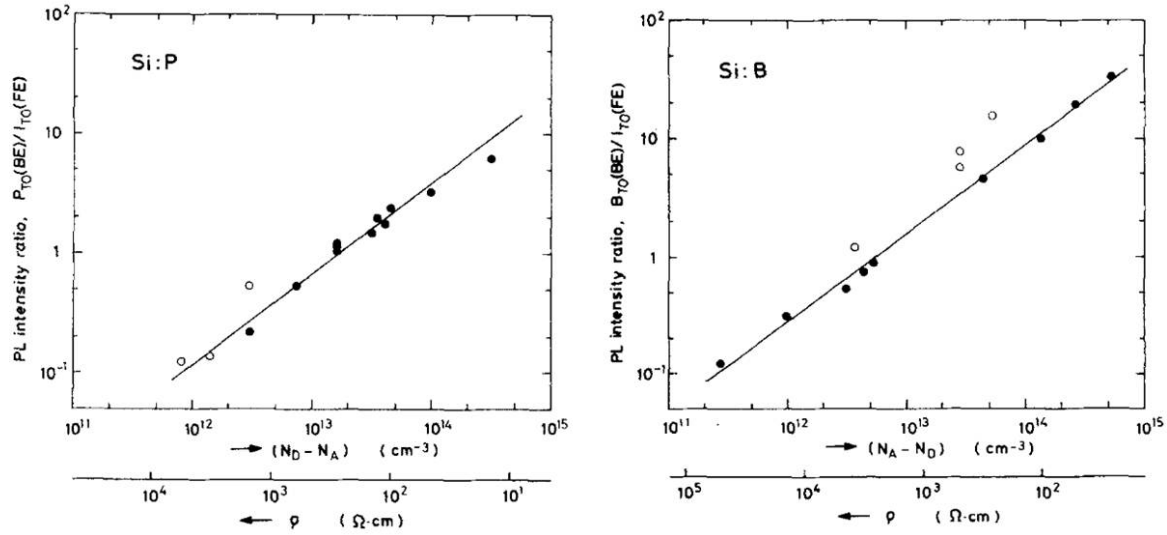

Figure 4.1: Calibration curve for the PL method for P-doped (left) and B-doped (right) Si [46].

We observed PL spectra at different temperatures. As shown in Fig. 4.2(a), the PL peak at 1.097 eV becomes sharp with decreasing temperature and splits to two peaks. These peaks are TO- and LO-phonon assisted sideband PL spectrum of free excitons [47]. Further, at low temperature, a new peak appears at low-energy side of the free exciton PL peak. This peak is associated with the TO-phonon assisted bound exciton which is bound to the impurity P. We evaluated impurity concentration from the PL spectrum at 5 K which is close to the temperature used in the calibration procedure in Ref. 46 (Fig. 4.2(b)). From the intensity ratio between FE_{TO} and BE_{TO} (P), the concentration of the impurity (P) was estimated to $\sim 10^{12}\mathrm{cm}^{-3}$.

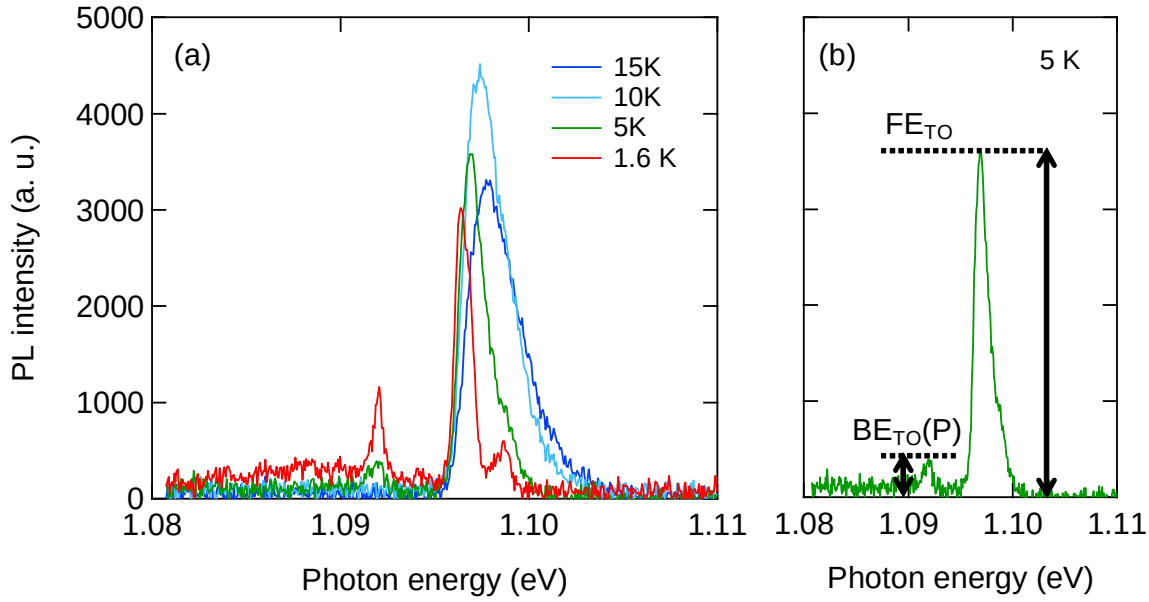

Figure 4.2: (a) PL spectra of our sample at different temperature. (b) PL spectrum at 5 K. Peaks of free exciton (FE) and bound exciton (BE) are shown.

4.2 The magnetic field effect

4.2.1 PL spectroscopy

Under the magnetic field, the spin degeneracy of the 1S exciton is lifted and the spin-forbidden exciton becomes the lowest energy state (Fig. 2.10). The lowest energy spin-triplet exciton state cannot be observed by PL spectroscopy. Hence, this exciton of the lowest energy is a dark exciton. In order to investigate the accumulation of dark exciton populations indirectly, we first performed the PL spectroscopy of bright excitons under the magnetic field up to 7 T. Figure 4.3(a) shows PL spectra at 1.6 K under the magnetic field. The two PL peaks are assigned by the TO- and LO-phonon-sidebands of the $1S$ exciton [47]. By applying the magnetic field, the PL peak of $1S$ excitons shifts to low-energy side slightly, and the PL intensity is reduced significantly. Further, the decrease of the exciton PL intensity by the magnetic field becomes prominent at lower temperature as shown in Fig. 4.3(b).

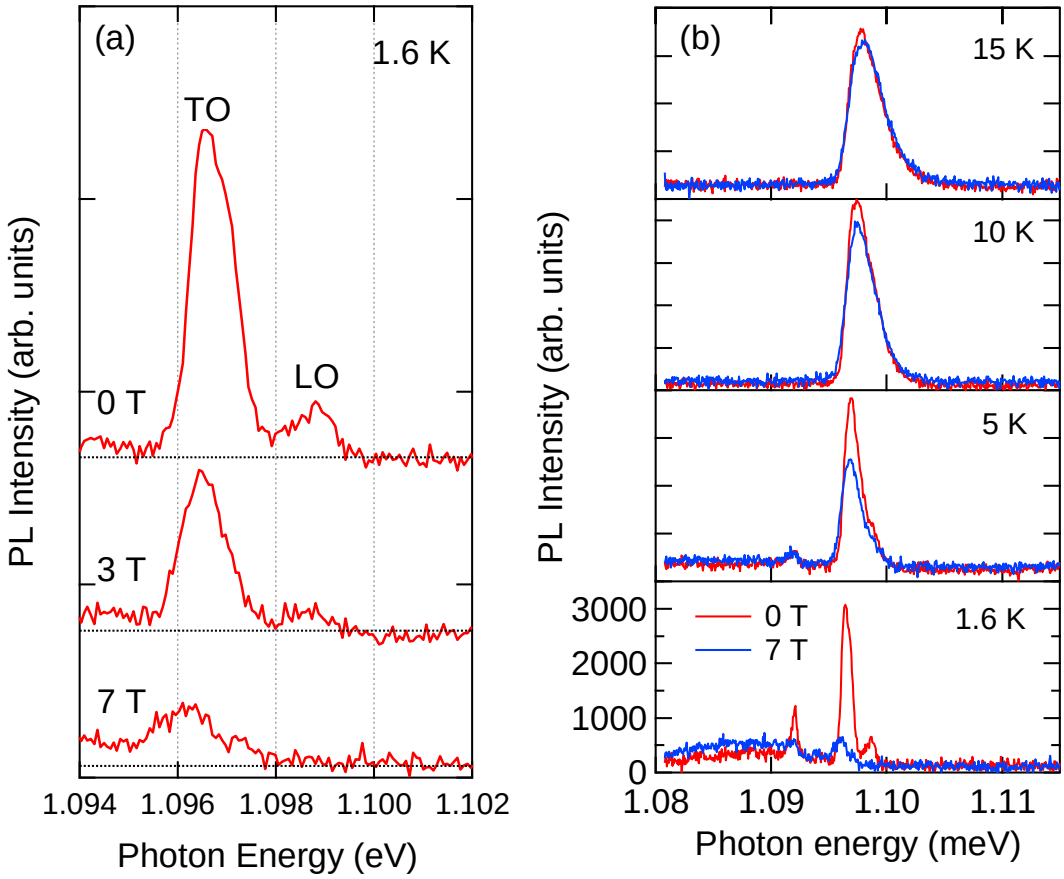

Figure 4.3: (a) PL spectra of excitons in Si under the magnetic field at the lattice temperature of 1.6 K. Labels TO and LO represent TO- and LO-phonon assisted PL spectra of the $1S$ excitons, respectively. (b) PL spectra under zero field and 7 T at different temperature from 1.6 K to 15 K.

To analyze this behavior, we used the hydrogen atom model to express the eigenenergy under the magnetic field as,

$$E(B) = E(0) + (\mu_B g_e S_z^e + \mu_B g_h J_z^h)B + \frac{e^2 < x^2 + y^2 >}{8\mu} B^2 \ , \tag{4.1}$$

where, μ_B is the Bohr magneton, g_e (g_h) is the electron (hole) g-factor, S_z^e and J_z^h are the projections of the electron and hole spins along the magnetic field direction, respectively. The detail for eq. 4.1 and the coefficients for Zeeman splitting and the diamagnetic shift are explained in Chapter 2. Figure 4.4(a) represents the experimental result (closed circles) and theoretical curves for the energy shift of $1S$ exciton under the magnetic field. The red lines denote the theoretical curves of the exciton with $J_z = \pm 3/2$ (Δ_7) and blue lines denote the exciton with $J_z = \pm 1/2$ (Δ_6). In addition, the solid and dashed lines represent the bright (spin-allowed) and dark

exciton states, respectively. Additionally, we used the energy splitting between (Δ_7) and (Δ_6) excitons under zero field of 0.19 meV in calculation [5]. The energy shift of the lowest bright exciton state is in good agreement with the PL experimental result. As shown in Fig. 4.4(a), the lowest dark exciton state exists below the lowest bright exciton with the energy difference of 0.8 meV (9.3 K in temperature) under 7 T. This energy difference is consistent with the magnetic field effect at high temperature shown in Fig. 4.3(b), where is the PL intensity is almost unchanged by the magnetic field above 10 K. Figure 4.4(b) shows the relative PL intensity as a function of the magnetic field normalized by the intensity under zero field at 1.6 K. By taking into account all energy levels as indicated in Fig. 4.4(a), the relative PL intensity under the magnetic field is expressed by

$$I(B) = \frac{\sum_{\text{bright}} \exp(\frac{\Delta_i}{k_B T})}{\sum_{\text{all}} \exp(\frac{\Delta_i}{k_B T})} \ , \tag{4.2}$$

where Δ_i is the energy difference of the i-th state from the lowest Δ_7 dark exciton state. The result of fitting by eq. 4.2 with the fitting parameter of the temperature is represented in Fig. 4.4(b). The best fitting was obtained with 3.7 K.

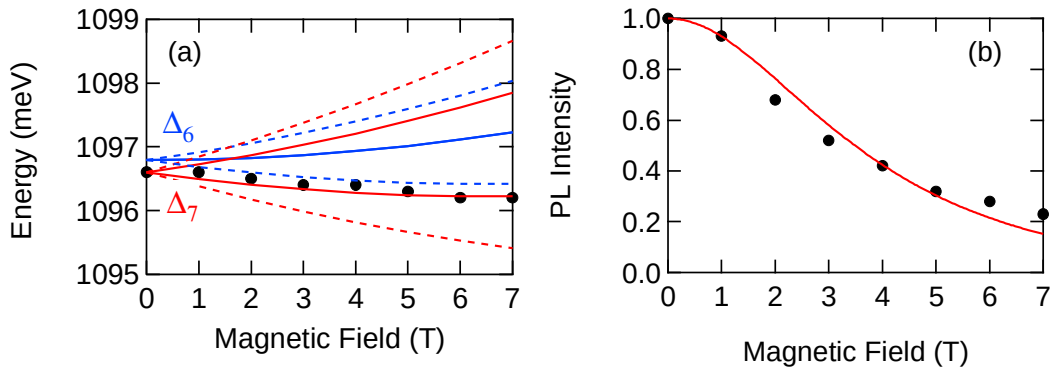

Figure 4.4: (a) The energy of the TO-phonon assisted PL peak as a function of the magnetic field (closed circles) at 1.6 K. The theoretical curves obtained from eq. 4.1 are also shown. The solid (dashed) lines indicate the spin-allowed (spin-forbidden) exciton states. The red (blue) color refer to the $J_z = \pm 3/2$ exciton states (Δ_7) ($J_z = \pm 1/2$ exciton states (Δ_6)). (b) The PL intensity as a function of magnetic field at 1.6 K normalized with that of zero field. The closed circles show the experimental result and the solid line is the fit by eq. 4.2. The fitted temperature was 3.7 K.

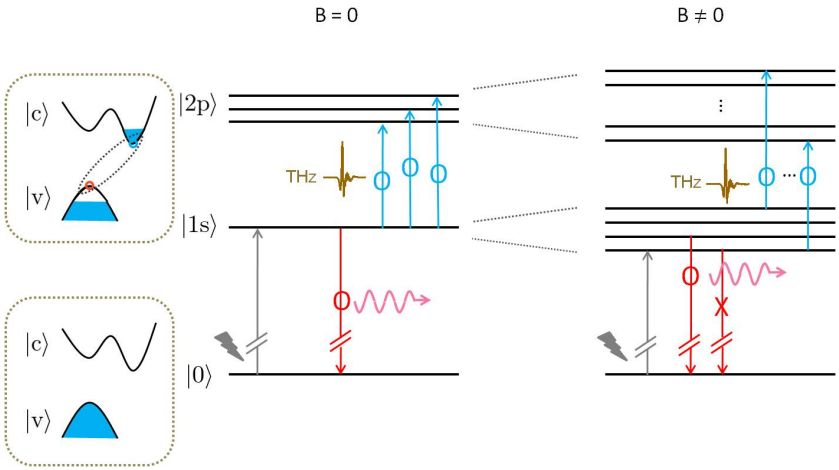

Figure 4.5: The schematic of the energy levels of the excitons without and with the magnetic field. Spin-forbidden excitons can be observed by measuring the intra-exciton transition.

Through the PL measurement, one can concludes that the dark excitons are accumulated under the magnetic field at low temperature which cannot be observed by PL spectroscopy. Therefore, we performed the OPTP spectroscopy. Figure 4.5 shows the schematic of the selection rule for interband and intraband transition.

4.2.2 OPTP spectroscopy

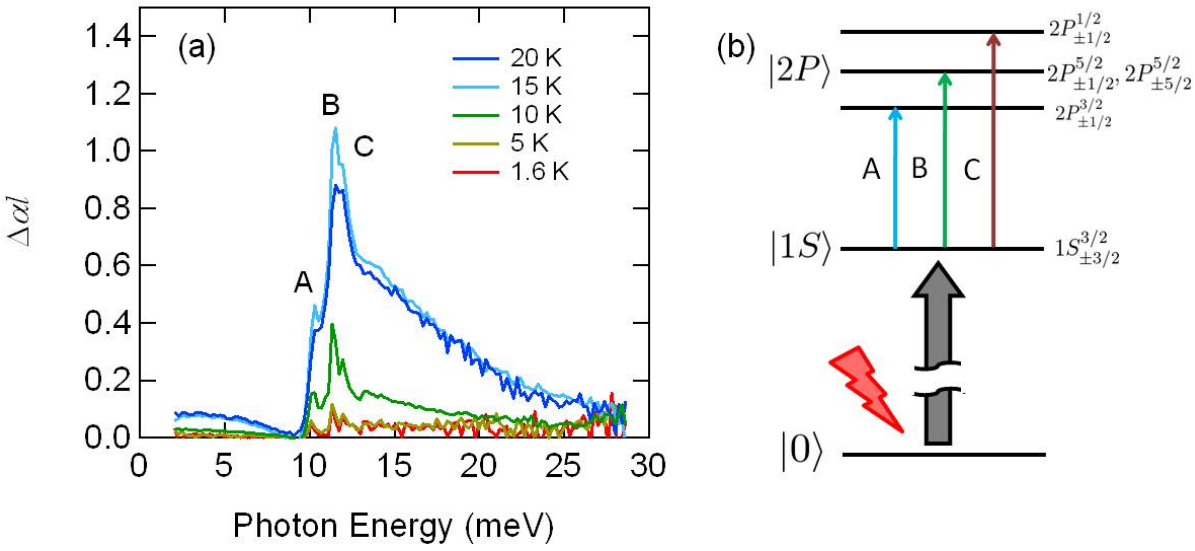

Figure 4.6: The absorption spectra in the steady state under the CW excitation at different temperature.

In contrast to the interband transition, both spin-allowed and spin-forbidden excitons can be observed for the intra-exciton transition. Figure 4.6(a) shows the absorption spectra $\Delta\alpha l \sim -\ln(1 + \Delta T(\omega)/T(\omega))$ under the steady state with the CW excitation of 1.55 eV at different temperature. The change in the reflection loss caused by the optical pumping was neglected. The fine structure of 1S to 2P transition of excitons can be seen in Fig. 4.6(a). Here, we use the representation $nL^F_{F_z}$ introduced by Lipari *et al.* [5], which is already described in the magnetic field effect in Si in Chapter 2. Then three peaks A (10.3 meV), B (11.3 meV), and C (11.9 meV) can be identified as $1S^{3/2}_{\pm 3/2} \rightarrow 2P^{3/2}_{\pm 1/2}$, $\rightarrow 2P^{5/2}_{\pm 1/2}$, $\rightarrow 2P^{5/2}_{\pm 5/2}$, and $\rightarrow 2P^{1/2}_{\pm 1/2}$ (shown in Fig. 4.6(b)) [48]. Besides, a broad absorption above the exciton binding energy also appeared which is attributed to the transition to the continuum states. With the decrease of temperature, each fine structure becomes sharp and the total spectral weight decreases. Next, we observed the magnetic field effect at 1.6 K. Figure 4.7(a) shows the magnetic field effect on the absorption spectra at 1.6 K. At zero magnetic field, the fine structure of 1S to 2P transition of excitons is observed. In addition, the absorption which is attributed to EHD is also seen at high-energy side of the intra-exciton transition. The energy of intra-exciton transition split and shifts by applying the magnetic field. We decomposed the fine structure of intra-exciton transition by the Lorentzian functions shown in Fig. 4.7(a) by black dotted lines. The experimental results are reproduced well by the sum of decomposition Lorentzian functions (blue solid lines in Fig. 4.7(a)). Due to the small binding energy of the $2P$ excitons in Si, the magnetic field effect on the 2 P excitons becomes non-perturbative above 3 T. Therefore, to describe the magnetic effect up to 7 T, we adopt the phenomenological model which is introduced by Nam *et al.* [49]. Then, the magnetic field effect can be written by

$$E(\gamma) = E(0) + \frac{\omega_1\gamma + \omega_2\gamma^2 + \omega_3\omega_4\gamma^3}{1 + \omega_4\gamma^2} \ , \tag{4.3}$$

where γ is the dimensionless parameter introduced in Chapter 2. In the weak field limit ($\gamma \ll 1$), eq. 4.3 results in the perturbation term. For $\gamma \gg 1$, the energy shift is linear to the magnetic field, which corresponds to the Landau level transition regime. Then the coefficients ω_1 and ω_2 correspond to the magnitude of Zeeman splitting and the diamagnetic shift, respectively. Figure 4.7(b) shows the intra-exciton transition energies as a function of the magnetic field. Red, green, and blue solid line pairs represent the fitting result by using eq. 4.3 on the transition A, B, and C in Fig. 4.6(b), which show reasonable agreements with the experimental results. Because the energy of A is the lowest, the magnetic field effect on the transition A does not merge with the higher-order transition. For this reason, the magnetic field effect on the transition A is most identified clearly. From the fitting, the coefficient ω_1 is obtain as 0.04 for the transition A. This value is smaller than the coefficient of the Zeeman splitting calculated by F-representation, indicating the effective g-factor reduces to 0.69.

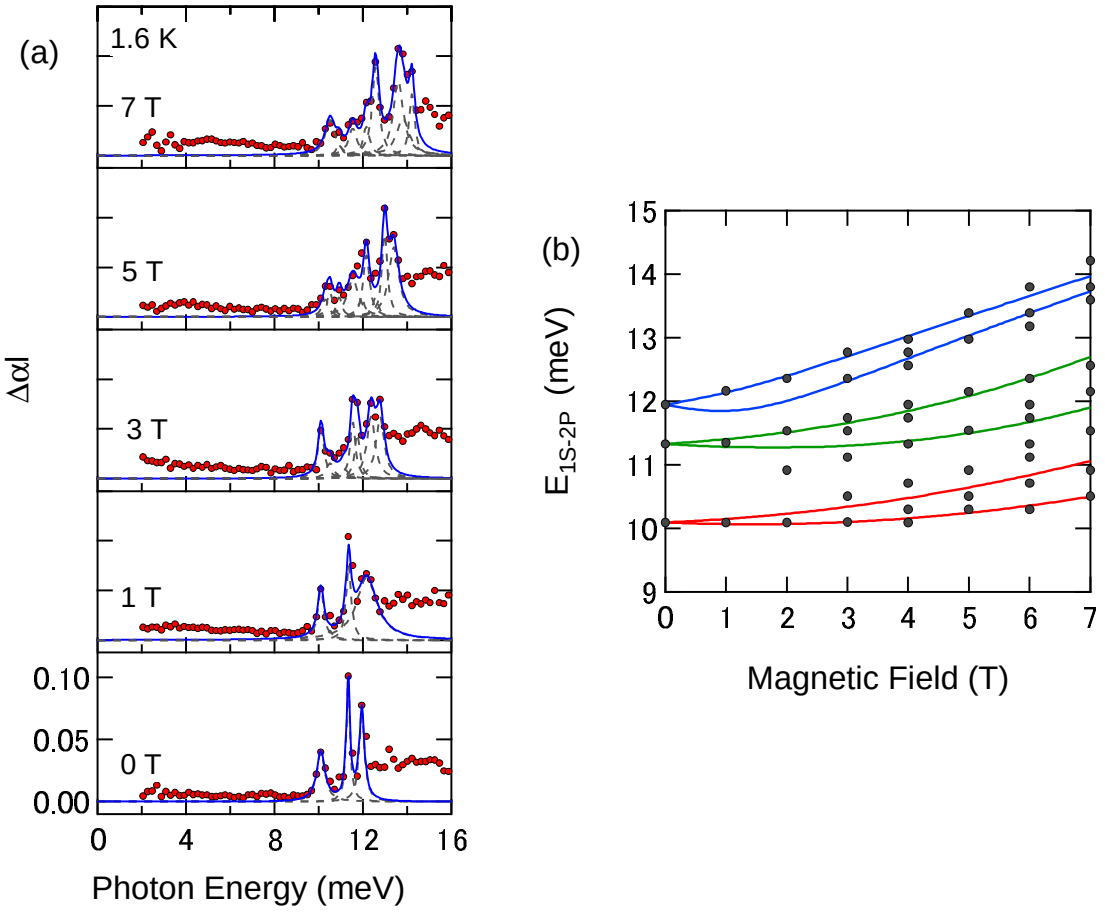

Figure 4.7: (a) The magnetic field effect on the absorption spectra at 1.6 K. Black dotted lines represent the decomposition of each intra-exciton transition by Lorentzian functions. Blue solid lines are the sum of Lorentzian components at each magnetic field. (c) The energies of the intra-exciton transition as a function of the magnetic field. The solid lines represent the fit by using eq. 4.3

4.3 Quasi-CW pump and THz probe spectroscopy

The time delay between the optical pump and THz probe of the conventional OPTP spectroscopy is controlled by optical delay line (shown in Fig. 3.2). However, to make a time delay of 10 ns, the optical path of 3 m is necessary. Therefore, temporal range of this method is limited from picosecond to a few nanoseconds.

To investigate the lifetime of excitons in Si, we developed OPTP spectroscopy system for long temporal dynamics that reaches milliseconds. First, we introduced an additional continuous wave (CW) laser. By chopping the output from the CW laser (800 nm) by an acousto-optic modulator (AOM), we generated chopped quasi-

CW pulses for the optical pump. The duration and delay time of quasi-CW pulse can be controlled by a delay generator which was synchronized with the 1 kHz amplified laser system for the THz-TDS. Since the delay generator was operated by the external trigger from 1 kHz amplified laser system, the maximum of the temporal range was 1 ms in this study. The temporal resolution was 57 ns which was limited by the bandwidth of the AOM (Fig. 4.8). The schematic of the developed system is shown in Fig. 4.9.

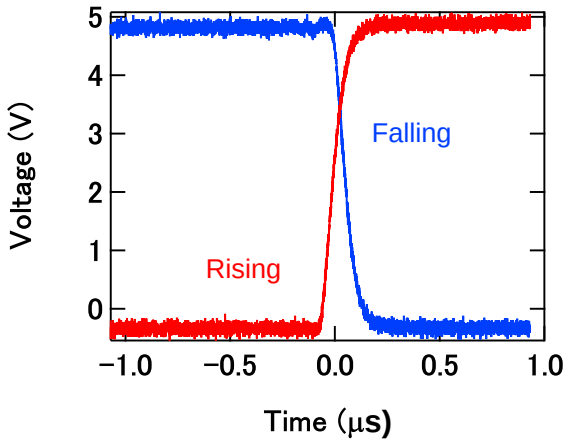

Figure 4.8: Rising time and falling time of AOM.

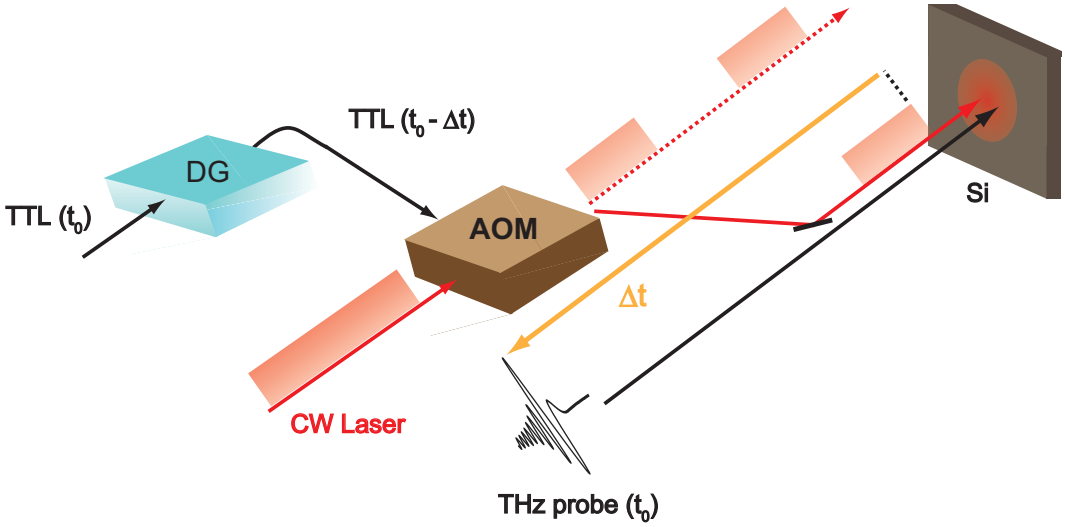

Figure 4.9: Experimental setup for quasi-CW pump and THz probe spectroscopy. E^{opt} being the CW laser source and E^{THz} being the THz probe pulse. Time delay Δt is controlled electrically by the delay generator (DG).

4.3.1 Pile up and relaxation dynamics of free carriers at room temperature

For the demonstration of OPTP spectroscopy in μs regime, we observed the pile up and relaxation of the photoexcited free carriers at room temperature. Figures 4.10(a) and (b) show the differential transmission spectra at pile up and recombination temporal regime, respectively. When the optical pump is turned on, the spectrum attributed to the Drude response of the free carriers is observed. The THz transmittance gradually decreases and reaches a steady state 80 μs after turning on the optical pump, indicating the pileup of photoexcited carriers. After turning off the optical pump, the spectrum recovers within 100 μs. Differential transmission rate at 3 meV is shown in Fig. 4.10(c).

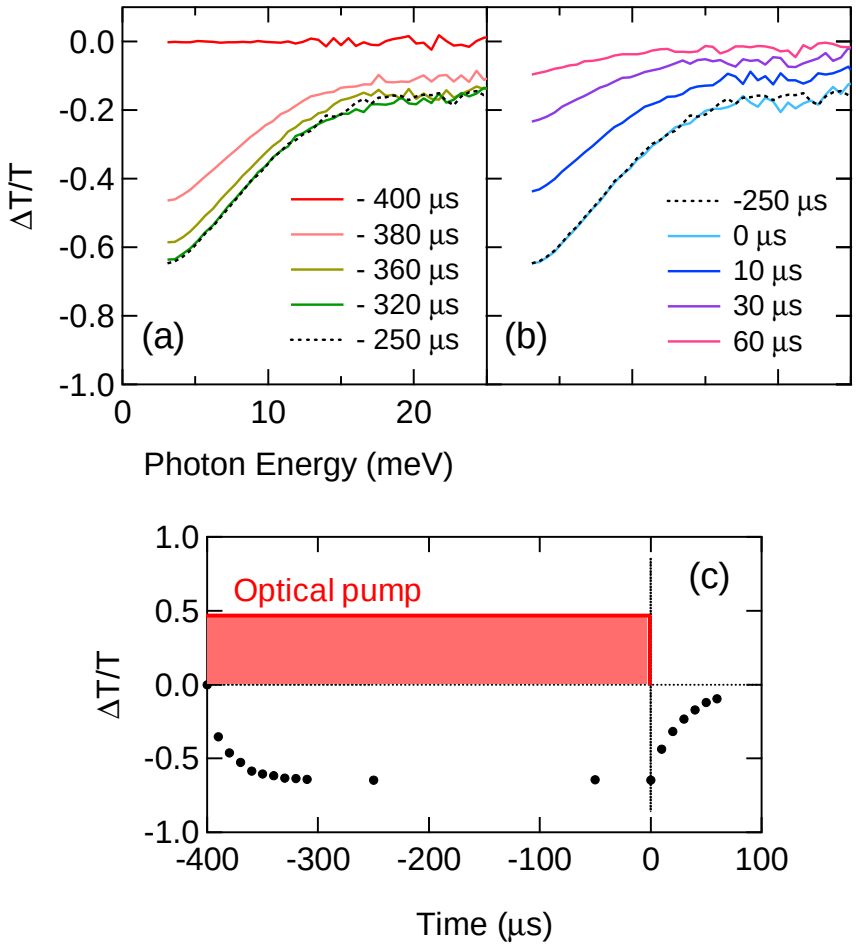

Figure 4.10: Differential transmission spectra at (a) pile up and (b) recombination regime. optical pump was turned on from -400 μs to 0 μs. (c) Differential transmission rate at 3 meV as a function of time. optical pump pulse is also shown.

4.4 Lifetime measurement of exciton by OPTP spectroscopy

By using the developed OPTP spectroscopy system, we investigated the temporal evolution of the excitons in μs regime. Figure 4.11(a) shows the absorption of intra-exciton transition at 10 K at different time delay after the quasi-CW pump turned off. To prevent the temperature increase by the optical pump, the pulse duration of quasi-CW pump was set to 200 μs. After the pump switched off, the absorption disappears in a few μs. For the quantitative discussion, we fitted the temporal evolution of the height of the peak B by the single exponential function. Figure 4.11(b) represents the temporal evolution of the peak B. The markers are experimental results and the solid lines are single exponential fits.

The evaluated exciton decay constants are plotted in Fig. 4.12 as a function of the temperature. We also examined the diffusion of the excitons by solving the diffusion equation with the reported value of the exciton diffusion coefficient $D(T) = (300\ \mathrm{cm^2K^{1/2}/sec})T^{-1/2}$ [50]. Because the effect of the diffusion is negligible in our condition, we ignored the contribution of diffusion (A details, see appendix A). As shown in Fig. 4.12, the decay time decreases below 15 K. It is consistent with the decrease of exciton absorption under steady-state shown in Fig. 4.6. The possible reason would be the trapping of the excitons into the nonradiative recombination centers such as impurities and defects. Indeed, this result is consistent with the previous report [51] which explains the exciton lifetime by the capture, evaporation, and recombination at impurities. Another possible reason might be the formation of electron-hole droplets (EHDs). The formation of EHDs accelerates the nonradiative recombination of the e-h system due to the high Auger recombination rate in EHDs [52, 53]. The collection of free excitons into the EHDs is also observed by PL spectroscopy [54].

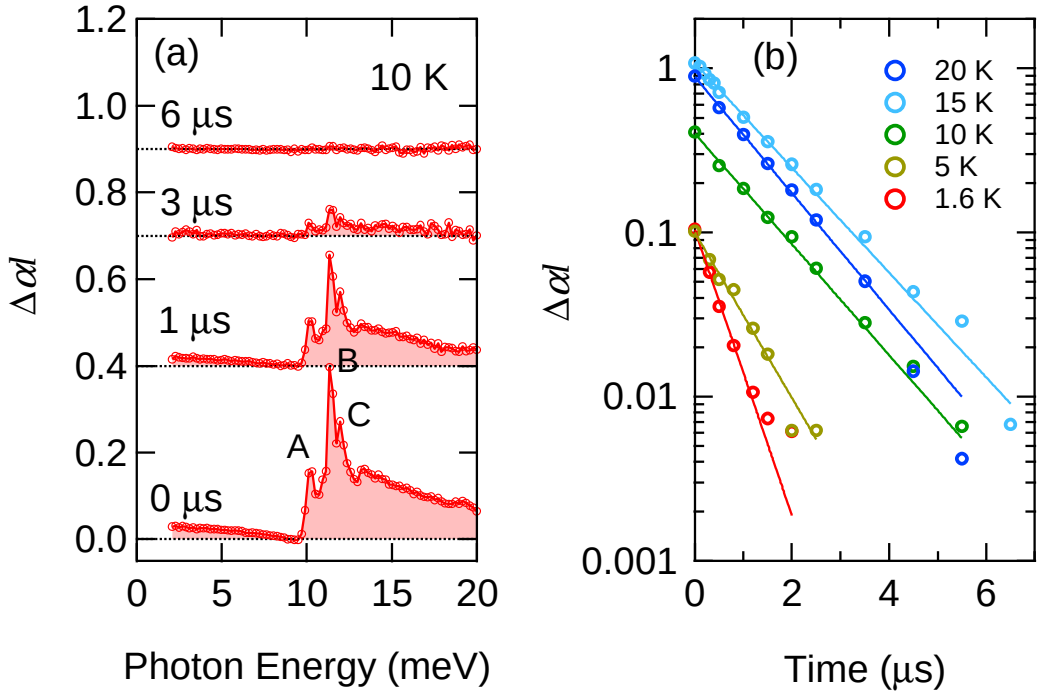

Figure 4.11: (a) Temporal evolution of the absorption spectrum at 10 K after the quasi-CW pump turned off. (b) Temporal evolution of height of peak B from 1.6 K to 20 K. Markers are the experimental results and solid lines are the single exponential fits.

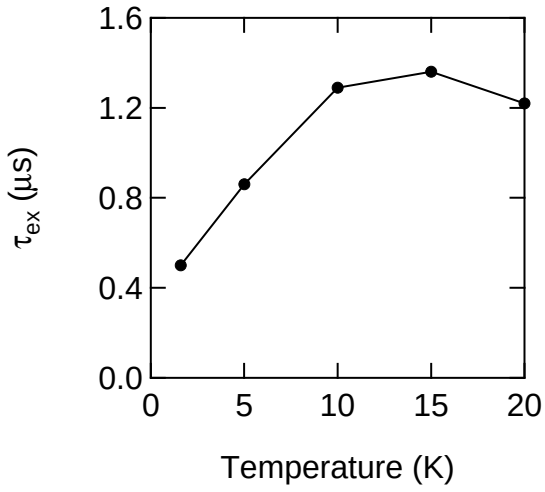

Figure 4.12: Temperature dependence of the exciton decay constant.

In contrast to the behavior below 15 K, the recombination of the excitons at 20 K is faster than that of 15 K. To understand the decrease of the exciton lifetime above 20 K, we investigated the temporal evolution of the population of exciton and free carriers in large temperature range from 1.6 K to 160 K. Figure 4.13 represents the decay constant at the peak B of the excitons and at the 3 meV of the free carriers. The exciton decay constant has a maximum value at 15 K, and decreases with the temperature increase. Besides, the decay constant of the free carriers also decreases with the temperature increase up to 50 K, whereas it increases with the temperature above 50 K.

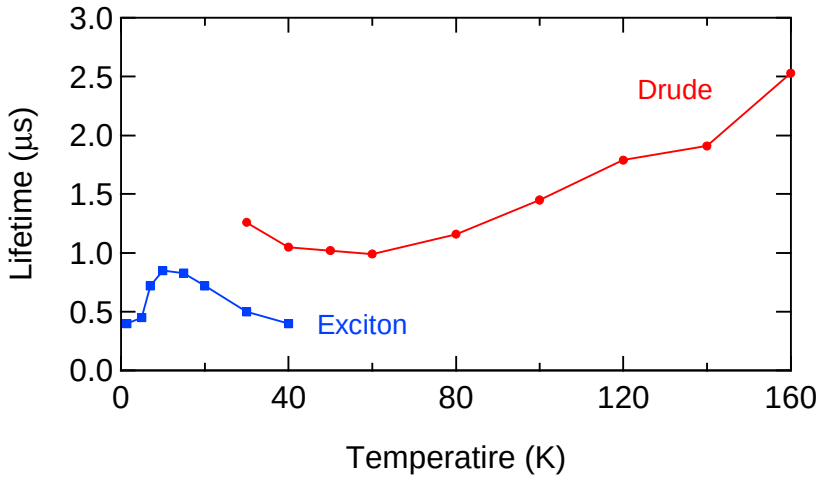

Figure 4.13: Temperature dependence of the decay constant obtained by the peak B of exciton and absorption at 3 meV of free carriers.

To analyze this behavior, we considered the thermal ionization of the excitons to the free carriers. Then, the rate equation for the density of the excitons and the free carriers can be written by [55]

$$\frac{dn_c(t)}{dt} = g - \frac{n_c}{\tau_c} - b_{xc} n_c^2(t) + b_{xc} n_{xc}^* n_{ex}(t) \tag{4.4}$$

$$\frac{dn_{ex}(t)}{dt} = -\frac{n_{ex}}{\tau_{ex}} + b_{xc} n_c^2(t) - b_{xc} n_{xc}^* n_{ex}(t) \ , \tag{4.5}$$

where g is the generation rate, τ_c (τ_{ex}) is the lifetime of the free carriers (excitons), b_{xc} is the cross-section of the formation of the exciton, and

$$n_{xc}^* = D \left(\frac{m^* k_B T}{2\pi\hbar^2} \right)^{3/2} \exp\left(-\frac{E_b}{k_B T} \right) \tag{4.6}$$

is the equilibrium constant. Here, D is the degeneracy, $m_d^* = m_{de} m_{dh} / m_{dex}$ with the density of state mass of the electron m_{de} (hole m_{dh}) and that of the exciton

m_{dex}, and E_b is the binding energy of the excitons. Figures 4.12(a) and (b) show the temporal evolution of the density of the free carriers (FC) and the excitons (FE) at different temperature which is calculated by eq. 4.5. Here, we used the values $D = 1.3$, $m_d^* = 0.12\ m_0$, and $E_b = 14.7$ meV [55]. Also, we used the values $b_{xc} = 1 \times 10^{-3}$ m^3/sec, $\tau_c^{\rm rad} = 1.0\ \mu$s, $\tau_{ex}^{\rm rad} = 1.5\ \mu$s, $n_c(0) = 2 \times 10^{20}$ m^{-3} and $n_{ex}(0) = 1 \times 10^{20}$ m^{-3}. Furthermore, to consider the pump-off condition, g=0 was used.

Figure 4.14(c) shows the calculated decay constants of the free carriers and the excitons as a function of the temperature which are obtained from the single-exponential fits, shown by the black solid lines in Figs. 4.12(a) and (b). This behavior is in good agreement with our experimental result in the temperature range between 20 K and 50 K. Therefore, we conclude that the decrease of lifetime of the excitons above 15 K is due to the thermal ionization to the free carriers.

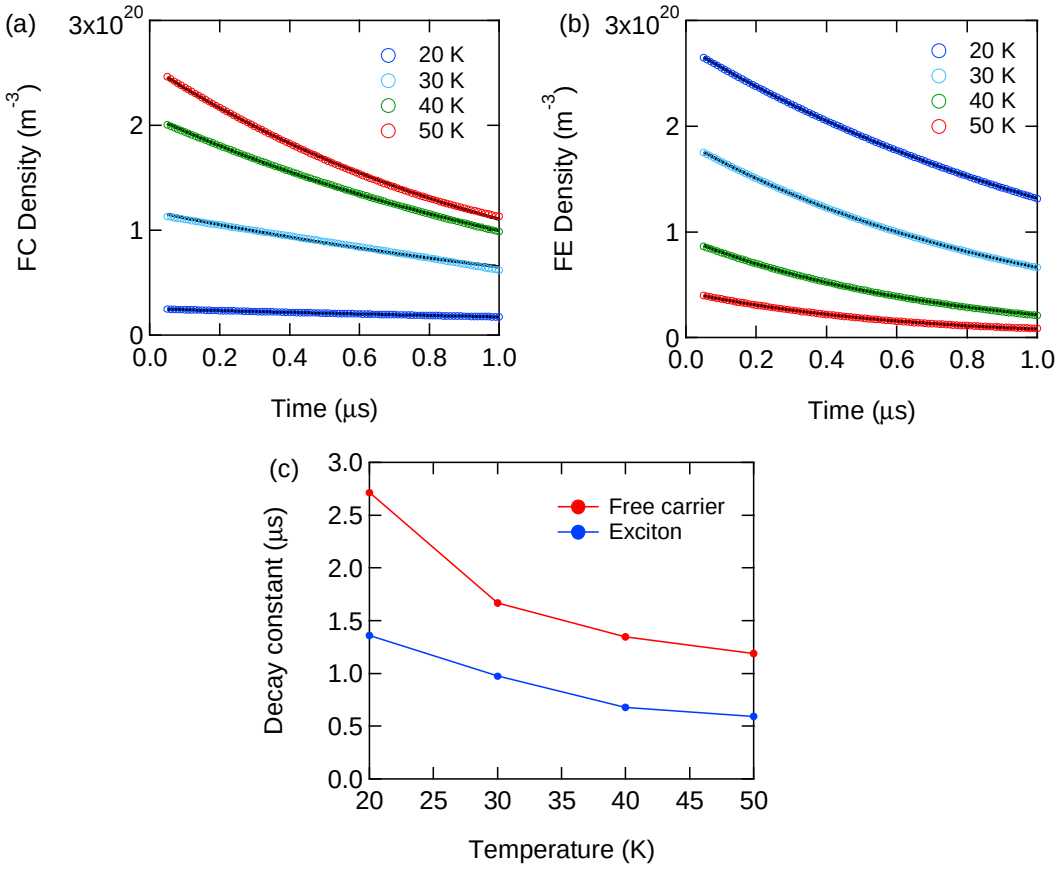

Figure 4.14: Simulation of the temporal evolution of the density of (a) the free carriers and (b) the excitons at different temperature by using eq. 4.5. Open circles are the result of simulation and the black solid lines are single exponential fits. (c) Evaluated lifetimes of the free carriers and the excitons as a function of the temperature.

4.5 Lifetime of spin-forbidden excitons

Figures 4.15(a) and (b) show the absorption spectra of the intra-exciton transitions under zero magnetic field and 7 T, respectively. The shape of absorption spectrum which corresponds to the $1S$ to $2P$ transition is changed by the magnetic field. The details of spectral change under the magnetic field have been discussed previously. Furthermore, the spectral weight of exciton absorption is not reduced even at 7 T.

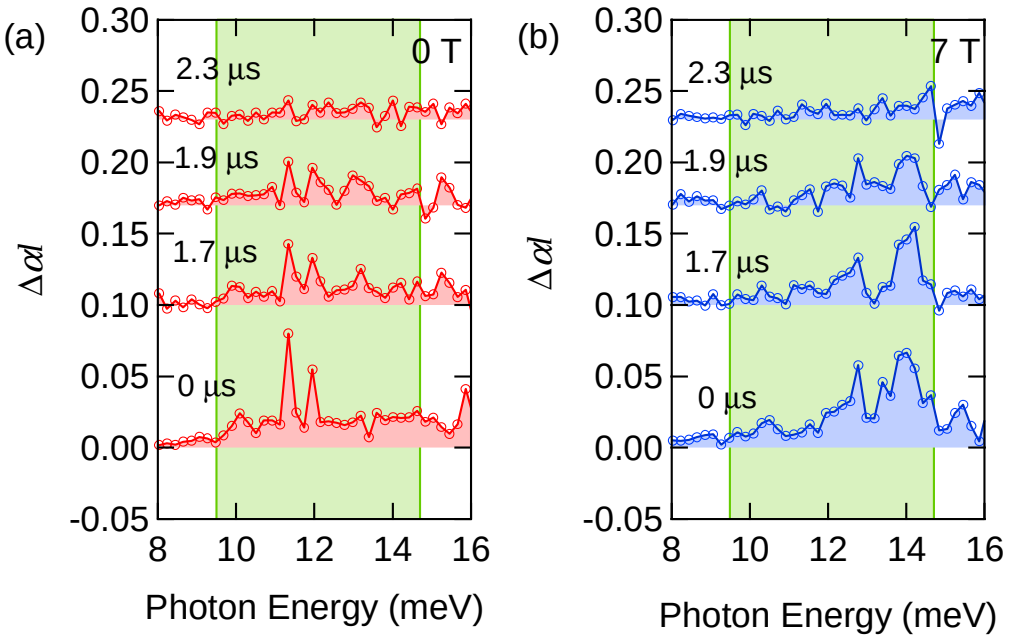

Figure 4.15: Temporal evolution of the absorption spectrum at 1.6 K under (a) zero field and (b) 7 T. Hatched area represents the integration range of the spectrum (9.5 to 14.7 meV) to estimate the lifetime.

From the analysis of the PL intensity, most excitons are considered to accumulate into the lowest dark exciton state. The lifetime of the dark exciton was evaluated by the exponential fit for temporal evolutions of both magnetic field of 0 T and 7 T. Figure 4.16 represents the experimental data and the result of single exponential fit. Here, the experimental data plot the integration of absorption spectrum from 9.5 meV to 14.7 meV (exciton binding energy) to improve the signal to noise ratio. From the exponential fit, the lifetime was estimated to 0.66 ± 0.04 μs for 0 T and 0.63 ± 0.03 μs for 7 T, indicating that the lifetime of dark excitons is not prolonged. Since the spin-orbit interaction in Si is sufficiently small, the radiative recombination rate for the dark excitons should be much smaller than that for the bright excitons. Therefore, this result indicates that the nonradiative recombination process is dominant for the decay of exciton population in the present Si crystal.

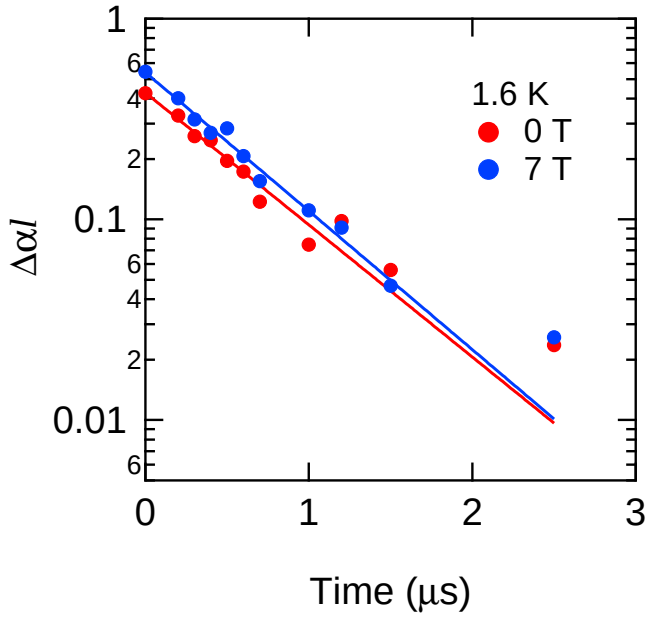

Figure 4.16: The temporal evolution of the integrated spectral weight of the absorption attributed to the intra-exciton transition. The integration range was from 9.5 to 14.7 meV

Note that the above obtained lifetime of bright excitons was slightly longer than that estimated at 1.6 K in Fig. 4.12. Since the quasi-CW pump pulse was set to 400 μs in the present case whereas it was 200 μs in the measurement under zero field, we attribute this difference to the slight increase of temperature of the e-h system caused by the photo-irradiation with a longer duration of the pump pulse.

4.6 Summary

We investigated the magnetic field effect on the excitons in Si by using the PL spectroscopy and the OPTP spectroscopy. In contrast to the PL spectroscopy, the absorption of the excitons does not reduce under the magnetic field. We found that the magnetic field effect on the intra-transition of the excitons becomes non-perturbative above 3 T. We also have developed an OPTP spectroscopy system which enables the study of photoexcited dynamics in a wide temporal region from sub-microsecond to millisecond regime. By using the developed system, we measured the decay dynamics of indirect excitons in Si systematically and we measured the lifetime of the dark excitons which indicates the nonradiative process is dominant for recombination of the excitons in Si.

Chapter 5

Electron and hole system under the magnetic field and uniaxial stress in Si

In this chapter, we experimentally examined the possibility of high density creation of the excitons in Si at low temperature toward the exciton BEC regime by applying the uniaxial stress to suppress the formation of EHD. Also by applying the magnetic field, we tried to lift the spin degeneracy which should increase the critical temperature of the exciton BEC as shown in Fig. 5.1. Indeed, there have been many previous studies for e-h system in Si by PL spectroscopy, absorption or photoconductivity. However, the direct observation of the Drude response, intra-exciton transition and surface plasmon resonance of EHD by THz-TDS can provide us with quantitative information about the e-h system. Therefore, we performed the OPTP spectroscopy on Si under the uniaxial stress and the magnetic field.

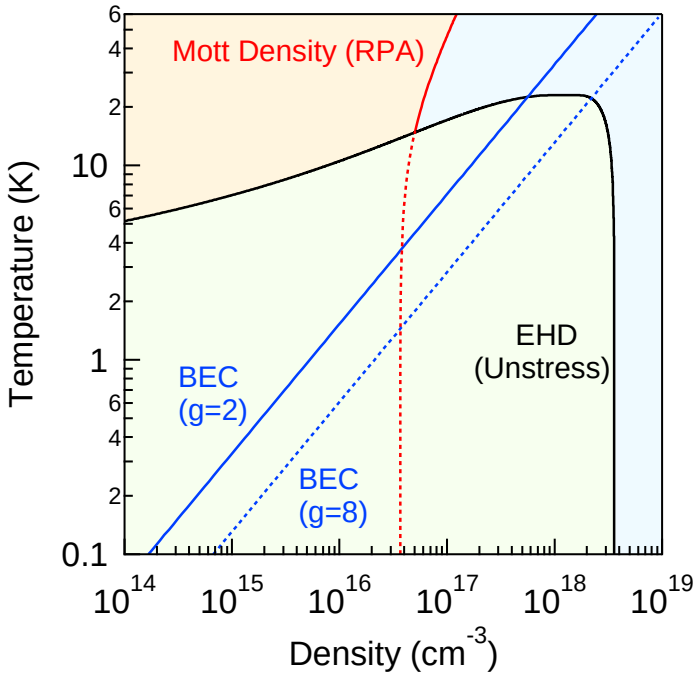

Figure 5.1: Phase diagram of e-h systems in Si. Black solid line represents the coexistence curve of the excitons and EHD and Blue solid (dotted) line is the critical temperature of the exciton BEC with the degeneracy of g = 2 (g = 8). Mott density calculated by random phase approximate theory [56] is also shown.

5.1 Photoexcited dynamics of e-h system in stressed-Si

First, temporal dynamics of photoexcited e-h system in uniaxially-stressed Si was studied. Figure 5.2 represents the change of the dielectric function and the optical conductivity for different delay time t_d between optical pump and THz probe at 5 K under the uniaxial stress along <100> and under zero magnetic field. The excitation power was 8 μJ/cm^2. At t_d =10 ps, the Drude response is observed, indicating that the initial state of photoexcited e-h system is in hot e-h plasma phase. The blue curves at t_d = 10 ps are calculated by the Drude model

$$\epsilon(\omega) = \epsilon_b - \frac{\omega_{\rm p}^2}{\omega(\omega + i\gamma_D)} \ , \tag{5.1}$$

where ϵ_b is the background dielectric constant, γ_D is the damping constant of the free carriers, and $\omega_{\rm pd} = (N_d e^2/\epsilon_0 m^*)^{1/2}$ is the plasma frequency with the free e-h pair density N_d. Here, $\omega_{\rm p}$ = 2.2 THz ($N_d = 7.4 \times 10^{15}$ cm^{-3}) and γ_D = 0.35 THz are used in the fit.

After 300 ps, a Lorentzian structure appears around 12 meV which is attributed to the intra transition of excitons [48], indicating that the initial hot e-h pairs are cooled down and form the excitons. The time scale of cooling dynamics is similar to in unstressed Si which has been reported previously [57]. At $t_d = 300$ ps, the fit by Drude-Lorentz model

$$\epsilon(\omega) = \epsilon_b - \frac{\omega_{\rm p}^2}{\omega(\omega + i\gamma_D)} - \frac{\omega_{\rm pex}^2}{\omega^2 - \omega_0^2 + i\gamma_{ex}\omega} \ , \tag{5.2}$$

is shown as blue solid lines in Fig. 5.2. Here, $\omega_{\rm pex} = (N_{ex}e^2/\epsilon_0 m^*)^{1/2}$ denotes the plasma frequency with the exciton density N_{ex} and the reduced mass of exciton m^*. γ_{ex} is the damping constant for the excitons.

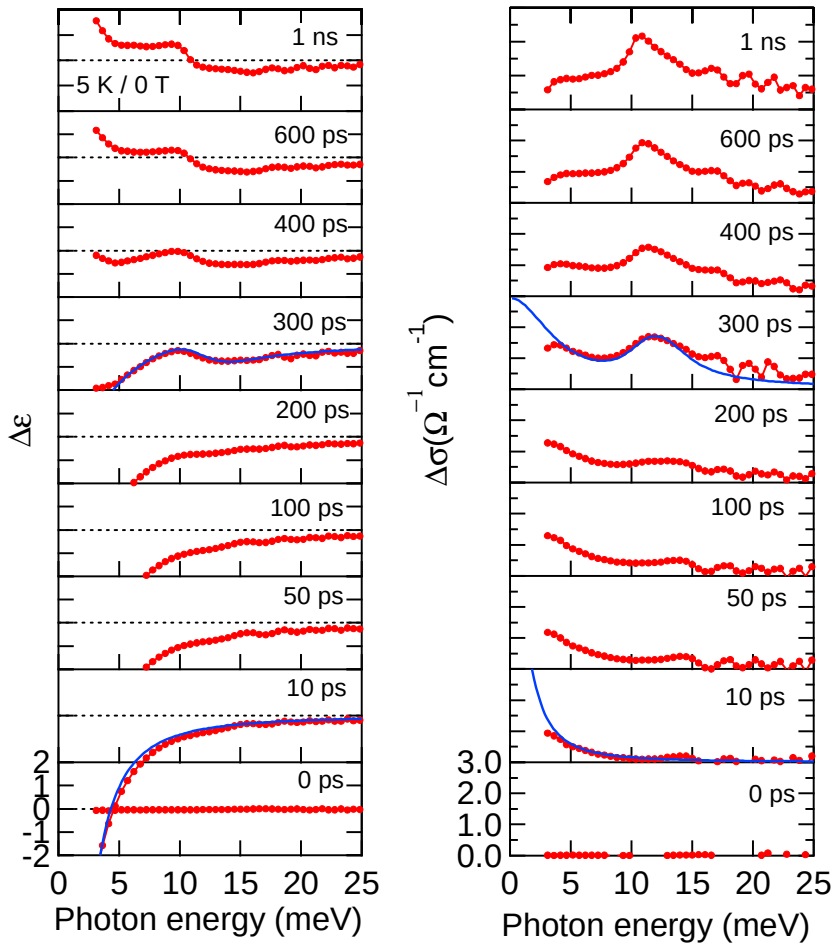

Figure 5.2: Temporal dynamics of the dielectric function and the optical conductivity spectra within 1 ns at 5 K and 0 T. The excitation power was 8 μJ/cm^2. The markers are experimental results. Solid curves represent the fitting results with the Drude model (10 ps) and Drude-Lorentz model (300 ps), respectively.

Note that the dielectric function shows an upturn toward the low-energy side and the optical conductivity seems to converge into zero for ω =0 after t_d =400 ps. This behavior indicates that the overall system becomes insulating after 400 ps. Such a behavior can be understood by taking into account the formation of the EHD [3]. After 400 ps, the spectral feature is conserved, indicating that the system reaches to the quasi-equilibrium state.

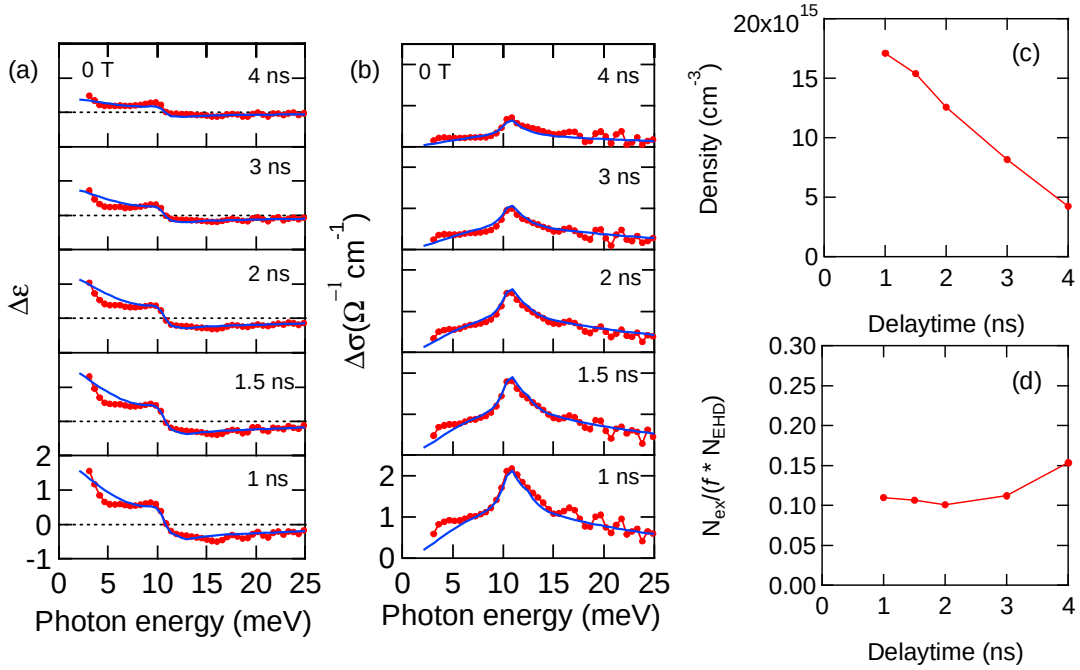

Figure 5.3: Temporal dynamics of the dielectric function and the optical conductivity spectra after 1 ns ((a) and (b)). The experimental condition is same as that in Fig. 5.2. Blue curves represent the fitting by EMT model. (c) The temporal evolution of total density estimated by EMT model. (d) The density ratio between EHD and excitons.

Figures 5.3(a) and (b) show the change of the dielectric function and the optical conductivity from t_d = 1 to 4 ns. The spectra are fitted by the effective medium theory (EMT) given by [58]

$$f\frac{\epsilon_A - \epsilon_{\rm eff}^{\rm Br}}{\epsilon_A + 2\epsilon_{\rm eff}^{\rm Br}} + (1-f)\frac{\epsilon_B - \epsilon_{\rm eff}^{\rm Br}}{\epsilon_B + 2\epsilon_{\rm eff}^{\rm Br}} = 0 \tag{5.3}$$

$$\epsilon_A = \epsilon_b - \sum_i \frac{e^2 N_{1{\rm S}-i{\rm P}}}{\epsilon_0 m_{\rm ex}} \frac{1}{(\omega - \omega_i) + i\gamma_{\rm ex}} \tag{5.4}$$

$$\epsilon_B = \epsilon_b - \omega_{\rm p}^2 \frac{1}{\omega(\omega - i\gamma_{\rm EHD})} \ , \tag{5.5}$$

where f denotes the volume fraction of EHD and $N_{1{\rm S}-i{\rm P}}$ is the exciton density which is determined from intra transition of the excitons and

$$\omega_{\rm p}^2 = \frac{N_{\rm EHD} e^2}{\varepsilon_0 m^*} \tag{5.6}$$

is the plasma frequency. Here, $N_{\rm EHD}$ denotes the density of e-h pairs inside the EHD, e is the charge of the electron, ε_0 is the permittivity of free space, and m^* is the reduced mass of e-h pair ($\frac{1}{m^*} = \frac{1}{m_e} + \frac{1}{m_h}$). Furthermore, the surface plasmon resonance (SPR) of EHD which is given by [59]

$$\omega_{\rm SPR} = \frac{\omega_{\rm p}}{\sqrt{3\varepsilon_b}} \ , \tag{5.7}$$

where ε_b is the background relative permittivity of medium. From this relation, one can see that the SPR frequency depends on the density of e-h pairs inside the EHD. Under the ambient pressure, SPR frequency of EHD in Si exists at 34 meV with the e-h pair density of 3×10^{18} cm^{-3} [6],

Here, we consider the intra-exciton transition from 1S to 2P and from 1S to 3P [26]. From eqs. 5.4 and 5.5, the densities of excitons and EHD can be estimated. With using $m_{ex} = m^* = 0.123\ m_0$ [21], the density inside EHD is estimated as $N_{\rm EHD} = 3.3 \times 10^{17}$ cm^{-3}, indicating that the band degeneracy is lifted from [6,2] to [2,1] by applying uniaxial stress [24]. Therefore, the estimated carrier density of 3.3×10^{17} cm^{-3} inside EHD indicates that the infinite-stress limit is realized ($>$ 300 MPa). Even though the applied stress may not be spatially uniform, in such a high stress limit, the stress distribution does not impinge to the uniaxial stress effect. Figures 5.3(c) and (d) show the total density $N_{\rm ex} + fN_{\rm EHD}$ and the density ratio $N_{\rm ex}/fN_{\rm EHD}$, respectively ($N_{\rm ex} = \sum_i N_{1{\rm S}-i{\rm P}}$, $i = 2, 3$). Figure 5.3(c) shows that the lifetime of photoexcited e-h pairs significantly decreases under the uniaxial stress. The reason is not clear at present. From Fig. 5.3(d), it can be seen that the total density decreases with keeping constant density ratio between the excitons and EHDs. A constant ratio between the excitons and the EHD indicates that the system has reached to the quasi-equilibrium state. The sharp intra-exciton transition sustains with EHD even at 4 ns. This behavior is completely different from the case of unstressed Si [3], where the excitons are completely absorbed into EHDs after 4 ns. This different can be attributed to the reduction of volume fraction of the EHD under the uniaxial stress.

5.2 Excitation power dependence

Next, we investigated the excitation power dependence systematically. Figures 5.4(a) and (b) show the change of the dielectric function and the optical conductivity for different excitation power I. The weakest excitation power was $I_0 = 10\ \mu$J/cm^2. At low excitation region, the sharp structure can be seen around 11 meV. This

structure is 1S to 2P transition of exciton [26]. Besides, the broad structure appears over all spectral range, which is attributed to SPR of EHD. With the increase of excitation power, the EHD becomes dominant, and the intra-exciton transition broadens while keeping its resonant energy. Further, under the high excitation region above 200 μJ/cm^2, the low-energy side of the dielectric function is turned to negative and the optical conductivity in the low energy limit increases to finite values. This indicates that the system is changed to metallic state which has the finite DC conductivity. This phenomenon can be understood by the percolation. When the density of the metallic clusters is small, the clusters behave (spatially) independently. However, when the density exceeds the percolation threshold, the long-range percolation path appears. Now, we apply this cluster model to EHD. At low density region, the system is insulating because the EHDs are separated. With the density increase, the connections between EHDs may be formed, and the conduction path appears. In the case of three dimensional sphere, the percolation threshold is 0.289573 [60]. Therefore, we can consider that the volume fraction of EHD exceeds about 0.3 above 200 μJ/cm^2.

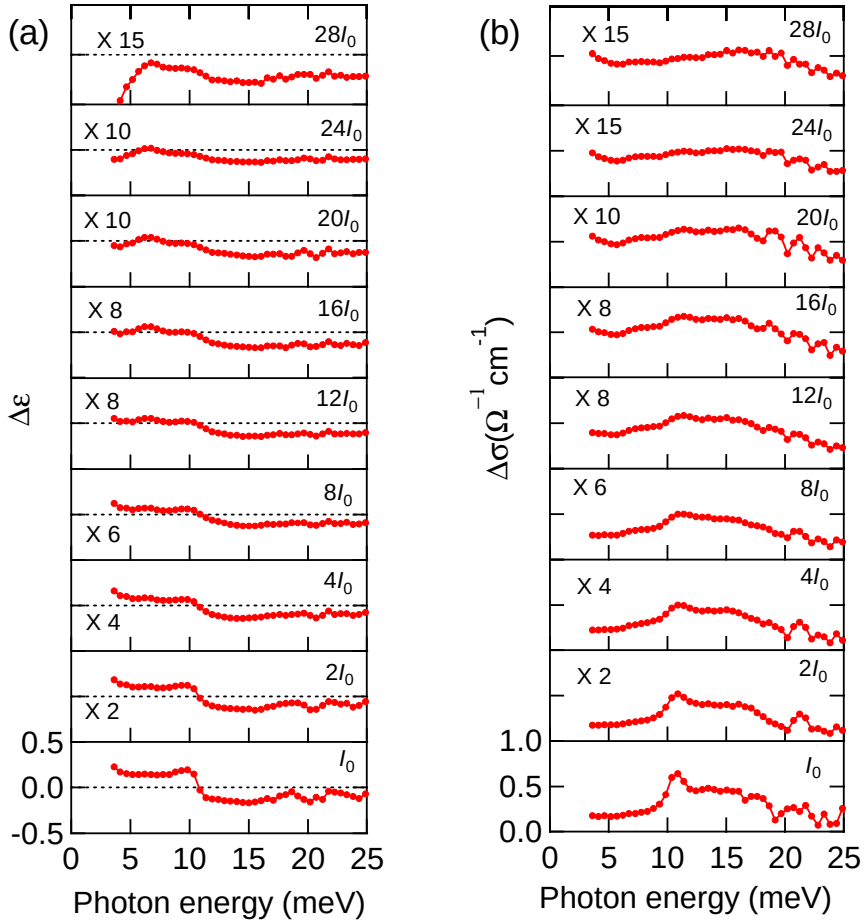

Figure 5.4: (a) The dielectric function and (b) the optical conductivity spectra at 0 T. The weakest excitation power is 10 μJ/cm^2 which is denoted by I_0. The delay time between the optical pump pulse and the THz probe pulse is 4 ns.

To evaluate the exciton density quantitatively, we have separated the exciton component from the optical conductivity spectrum as shown in Fig. 5.5. EHD component is evaluated by EMT (filled curves in Fig. 5.5.) and $1S$-$2P$ transition of excitons is evaluated by Lorentzian functions (the red curves in Fig. 5.5.) [26]. To reproduce experimental results, we must add additional Lorentzian function at 12 and 16 meV. The 12 meV line could be attributed to the transitions of 1S excitons to the higher Rydberg states, whereas the origin of 16 meV line is unclear at present. The intra transitions of bound excitons may be one possible origin. However, their excitation-power dependence should be saturated in such a high density region. Since the spectral weight of the additional peak increases with the increase of excitation power, we concluded the peak around 16 meV is not attributed to the bound excitons.

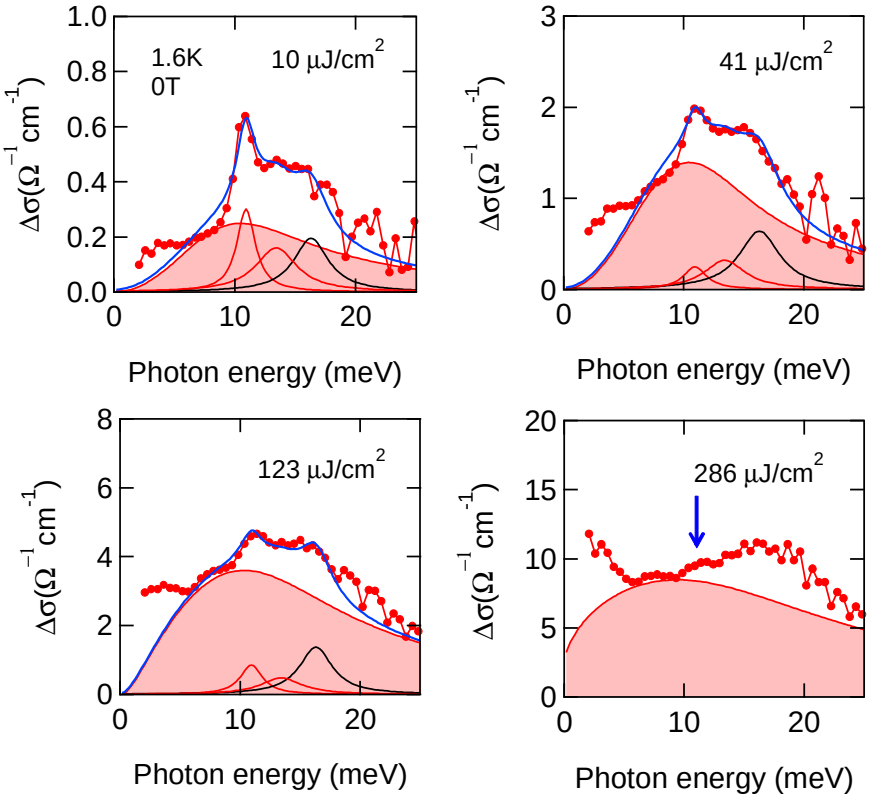

Figure 5.5: Optical conductivity spectra at 0 T. Markers are experimental results. Solid curves represent the theoretical calculation from effective medium theory (filled), Lorentzians (red), and sum of theoretical curves (blue). Excitation powers are shown in figures.

We compared the experimental result with the sum of theoretical curves represented in Fig. 5.5 by blue solid lines. One can see the experimental results can be reasonably reproduced by theoretical curves below 123 μJ/cm^2, except the low-energy regime. At the high density regime above 123 μJ/cm^2, the quantitative evaluation is difficult because of the EMT analysis is invalid at the large volume fraction of EHD. Therefore, we evaluated the exciton density from 10 to 123 μJ/cm^2. Figure 5.6(a) shows the components of intra-transition of excitons, and Fig. 5.6(b)-(d) show the estimated exciton density as a function of the excitation power at 1.6, 5, and 10 K. From Fig. 5.6(b)-(d), it can be seen that the excitons of 2×10^{15} cm^{-3} are accumulated and the exciton density slightly increases with the increase of excitation power. This sub-linear power dependence of exciton density suggests that the photoexcited e-h pairs are collected by EHD in the high density region.

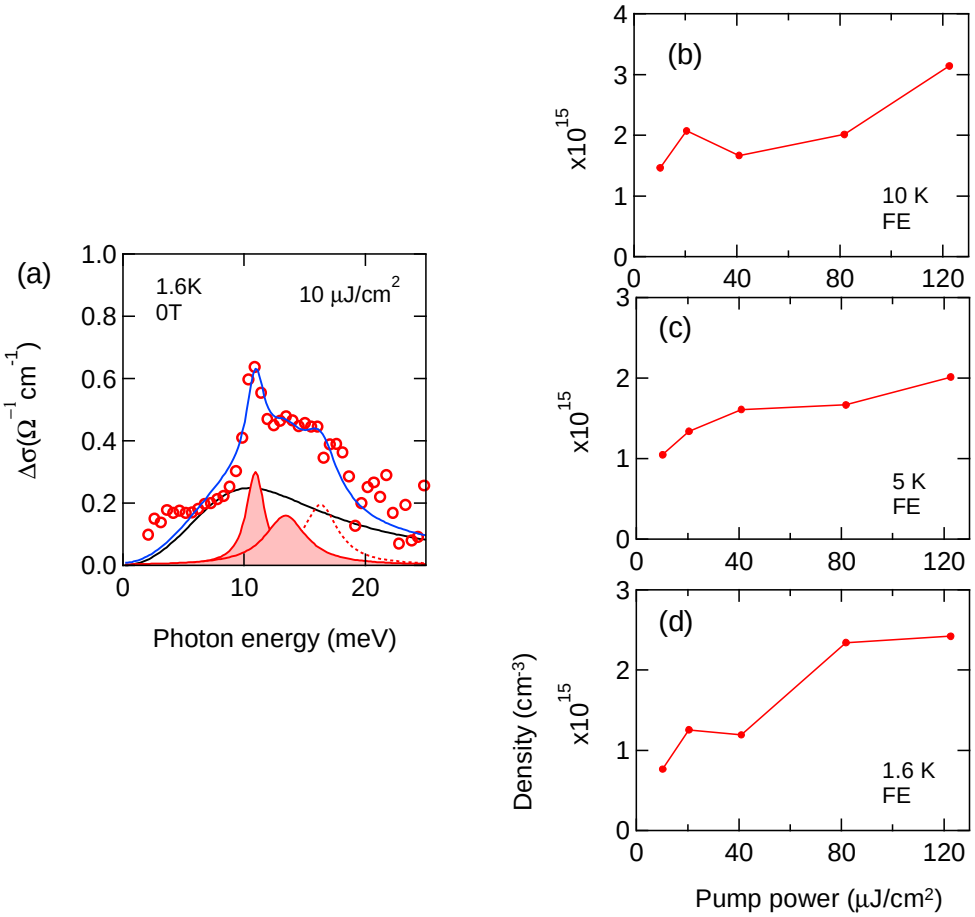

Figure 5.6: (a) Exciton component in the optical conductivity spectrum. Open circles are the experimental result, black curve is the EHD component estimated by EMT, red-filled curves are the intra-exciton transitions fitted by Lorentzian functions, red-dashed curve is the additional component to reproduce spectral feature, and blue curve is the sum of fitting curves of all components. (b)-(d) Estimated exciton density from Lorentzian fitting (filled area in (a)) as a function of the excitation power. The pump-probe delay is 4 ns.

5.3 Density of the excitons under the magnetic field

As mentioned previously, the lift of degeneracy of the excitons is important to increase the critical temperature of the exciton BEC. In this study, we lifted the band degeneracy of the excitons from [6,2] to [2,1] by applying uniaxial stress. Furthermore, the spin degeneracy of exciton is lifted by applying the magnetic field. Under the magnetic field stronger than 2 T, the spin degeneracy is lifted at the temperature

of 1.6 K as discussed in Chapter 4. Then, finally the excitons with the degeneracy of 2 fold are realized. Therefore, we applied the magnetic field up to 7 T to accumulate the lowest energy dark excitons. Figure 5.7 shows the optical conductivity spectra with and without the magnetic field of 7 T at the excitation power of 10 μJ/cm^2 (upper side) and 123 μJ/cm^2 (lower side). The intra-exciton transition energy is changed by the Zeeman splitting and the diamagnetic shift [36]. The 1S to 2P transition of exciton shift to 13 meV by the applying the magnetic field of 7 T. The SPR of EHD does not change significantly by the magnetic field, i. e. the density inside the EHD remains constant against the magnetic field. Since the Zeeman splitting of each 1S to 2P transition of the excitons are small (< 0.2 meV), here we evaluated the 1S to 2P transition by single Lorentzian. In Fig. 5.7, each solid line denotes same curves in Fig. 5.5. The unknown peak around 16 meV does not depend on the magnetic field.

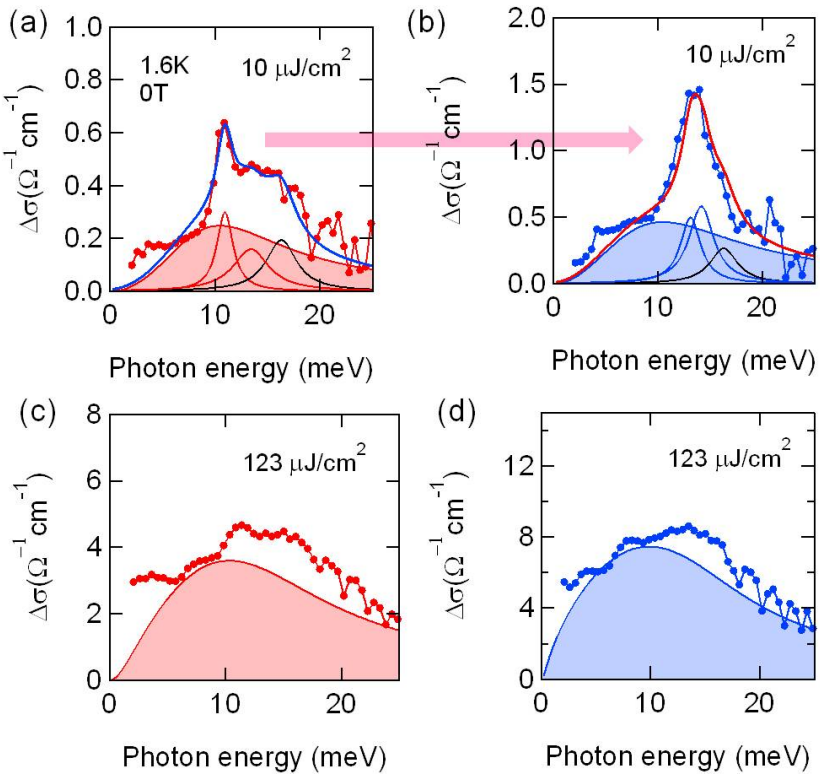

Figure 5.7: Optical conductivity spectra at 0 T ((a),(c)) and 7 T ((b),(d)), respectively. Upper (Lower) side shows low (high) excitation regime. Filled curves are calculation by the effective medium theory.

From the spectral weight of intra-exciton transition, we evaluated the density of the excitons. We also performed the experiment and the analysis at 5 and 10 K. Figure 5.8 shows the exciton density with and without the magnetic field of 7 T. One

can see that the density of the excitons increases under the magnetic field at whole temperature. From the spectral analysis, not only the density of the excitons but also that of EHD increases under the magnetic field. Even in the initial temporal region of 50 ps after the photoexcitation, we observed the increase of Drude weight with applying the magnetic field. Therefore, we attribute this increase of the e-h pair density to the modification of above-gap transition probability is caused by the magnetic field.

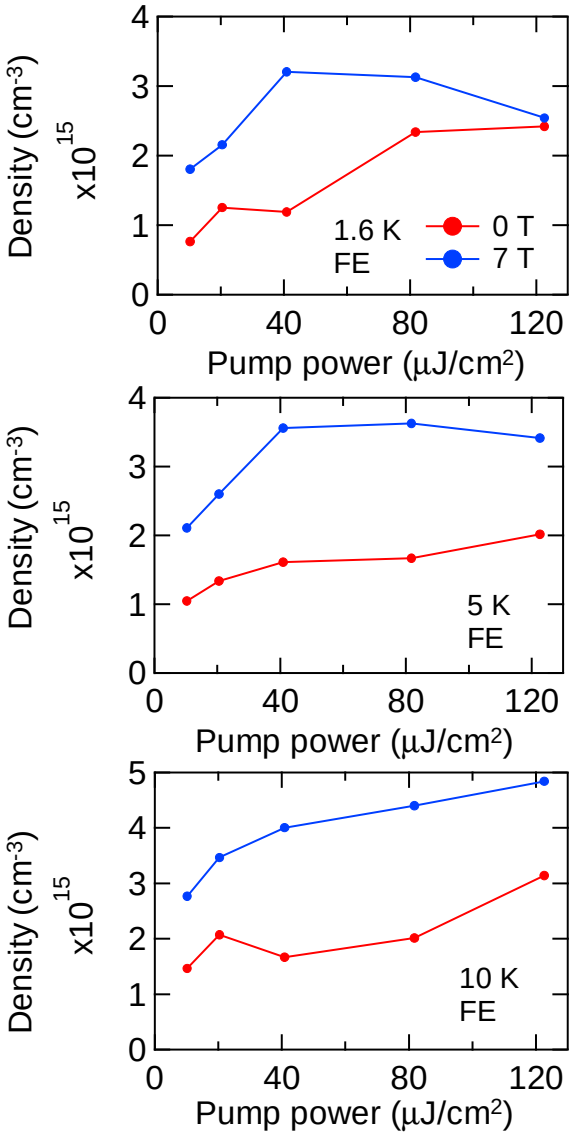

Figure 5.8: Density of excitons under zero field (red) and the magnetic field of 7 T (blue) as a function of the excitation power at 1.6 K (upper), 5 K (middle), and 10 K (lower).

Figure 5.9 shows the experimental results in the phase diagram. First, the reduction of the critical e-h pair density for the EHD is realized by applying the uniaxial stress. As shown by black arrow in Fig. 5.9, the density inside EHD is reduced from 3×10^{18} cm^{-3} to 3×10^{17} cm^{-3}. Green markers represent the experimental result estimated by EMT. Second, the excitons survival is observed with the relatively high density of 3×10^{15} cm^{-3}, which locates inside the coexistence curve even in the thermal-equilibrium condition. Assuming that the thermal equilibrium between the excitons and EHDs are realized, the density of the excitons can be written by [24]

$$N_{\mathrm{ex}}(T) = g \left(\frac{m_{ex} k_B T}{2\pi\hbar^2} \right)^{3/2} \exp\left(-\frac{\phi}{k_B T} \right), \tag{5.8}$$

where g is the degeneracy factor of the excitons, m_{ex} is the mass of the excitons, and ϕ is the work function of EHD. From eq. 5.8, the density of the excitons is calculated to be less than 10^{10} cm^{-3} at 1.6 K with $m_{ex} = 0.5\ m_0$ and $\phi = 2.2$ meV [24]. The experimentally realized exciton density of 3×10^{15} cm^{-3} is far above this density, indicating that the e-h system is not in the thermal equilibrium state. On the other hand, the spectral analysis in Fig. 5.3 shows that the density ratio of the excitons and EHDs hardly changes after 1 ns, indicating that the e-h system reached in a quasi-steady state. The shortening of e-h pair lifetime under the uniaxial stress may explain such behavior. Because of such a short lifetime, EHDs cannot grow enough by absorbing the excitons to reach the thermal equilibrium, and thus the relatively large density of the excitons is achieved. Furthermore, as shown by blue arrow in Fig. 5.9, the increase of critical temperature for the exciton BEC is expected under the magnetic field by lifting the spin degeneracy. The blue dotted line represents the critical temperature of the exciton BEC of the spin-degenerated excitons (i. e. in the absence of the magnetic field), and the blue solid line is that of the spin-degeneracy-lifted exciton (in the presence of the magnetic field). Also, the red markers and blue markers represent the experimentally evaluated of the exciton density. It can be seen that the realized exciton density appreciably approaches to critical curve of the exciton BEC. With the density of 3×10^{15} cm^{-3}, the critical temperature of the exciton BEC is expected as 0.7 K.

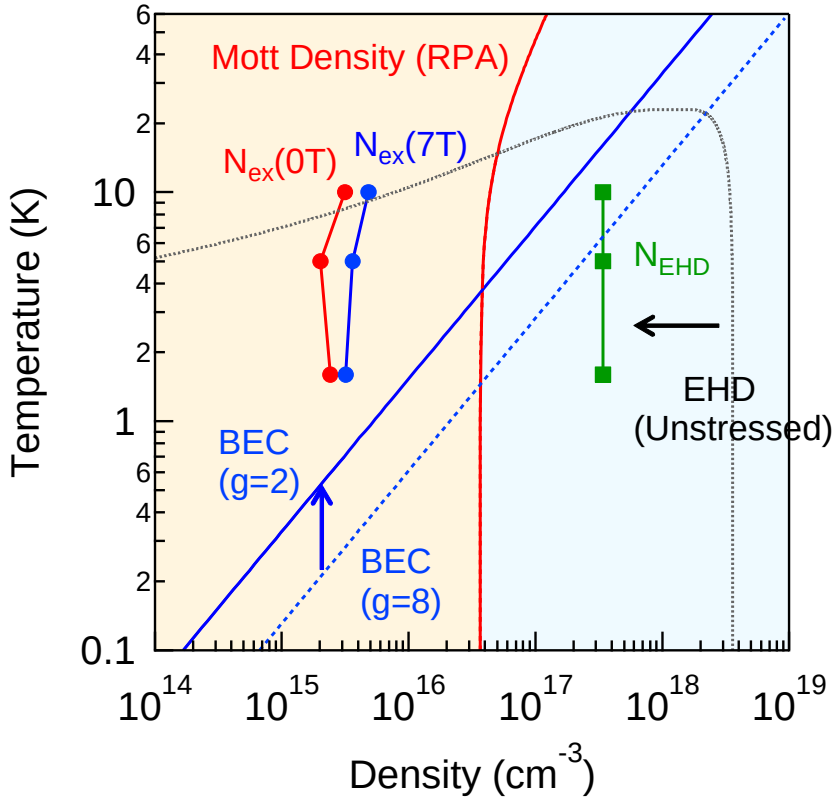

Figure 5.9: Experimental results in the phase diagram. Red and blue circles represent maximum density of excitons under zero field and 7 T, respectively. Green squares are the density inside EHDs. Black arrow shows the reduction of the density inside EHD by applying uniaxial stress and blue arrow the increase of the critical temperature of the exciton BEC by applying the magnetic field.

5.4 Summary

We performed OPTP spectroscopy in the uniaxially-stressed Si. Under the uniaxial stress along <100>, the decreasing of e-h pair density inside the EHD from 3×10^{18} cm^{-3} to 3×10^{17} cm^{-3} is confirmed through the shift of SPR of EHD, which indicates that the band degeneracy is lifted. Further, by applying the magnetic field, it is expected that the spin degeneracy is lifted. Then, the total degeneracy of exciton decreases significantly from 48 to 2. Under the uniaxial stress, we measured the formation and decay dynamics of the excitons and the EHD. The excitons and EHD are formed and reach to the quasi-equilibrium state during few hundred ps after the optical excitation. The time scale of the formation dynamics is similar to that of unstressed Si [3]. However, in the case of stressed Si, the intra-exciton transition sustains even at 4 ns after the photoexcitation. This behavior is completely different

to the case of unstressed Si. Next, from the excitation power dependence, the surviving of cold excitons against the absorption into EHD is investigated. As a result, intermediate exciton density region is realized at very low temperature far below T_c of EHD. From the estimation by EMT and Lorentzian fitting, excitons of 3×10^{15} cm^{-3} are accumulated under the magnetic field of 7 T even at 1.6 K. The critical temperature of the exciton BEC at the density is estimated as 0.7 K with the degeneracy of g=2, which is still below the lowest temperature of the present experimental apparatus, 1.2 K. Yet, the temperature of 0.7 K would be experimentally the feasible range.

Chapter 6

Electron and hole system under the magnetic field and an uniaxial stress in Ge

The conduction band minima of Ge is located at L point and it is four-fold degenerated. By applying the uniaxial stress, the band degeneracy of Ge can be reduced from [4,2] to [1,1]. This character is beneficial for the research of exciton BEC. In addition, since the density of state mass is 0.2198 m_0 for electrons and 0.088 m_0 for holes [21], it is possible to realize the strong magnetic field limit where both electrons and holes stay only in the lowest Landau level with the moderate magnetic field of 3 T. In this chapter, we will discuss about the OPTP spectroscopy on the e-h system in Ge under uniaxial stress and the magnetic field.

6.1 Sample and experimental setup

High resistivity Ge of (111) surface with the thickness of 40 μm was used as a sample. The resistivity was about 5 Ω cm.

For the OPTP spectroscopy of the e-h system in Ge, we used the experimental setup described in chapter 3. In the case of Ge, the direct transition occurs by the optical pump of the photon energy of 1.55 eV (800 nm). Then, the distribution of the e-h system becomes inhomogeneous in the depth direction because the thickness of our sample (40 μm) is much thicker than the penetration depth of the wavelength of 800 nm (< 1 μm). Therefore, to make homogeneous distribution, we used long-wavelength optical pulse of 1450 nm (0.86 eV) and 1500 nm (0.83 eV) which is generated by Optical Parametric Amplifier (OPA; OPerA Solo, Coherent Inc.) as the optical pump. Then, the penetration depths of the photon energy of optical pump (0.86 and 0.83 eV), which is between the direct gap energy (0.898 eV at 1.5 K [14]) and the indirect gap energy (0.744 eV at 1.5 K [14]), are estimated to 300 μm for the optical pump of 1450 nm, and 1000 μm for the optical pump of 1500 nm, respectively [11]. These penetration depths are longer than the sample thickness.

6.2 Evaluation of e-h pair density at high temperature under the uniaxial stress

For the evaluation of photoexcited e-h pair density, we measured complex dielectric function spectrum at high temperature 50 K and zero magnetic field. The time delay between the optical pump pulse and the THz probe pulse was 5 ns. We used an optical pulse of the wavelength of 1450 nm as the optical pump. In such a high temperature, the excitons are thermally ionized. At such high temperature, we can evaluate the density of photoexcited carriers by Drude model fits. Figure 6.1(a) shows the change of the dielectric function (upper panel) and the optical conductivity (lower panel) spectra. The markers represent the experimental results and the solid lines are the fitting curves obtained by the Drude model $\epsilon(\omega) = \epsilon_b - \omega_{\rm pd}^2/(\omega(\omega + i\gamma_D))$. Then, the carrier density can be determined from $\omega_{\rm p} = (N_d e^2/\epsilon_0 m^*)^{1/2}$, with $m^* = 0.046\ m_0$ the reduced mass of electrons and holes. The estimated carrier density is shown in Fig. 6.1(b) as a function of the excitation power. The photoexcited carrier density shows a linear dependence on the pump power.

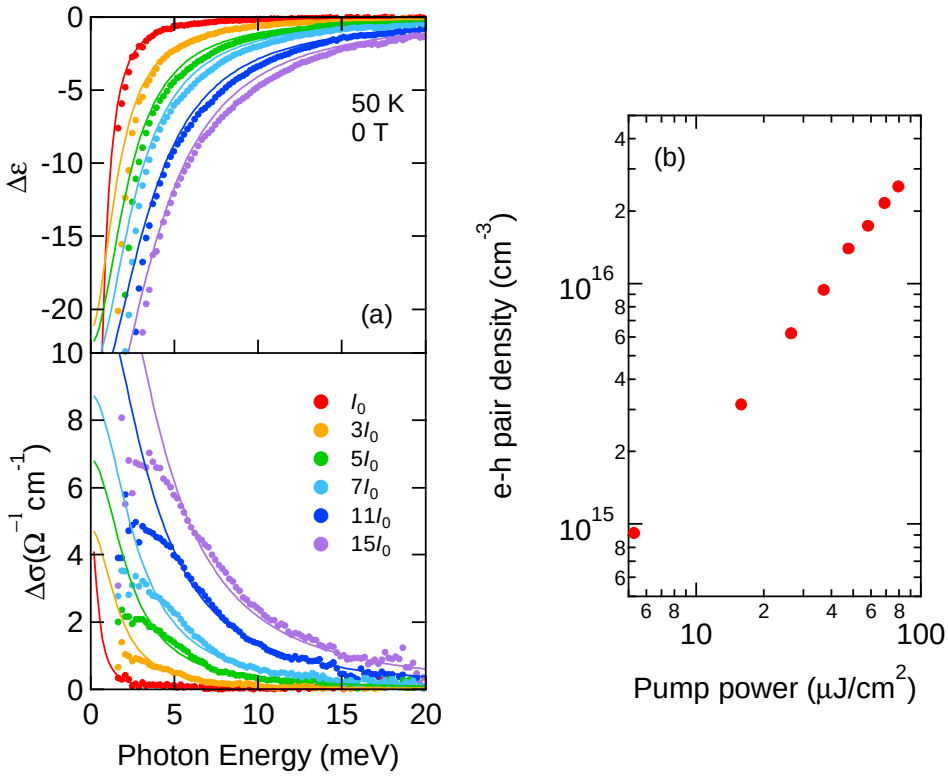

Figure 6.1: (a) Complex dielectric function at 50 K under zero magnetic field. $I_0 = 5.3\ \mu$J/cm^2. (b) The e-h pair density evaluated from the Drude fits as a function of the pump power.

6.3 Intra-exciton transition and suppression of EHD at low temperature under the uniaxial stress

Next, we measured the temperature dependence under zero magnetic field. Figures 6.2(a) and (b) show the temperature dependence of the dielectric function and the optical conductivity spectra. At high temperature, the spectra show the Drude response as we discussed in the previous Section. With the decrease of the temperature, two peak structures appear at 2.1 and 2.7 meV. These peaks can be assigned to the $1S$ - $2P_{\pm}$ and $1S$ - $3P_{\pm}$ transitions of the excitons.

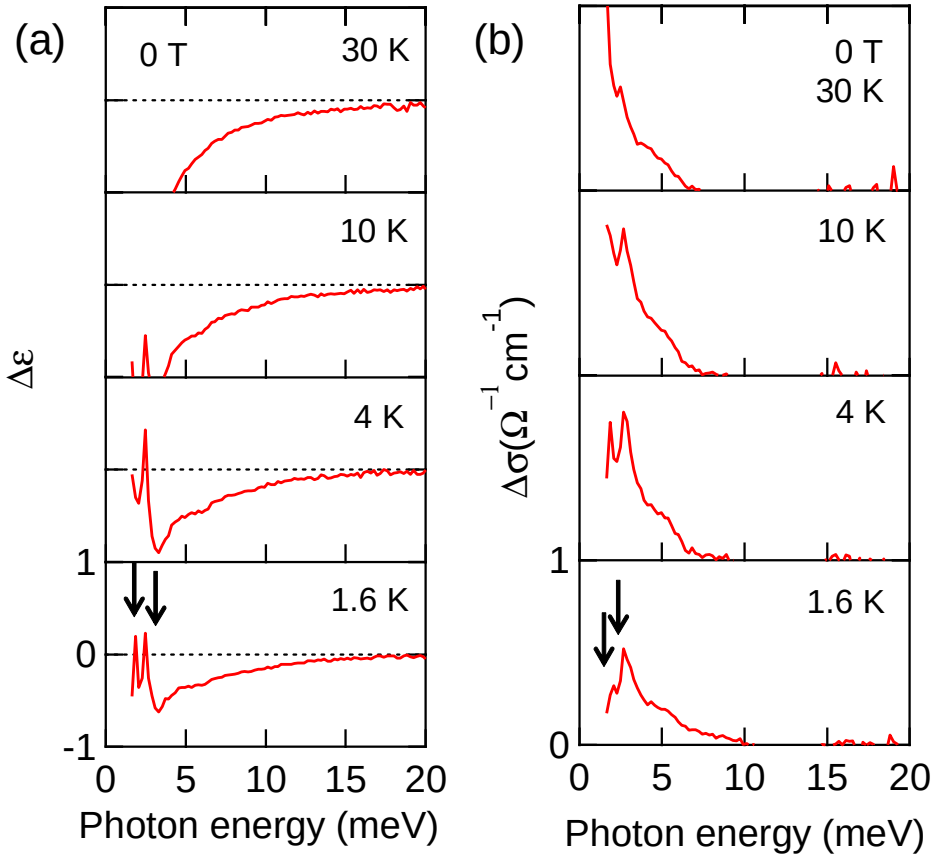

Figure 6.2: Temperature dependence of (a) the dielectric function and (b) the optical conductivity of photoexcited e-h system in uniaxially stressed Ge under zero magnetic field. The pump power was 5.3 μJ/cm^2 and the delay time between the optical pump and THz probe was fixed at 5 ns.

Under the ambient pressure, SPR frequency of EHD in Ge exists at 9 meV with the density of 2×10^{17} cm^{-3} [23]. Figures 6.3(a) and (b) show the dielectric function and the optical conductivity spectra of unstressed and uniaxially-stressed

Ge, respectively. The pump power was 16 μJ/cm^2. The solid lines in Fig. 6.3(a) represent the calculation result of EMT with the carrier density inside EHD 1.3 $\times$ 10^{17} cm^{-3}. From the agreement between the experiment and calculation in Fig. 6.3(a), The existence of EHD can be confirmed. In contrast, under the uniaxial stress, we could not obtain the theoretical curve with EMT which reproduces the experimental result. The solid lines in Fig. 6.3(b) represent the Drude-Lorentz fit with the Lorentzian peaks of 2.0 and 2.7 meV. Two peaks are attributed to the $1S$ - $2P_{\pm}$, and $1S$ - $3P_{\pm}$ transitions of the excitons. A broad structure is due to the Drude response of the free carriers. The transition to continuum may be included at high-energy side of intra-exciton transition in the experimental result. From this result, EHD can be regarded as completely suppressed by the uniaxial stress.

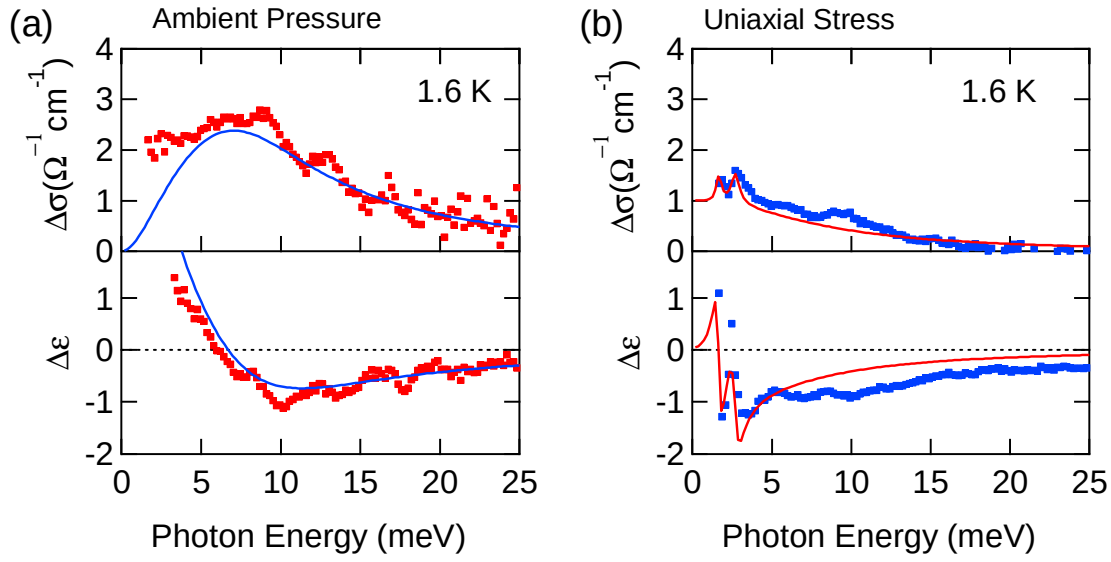

Figure 6.3: The dielectric function and the optical conductivity spectra of (a) unstressed and (b) uniaxially-stressed Ge. The pump power was 16 μJ/cm^2. Solid lines in (a) represent theoretical curves obtained by effective medium theory and solid lines in (b) represent the Drude-Lorentz fit.

6.4 Cyclotron resonance of free carriers under the uniaxial stress

Figures 6.4(a) and (b) show the magnetic field dependence of the change of the dielectric function and the optical conductivity spectra. The excitation power was 5.3 μJ/cm^2, and the delay time between the optical pump pulse and the THz probe pulse was 5 ns and the temperature was 50 K. At first, under zero magnetic field, the

spectrum is well described by the Drude model as shown in Fig. 6.1. It is attributed to the photoexcited free carriers. With the increase of the magnetic field, a sharp resonance appears above 2 T and shifts to high-energy side which is labeled C_e. Likewise, above 4 T, another broad resonance C_{h1} also appears. Above 5 T, one can identified another small peak appears at low-energy side of C_{h1}, which we denote C_{h2}. The energy shift of the resonances C_e, C_{h1}, and C_{h2} are plotted in Fig.6.4(c) as a function of the magnetic field. C_e shows the slope of 1.39 meV/T. From the slope, the effective mass can be determined by the relation $\omega_c = eB/m^*$. Then the resonance C_e is identified to the cyclotron of the electrons with the effective mass of 0.08 m_0. Besides, the slopes of C_{h1} and C_{h2} are 0.63 and 0.45 meV/T. From the slopes, we evaluate the cyclotron masses of 0.18 and 0.26 m_0, respectively. The C_h peaks are composed of two resonances, C_{h1} and C_{h2} as identified above 5 T.

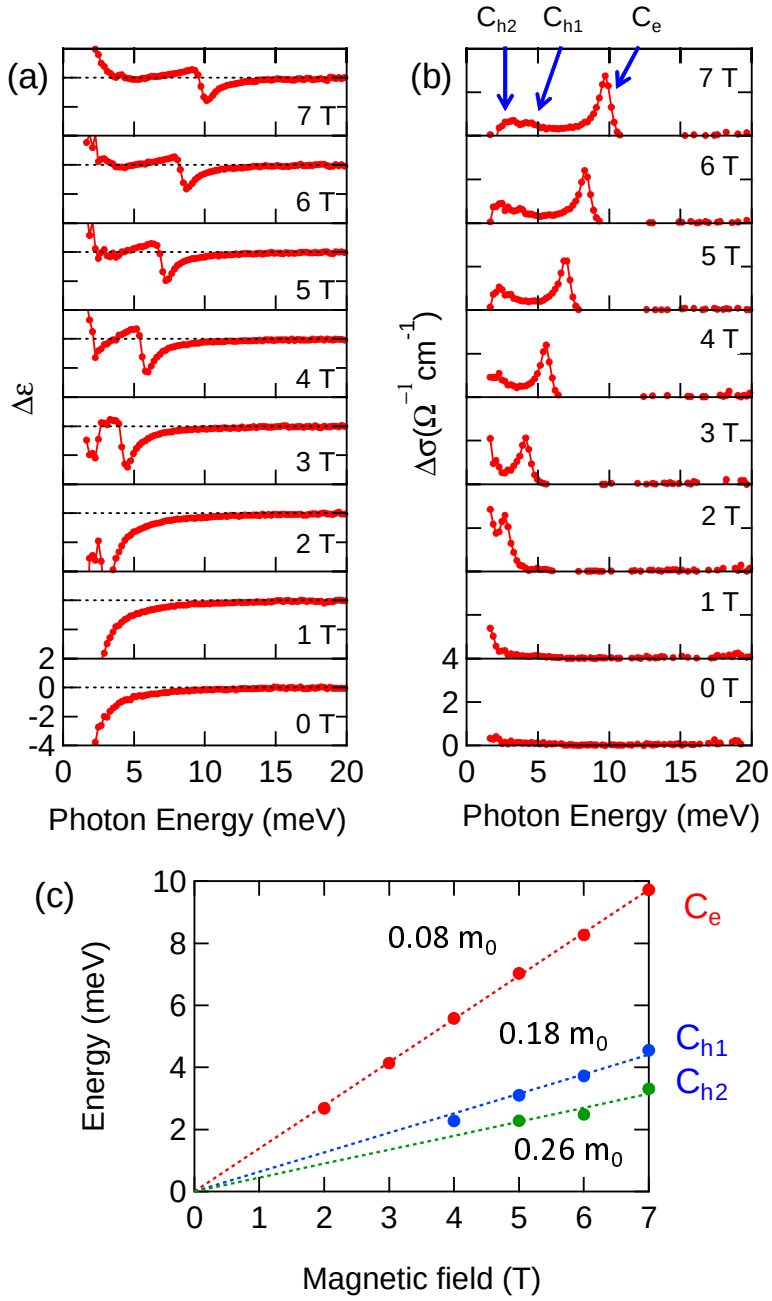

Figure 6.4: Photo-induced change of (a) the dielectric function and (b) the optical conductivity of photoexcited e-h system in uniaxially stressed Ge under the magnetic field at 50 K. The excitation power was 5.3 μJ/cm^2 and the delay time between the optical pump and THz probe was fixed at 5 ns. (c) The peak energies of cyclotron resonances C_e, C_{h1} and C_{h2} as a function of the magnetic field.

From the dielectric function, we can determine the frequency of the cyclotron resonance. To further confirm the origin of the cyclotron resonances, we measured

the Faraday rotation angle and the ellipticity. From eqs. 3.13 and 3.15, the sign of the ellipticity is determined by the phase difference between the x and y components of the transmitted THz electric field, indicating that the sign of the ellipticity is opposite between the electrons and the holes. Figures 6.5(a) and (b) show the Faraday rotation angle and the ellipticity spectra at 30 K and under 7 T, respectively. We fitted the spectra by Lorentzian functions as shown by blue solid lines in Fig. 6.5. The fitting parameters were $\hbar\omega_c$ and γ. The value $\hbar\omega_c$= 9.8 meV for C_e, 4.5 meV for C_{h1}, and 3.1 meV for C_{h2}. The value γ= 0.4 meV for C_e, 1.2 meV for C_{h1} and for C_{h2}. In Fig. 6.5(b), it can be seen that the sign of the ellipticity is opposite between the C_e and C_{hi} (i=1,2). Correspondingly, the dispersion of the Faraday rotation angle is also opposite (Fig. 6.5(a)). From the sign of the ellipticity, we can determine the kind of the carriers. Then, the peaks C_{h1} and C_{h2} are assigned to the cyclotron resonance of the holes and C_e to the electron. The peak C_{h1} is attributed to the hole of the $|J_z| = 3/2$ valence band, correspondingly C_{h2} is that of the $|J_z| = 1/2$ valence band.

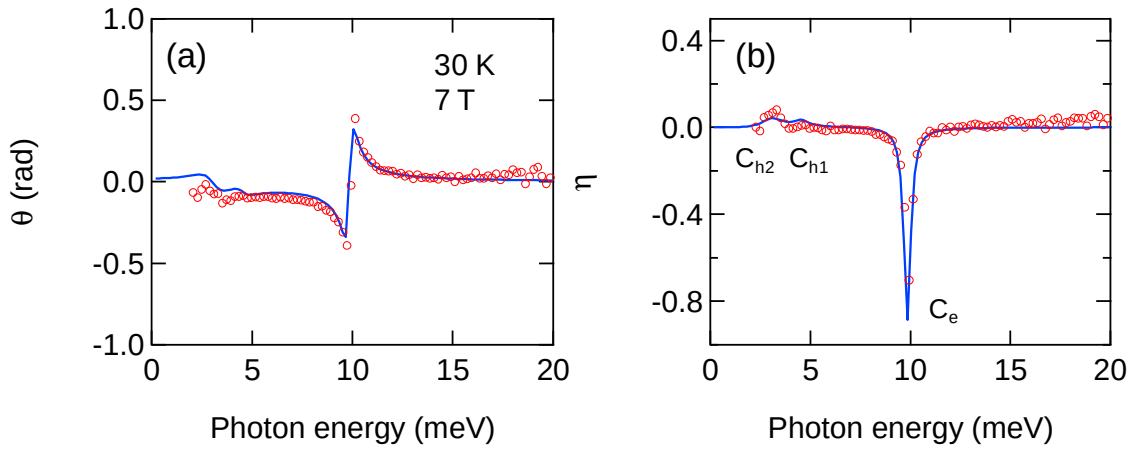

Figure 6.5: (a) The Faraday rotation angle and (b) the ellipticity spectra at 30 K and under 7 T. Blue solid lines are fitting curves by Lorentzian function.

6.5 Magnetoexcitons in the low density regime

6.5.1 Magnetic field dependence

Next, we studied the magnetic field dependence of the photoexcited e-h system at low temperature below the binding energy of the excitons. Figure 6.6 shows the change of (a) the dielectric function and (b) the optical conductivity spectra at low temperature of 1.6 K and in the low exciton density of 5.3 μJ/cm^2. The delay time of THz probe pulse to the optical pump pulse was 5 ns. At zero magnetic field, two peak structures are identified at 2.1 meV and 2.7 meV, which corresponds to

the transition of $1S$ to $2P_{\pm}$ and $3P_{\pm}$ excitons as described in Section 6.2. With the increase of the magnetic field, two new peaks appear which are labeled FE_1 and FE_2, respectively, which is assigned to the magnetoexciton as we describe in detail later. The sharp line denoted C_e corresponds to the cyclotron resonance of electrons. The cyclotron resonance of holes is less prominent.

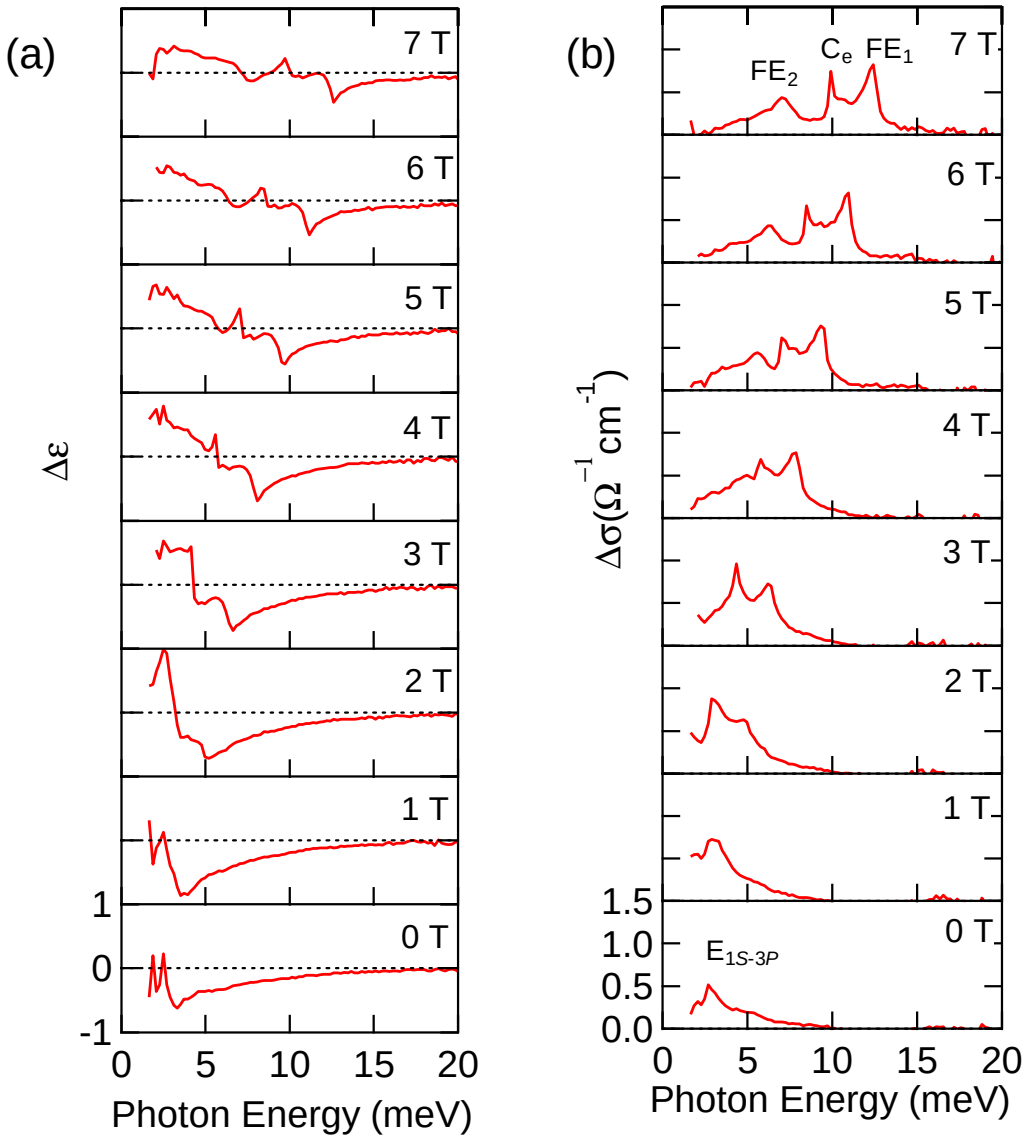

Figure 6.6: (a) Dielectric function and (b) optical conductivity spectra of photoexcited e-h system in uniaxially stressed Ge under the magnetic field at 1.6 K. The delay time between the optical pump and THz probe was fixed at 5 ns. C_e, C_{h1}, and C_{h2} indicate the cyclotron resonances of the electrons and the holes. FE_1 and FE_2 represent the intra-transition of magnetoexcitons.

Figure 6.7(a) shows the peak energies of FE_1, FE_2, and C_e as a function of the magnetic field. Here, for a reference, we added the data of C_{h1} taken at 50 K, since it is not clearly identified at 1.6 K (Fig. 6.6). In Fig. 6.7(a), one can see that the peak energies of FE_1 and FE_2 are parallel to the that of C_e and C_{h1}, respectively. Indeed, from the fitting by the linear function, the slopes of FE_1 and FE_2 are in good agreement with that of C_e and C_{h1}. The magnetic field effect which is shown in Fig. 6.7(a) is consistent with the previous report by using magnetoabsoption measurement [32].

The magnetic field effect of the peak energies of FE_1 and FE_2 are can reproduced by eq. 2.41, which is presented again as,

$$E^{NM\lambda} = \frac{e\hbar H}{c}\left[\frac{1}{\mu_t}\left(N+\frac{1}{2}\right) - \frac{1}{m_{ht}}M\right] + E_c^{NM\lambda}\ , \tag{6.1}$$

with the binding energy $E_c^{NM\lambda}$=2.2 meV. Therefore, we can conclude that the FE_1 and FE_2 are assigned to the Landau level transitions of the electrons and the holes with the Coulombic interaction, i. e. the intra-transition of the magnetoexcitons.

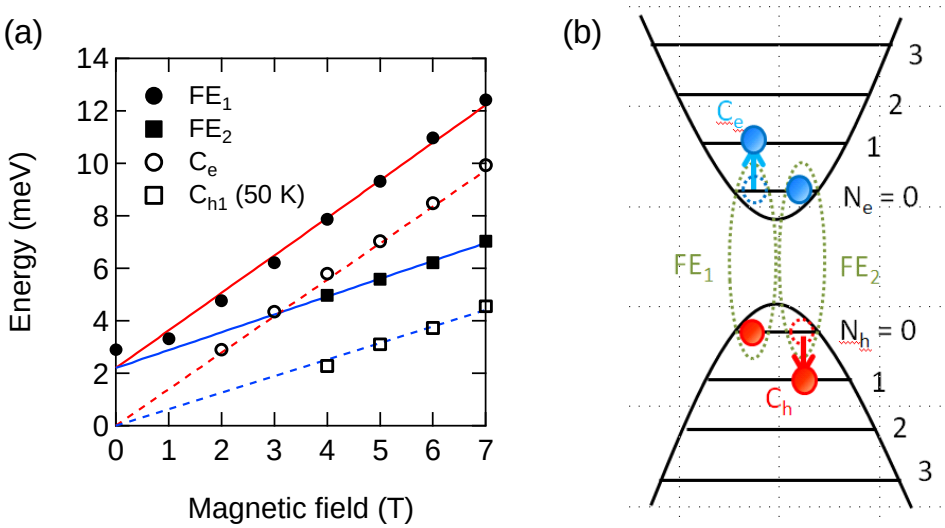

Figure 6.7: (a) Peak energies of cyclotron resonances (C_e and C_{h1}) and magnetoexcitons (FE_1 and FE_2) as a function of the magnetic field. Markers plot the experimental result and solid lines are calculated by eq.2.41. data of C_{h1} taken at 50 K is added for a reference. (b) The schematic of intra-transition of the magnetoexcitons and the cyclotron resonances of the free carriers.

6.5.2 Temperature dependence under the magnetic field

We investigated the temperature dependence of the intra-transition of the magnetoexcitons under 7 T. Figures 6.8(a) and (b) represent the temperature dependence of the dielectric function and the optical conductivity spectra under 7 T. The labels

FE_1, FE_2, C_e, C_{h1}, and C_{h2} are also shown for the indication. In Fig. 6.8(a) and (b), it is clearly seen that the FE_1 and FE_2 increase with the decrease of the temperature, whereas C_e, C_{h1}, and C_{h2} decrease. This behavior can be interpreted by the thermal stabilization of the magnetoexcitons.

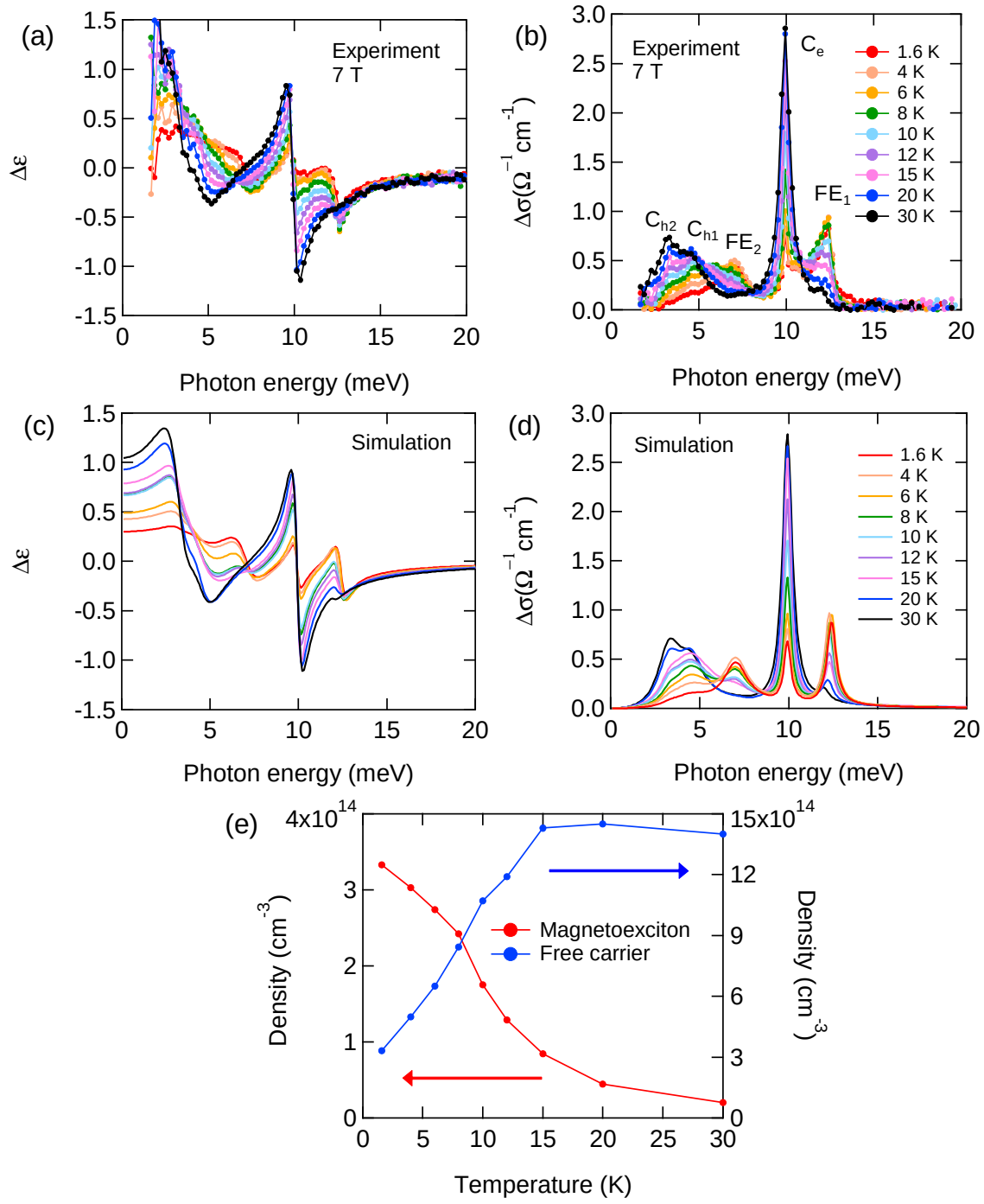

Figure 6.8: (a) The dielectric function and (b) the optical conductivity spectra under 7 T at different temperature. The pump power and the delay time were 5.3 μJ/cm^2 and 5 ns, respectively. (c),(d) The simulation of temperature dependence of the dielectric function and the optical conductivity spectra under 7 T by using five Lorentzian functions. (e) Evaluated densities of the magnetoexcitons and free carriers.

To evaluate the densities of the magnetoexcitons and free carriers quantitatively, we performed the simulation. Figures 6.8(c) and (d) show the simulation with five Lorentzian functions. In the case of the cyclotron resonances of the free carriers, the spectral features can be well reproduced by the Lorentzian functions. However, the spectral features of the magnetoexcitons are not in good agreement with the Lorentzian functions. The spectrum of the magnetoexcitons exhibits a tail to low-energy side, likely in the form of inverse-Boltzmann distribution. This behavior can be interpreted by the dispersion relation of $|NM\rangle = |00\rangle$ and $|10\rangle$ magnetoexcitons as we described in Chapter 2, section 2.3. Instead of quantitatively describing this asymmetric lineshapes of intra-transition of the magnetoexcitons, here we evaluated the density of the magnetoexcitons at 1.6 K in a different way. First, from the total spectral weight, we evaluated the total e-h pair density as 5.5×10^{14} cm^{-3}. Next, we evaluated the free carrier density by the Lorentzian fitting of the cyclotron resonances as 0.5×10^{14} cm^{-3}. From the difference of these density, we estimated the density of magnetoexcitons as 5.0×10^{14} cm^{-3}, which is indeed higher than the estimation obtained by approximating the intra-transitions of magnetoexcitons with the Lorentzians as shown in Fig. 6.8(e).

6.6 Evaluation of the temperature of magnetoexcitons

We estimated the temperature of the magnetoexcitons. Figures 6.9(a)-(c) show the absorption spectra at the lattice temperature of 6, 4, and 1.4 K under 7 T. The pump power and the delay time were 5.3 μJ/cm^2 and 5 ns, respectively. One can see that the widths of peaks C_e and FE_1 become sharp with the decrease of the temperature. With assumption of the Maxwell-Boltzmann distribution of $|00\rangle$ magnetoexciton, the spectral feature of the intra-magnetoexciton transition which is from $|00\rangle$ to $|10\rangle$ is given by [61]

$$\Delta\alpha \propto \int \sqrt{E - E_{01} - \epsilon}\, \exp\left(\frac{E - E_{01} - \epsilon}{(M_{00}/M_{10} - 1)k_B T}\right) \frac{\Gamma_{10}/2}{\epsilon^2 + (\Gamma_{10}/2)^2} d\epsilon \ . \qquad (6.2)$$

where E_{01} is the offset energy of $|00\rangle$ to $|10\rangle$ transition, M_{00} (M_{10}) is the mass of the magnetoexciton $|00\rangle$ ($|10\rangle$), and Γ_{10} is the damping constant of $|10\rangle$ magnetoexcitons. We reproduced the spectral feature of the FE_1 by eq. 6.2. To evaluate the slope of the FE_1 accurately, we added two Lorentzian peaks in Figs. 6.9(a)-(c). The black solid lines Figs. 6.9(a)-(c) show the fitted curves and the black dotted lines represent the FE_1 components which is calculated by eq. 6.2 with assuming that the masses of $|00\rangle$ and $|10\rangle$ magnetoexcitons correspond to the 2 dimensional case i. e. $M_{10} = -2M_{00}$ [34, 35]. Evaluated temperature of the magnetoexciton T_{ex} is shown in Fig. 6.9(d) as a function of the lattice temperature T_L. At the lattice temperatures of 6 and 4 K, the temperature of the magnetoexcitons was evaluated as equal to the lattice temperature. However, at the lattice temperature of 1.4 K, the temperature of the magnetoexcitons was evaluated as 2.3 K which is slightly higher than the lattice temperature. Since the pump photon energy of 0.86 eV is

larger than the exciton energy of 0.74 eV, the temperature difference of the excitons and the lattice would be due to the heating by the excess energy of the optical pump pulse. By setting the delay time larger than 5 ns, we expect that the excitons reach the thermal equilibrium with the lattice. There is a possibility that the temperature cools down lower than 2.3 K when the delay time is set longer than 5 ns.

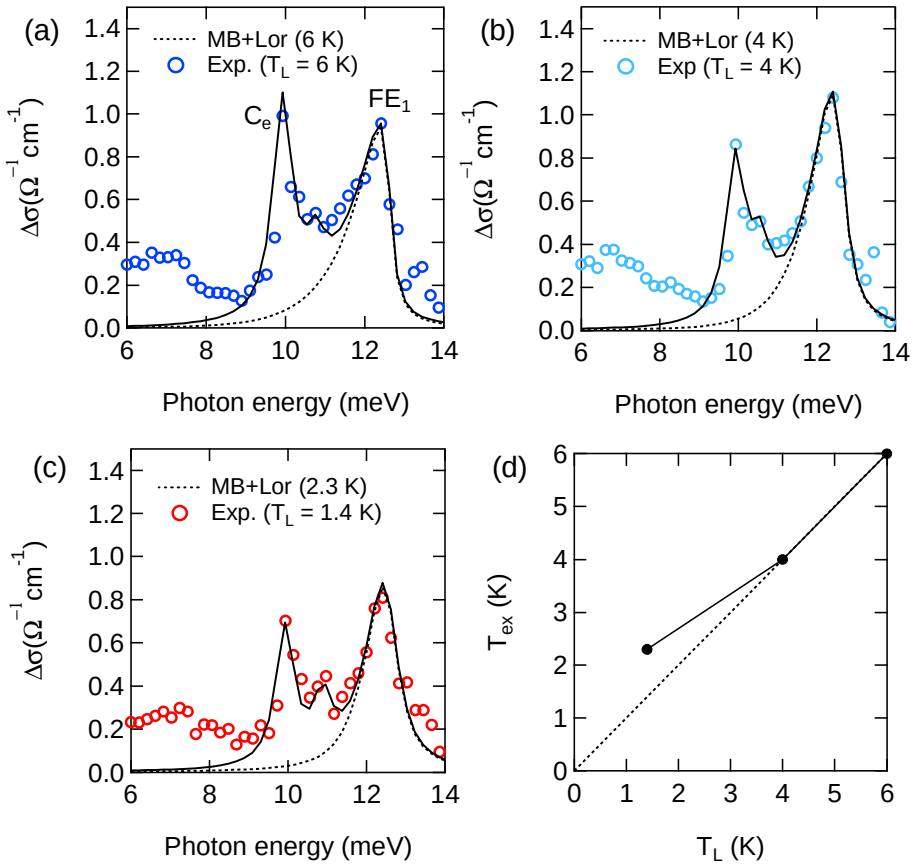

Figure 6.9: Temperature dependence of the optical conductivity spectra of photoexcited e-h system in uniaxially stressed Ge under 7 T at (a) 6, (b) 4, and (c) 1.4 K. The pump power and the delay time were 5.3 μJ/cm^2 and 5 ns, respectively. Black dotted lines represent the FE_1 components which is calculated by eq. 6.2. Black solid lines represent the fits which included the C_e component. (d) The temperature of the magnetoexciton T_{ex} as a function of the lattice temperature T_L.

6.7 Formation dynamics of the magnetoexcitons

We studied the formation dynamics of the magnetoexcitons. Figures 6.10(a) and (b) represent the temporal dynamics of the dielectric function and the optical conductivity after the photoexcitation under 7 T. The pump power was 16 μJ/cm^2.

At 10 ps, the cyclotron resonances of free carriers C_e, C_{h1}, and C_{h2} are observed. This spectrum is analogous to the spectrum at high temperature, indicating that the initial state of photoexcited e-h system is heated by photoexcitation. After 1 ns, the intra-transitions of the magnetoexcitons FE_1 and FE_2 appear, indicating that the formation of the magnetoexcitons takes a long period of $\sim$ 1 ns, which presumably indicates the cooling dynamics of photoexcited e-h system in Ge. The spectral weight of the magnetoexcitons FE_1 and FE_2 increases with temporal evolution to 2 ns, and after 2 ns, the spectral shape becomes time-independent. Therefore, at 5 ns after the photoexcitation, the system can be regarded as in the quasi-equilibrium state.

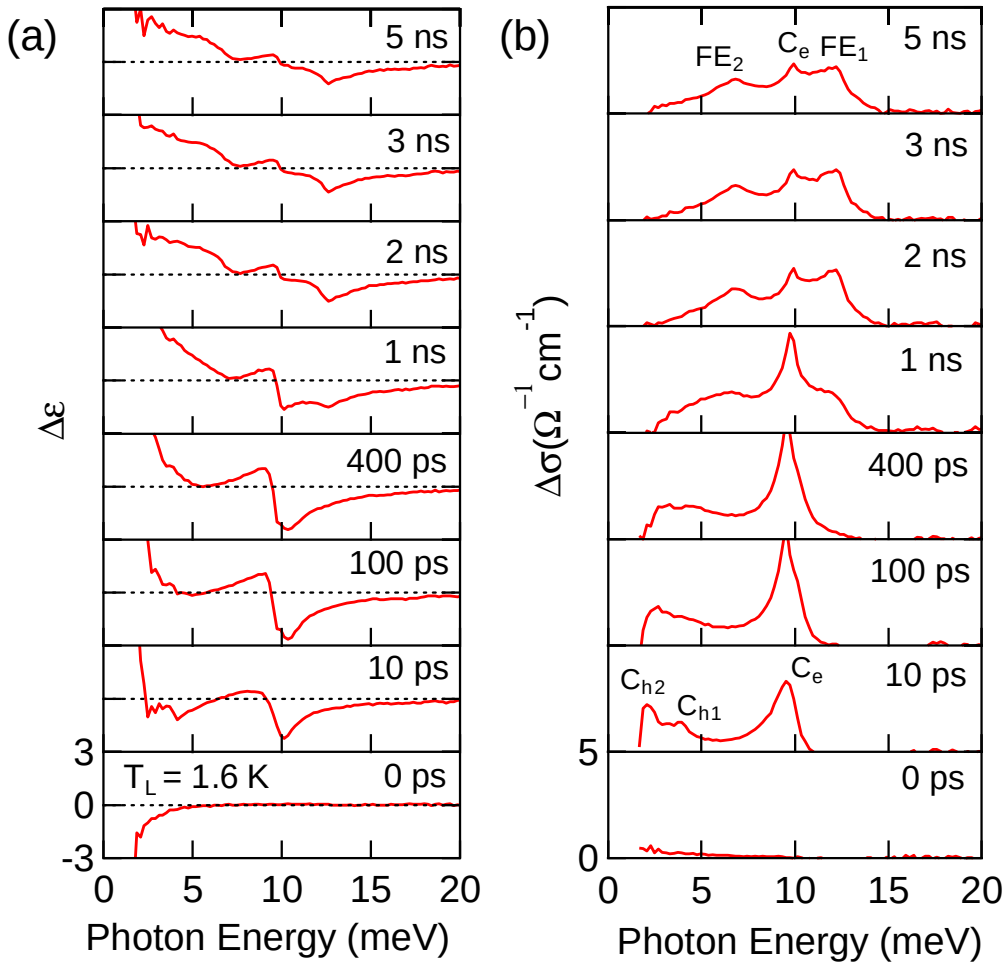

Figure 6.10: Temporal evaluation of (a) the dielectric function and (b) the optical conductivity spectra of photoexcited e-h system in uniaxially stressed Ge at 1.6 K under 7 T. The pump power was 16 μJ/cm^2. C_e indicates the cyclotron resonance of the electron. FE_1 and FE_2 represent the intra-transition of magnetoexcitons.

As discussed in Section 6.4, we can determine the kind of the free carrier by measuring the Faraday rotation angle and the ellipticity. To investigate the formation dynamics in more detail, we measured the temporal evolution of the Faraday rotation angle and the ellipticity. Figure 6.11(a) and (b) show the temporal evolution of the Faraday rotation angle and the ellipticity spectra at 5 K under 7 T. The cyclotron resonances of the free electrons and free holes are clearly identified with opposite sign of the ellipticity at fast temporal region. At 5 ns after the photoexcitation, the opposite dispersions of FE_1 and FE_2 can be seen in Figs. 6.11(a) and (b).

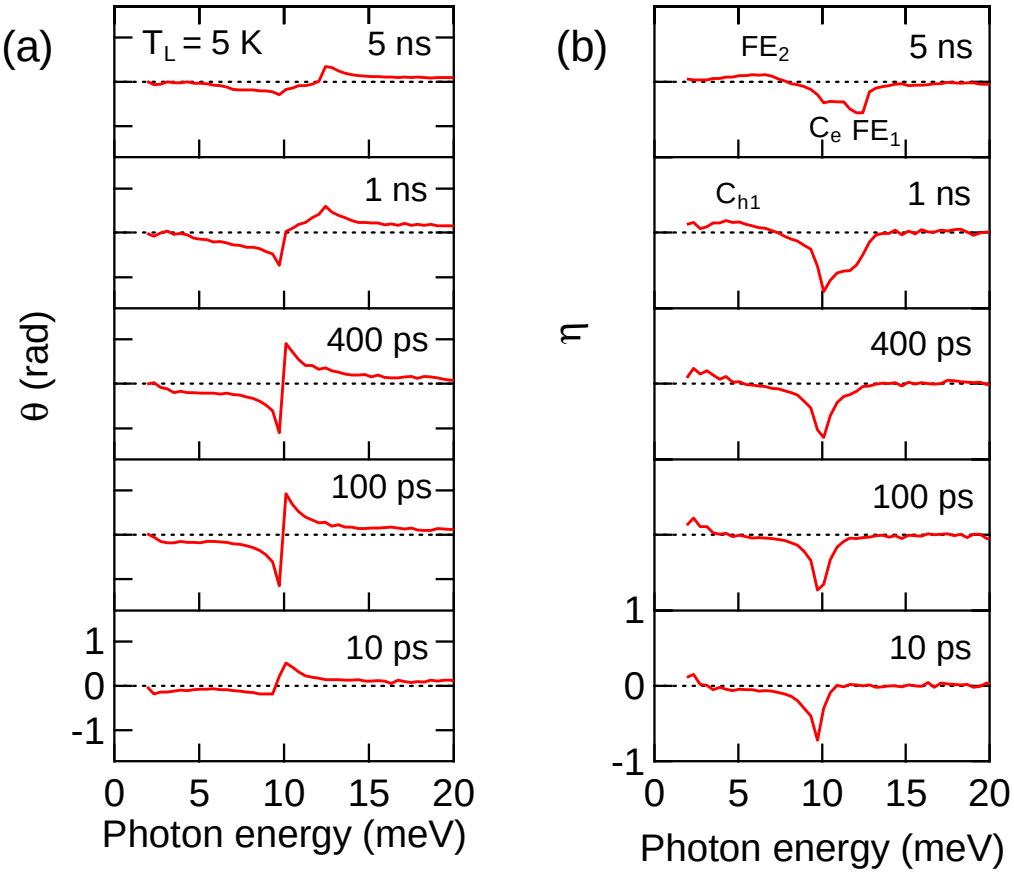

Figure 6.11: Temporal evaluation of (a) the Faraday rotation angle and (b) the ellipticity spectra of photoexcited e-h system in uniaxially stressed Ge under the magnetic field at 5 K under 7 T. The pump power was 16 μJ/cm^2. C_e indicates the cyclotron resonance of the electron. FE_1 and FE_2 represent the intra-transition of magnetoexcitons.

6.8 Magnetoexcitons in high density regime

6.8.1 Invalidity of the OPTP spectroscopy under the magnetic field

In this study, we investigated the response of the e-h systems in Si and Ge by using the differential transmission spectra. Here, we remind the detection of THz probe pulse. The detection efficiency of the THz wave of EO sampling method depends on the polarization of the THz wave (the detailed information is presented in Chapter 3). Therefore, we optimize the angle of the detection GaP crystal with polarization of probe THz wave and gate pulse. Due to the polarization dependence of EO sample method, exactly, we obtain the differential transmission of x-polarized THz wave component $|E_x^{\rm pump}|^2/|E_x^{\rm nopump}|^2$, where $E_x^{\rm pump}$ and $E_x^{\rm nopump}$ denotes the x component of THz electric field with and without the optical pump. Here, we call the direction of the optimized polarization of the THz wave as x. Since the generated THz wave is purely x-polarized, when the optical pump switched off, $|E_x^{\rm nopump}|^2$ is same to the power of the THz probe pulse. Also, in the case of the observation of the free carriers under zero magnetic field or charge neutral object such as exciton, the THz probe pulse of $E_x^{\rm pump}$ is kept x-polarization. Therefore, in such case, the differential transmission spectra indicate the absorption directly. However, for the observation of the cyclotron resonance, it must be paid attention. In the case of the cyclotron resonances of the free carriers, they absorb either the right- or left-handed circular polarization. Therefore, the polarization of the transmitted THz pulse is rotated and be ellipsoidal by the Faraday effect. As a result, in the high density region of free carriers under the magnetic field, the differential transmission spectra cannot be directly related to the absorption. Since the intra-transition of the magnetoexcitons is also originated by the cyclotron resonance, the same invalidity occurs.

For example, Fig. 6.12(a) shows the excitation power dependence of the differential transmission spectra $|E_x^{\rm pump}|^2/|E_x^{\rm nopump}|^2$ at 30 K under 7 T. In Fig. 6.12(a), the peak of the cyclotron resonance of the electrons "seems" to shift to low-energy side with the increase of the excitation power. However, it is just attributed to the rotation and ellipsoidal deformation of the THz probe pulse. Indeed, the ellipticity spectra show different behavior as shown in Fig. 6.12(b). There is no peak shift. Therefore, to obtain the correct absorption spectra, we must measure the x- and y-component of the THz probe pulse simultaneously. For this reason, we measured the Faraday rotation angle and the ellipticity for the excitation power dependence under the magnetic field.

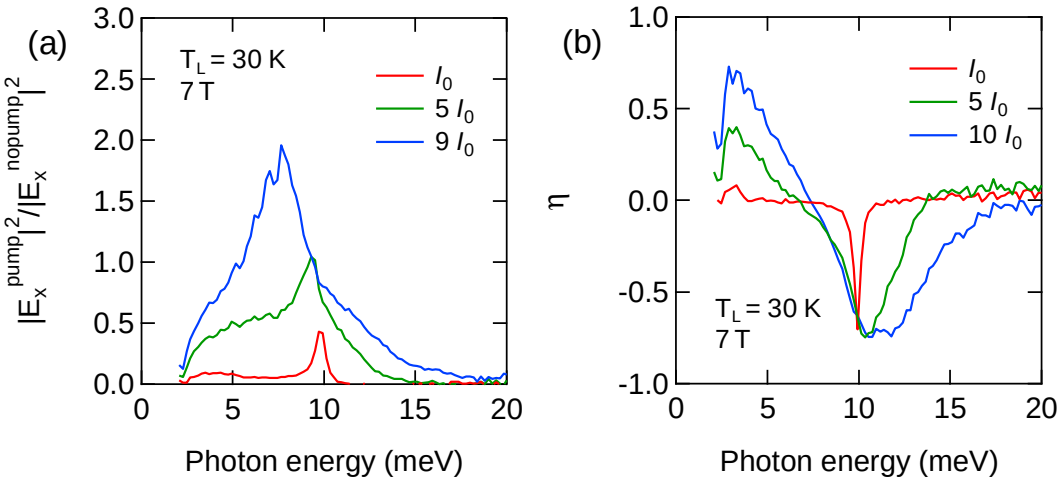

Figure 6.12: (a) The differential transmission of x-polarized THz wave component $|E_x^{\rm pump}|^2/|E_x^{\rm nopump}|^2$. (b) The ellipticity spectra under same condition with (a).

6.8.2 Excitation power dependence

To realize lower temperature than 1.6 K, we introduced the mechanical booster pump system described in Chapter 3. By the enhancement of the exhaust velocity, the temperature below 1.20 K was realized. However, due to the Joule heating of the magnet coils, the temperature increases slightly under the magnetic field. Under the 7 T, the realized temperature was 1.27 K. The delay time was fixed at 5 ns. The lowest excitation power I_0 was 5.3 μJ/cm^2. Furthermore, to prevent thermal heating by the excess energy of the optical pump, we used long-wavelength optical pulse of 1500 nm as the optical pump. Figures 6.13(a) and (b) show the Faraday rotation spectra and the ellipticity spectra under 7 T at 1.27 K. For the Faraday rotation, we plotted from -$\pi/2$ to $\pi/2$. At the low density, the C_e (9.92 meV) and the FE_1 (12.4 meV) can be seen clearly. Also, the hole-like structure appears around 7 meV with broad width. This is attributed to C_{h1} and FE_2 as discussed previously. The jumps of the Faraday rotation angle at high density region are due to the rotation angle larger than $\pi/2$. With the increase of the pump power, one can see that the population in η spectra of the magnetoexcitons is increases significantly whereas the intensity of the cyclotron resonance is almost conserved up to the pump power of 5 I_0. In higher density region, the ellipticity spectra broaden asymmetrically.

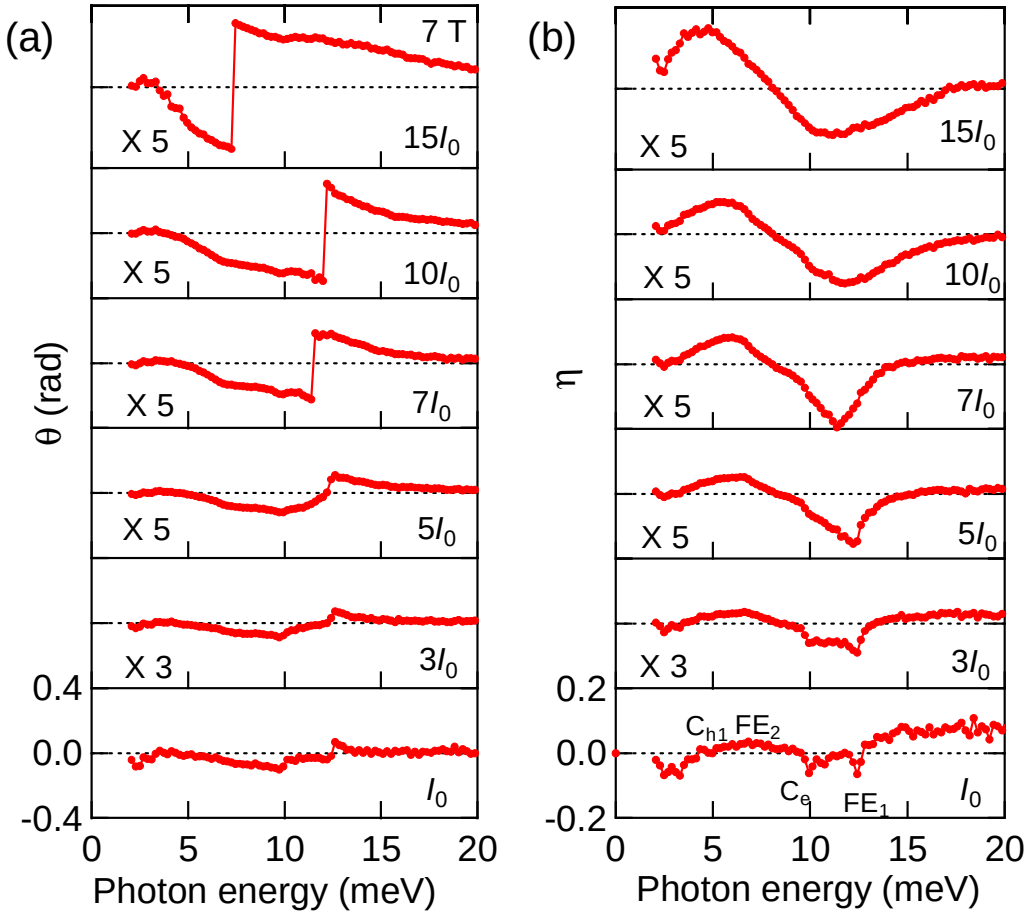

Figure 6.13: (a) The Faraday rotation angle spectra and (b) the ellipticity spectra under 7 T at 1.27 K. The delay time was fixed at 5 ns and the lowest pump power I_0 was 5.3 μJ/cm^2.

To confirm the origin of the broad spectral weight in high density region, we investigate the pump power dependence at high temperature. Figure 6.14 shows the ellipticity spectra under 7 T at (a) 1.27 K, (b) 5 K, and (c) 30 K. The similar pump power dependence between 1.27 K and 5 K can be seen for all regions. Note that the excitonic FE_1 structure is clearly seen up to 5 I_0. Above 7 I_0, FE_1 structure broadens and a long tail toward high-energy side appears. On the other side, the excitonic FE_2 structure clearly remains to 10 I_0. Since 5 K is higher than the critical temperature of EHD in stressed-Ge, 4 K [30], the spectral similarity between 1.27 K and 5 K indicates that the EHD was not formed.

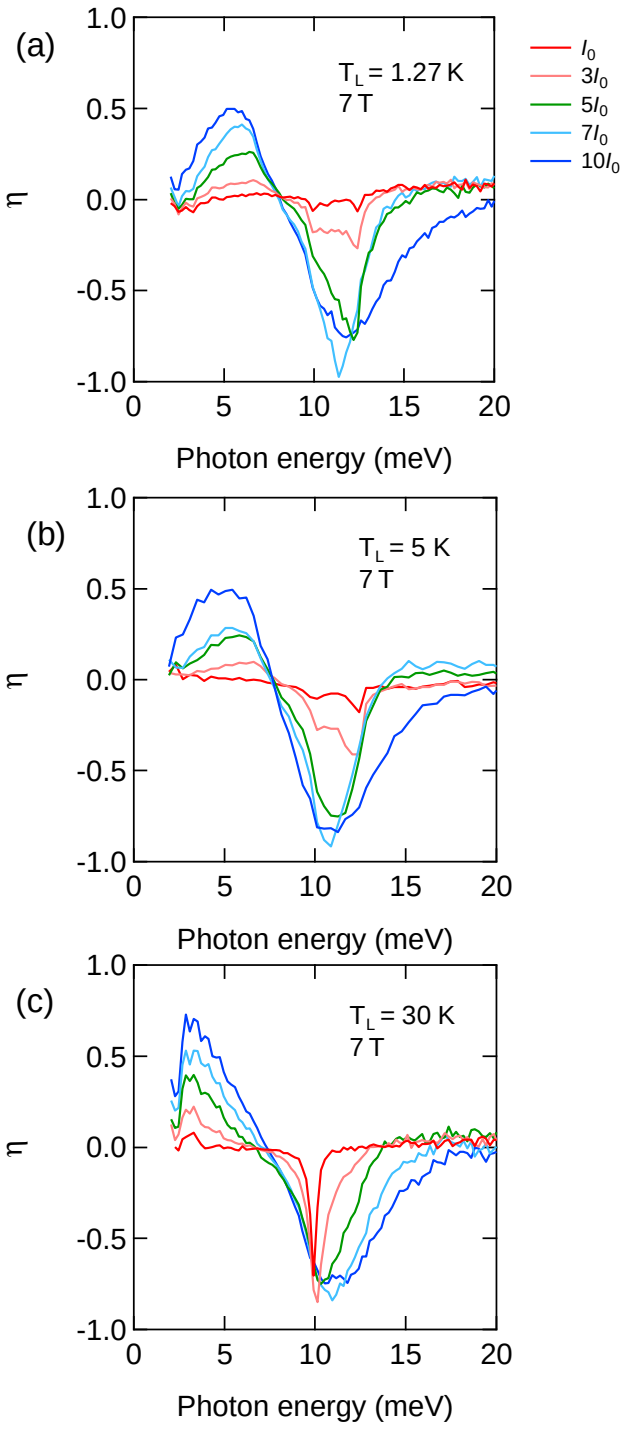

Figure 6.14: The ellipticity spectra under 7 T at the lattice temperature of (a) 1.27 K, (b) 5 K, and (c) 30 K. The delay time was fixed at 5 ns and the lowest pump power I_0 was 5.3 μJ/cm^2.

To evaluate the density of the magnetoexcitons quantitatively, we extracted the off-diagonal component ϵ_{xy} from the Faraday rotation angle and the ellipticity. When the difference of the refractive index and the absorption between the right-handed- and left-handed-circular polarizations is small, The Faraday rotation angle and the ellipticity is given by [62]

$$\theta = -\frac{\omega}{2c}\frac{\kappa\epsilon_{xy}^{'} - n\epsilon_{xy}^{''}}{n^2+\kappa^2}d$$
$$\eta = -\frac{\omega}{2c}\frac{n\epsilon_{xy}^{'} + \kappa\epsilon_{xy}^{''}}{n^2+\kappa^2}d \ , \tag{6.3}$$

where $\tilde{N} = n + i\kappa$ is the complex refractive index, $\epsilon_{xy} = \epsilon_{xy}^{'} + i\epsilon_{xy}^{''}$ is the off-diagonal component of the dielectric function, c is the speed of light, and d is the thickness of the sample. By using eqs. 6.3, we can determine the ϵ_{xy} from the measured Faraday rotation angle and ellipticity. Figures 6.15(a) and (b) represent the determined real and imaginary part of ϵ_{xy}, respectively. From the Im[ϵ_{xy}] spectra, one can see that the dispersion of the C_e does not increase in all excitation regime. Therefore, we can conclude that most of photoexcited e-h pairs forms the magnetoexciton in this condition.

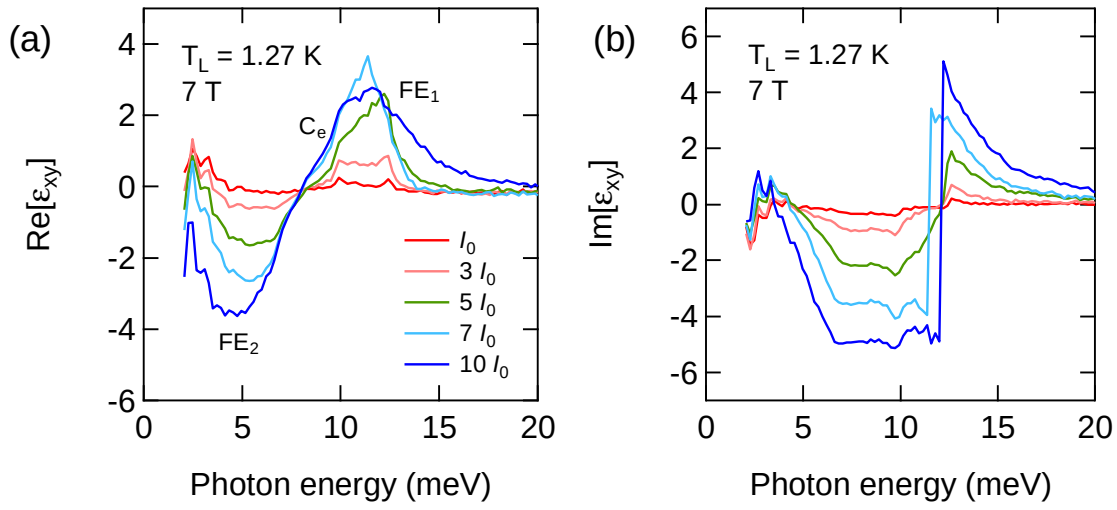

Figure 6.15: (a) The real part and (b) the imaginary part of ϵ_{xy} which is determined from the Faraday rotation angle and ellipticity spectra (Fig. 6.13).

The sum rule for the real part of ϵ_{xy} is given by [63]

$$N = \frac{2\epsilon_0 m^2}{\pi e^3 B_0}\int_0^\infty \omega^2 \epsilon_{xy}^{'} d\omega \ . \tag{6.4}$$

Firstly, by using eq. 6.4, we evaluated the total e-h pair density in the excitation range between I_0 to 10 I_0. Here, we used the optical reduced mass of the free carriers and the excitons 0.046 m_0 [21]. Next, we evaluated the density of free carriers from the cyclotron resonance. In the case of the cyclotron resonance, the off-diagonal component of the dielectric function is given by [62]

$$\epsilon_{xy} = \omega_p^2 \frac{i\omega\omega_c}{(\omega^2 + i\omega\gamma)^2 - \omega^2\omega_c^2} \ , \tag{6.5}$$

where $\omega_c = eB_0/m^*$ is the frequency of the cyclotron resonance of the free carrier with effective mass of m^*. By using eq. 6.5, we fitted the ϵ_{xy} spectra as shown by blue lines in Fig. 6.16. Since the spectrum of low-energy side is broadened, the separation of spectrum is difficult. Therefore, we focused on the component C_e. The damping constant γ and the density of the free carrier N_c were used as fitting parameter. By Lorentzian fit of the peak C_e, the density of the electrons is evaluated to 0.6×10^{14} cm^{-3}. The FE_1 was also included to reproduce the ϵ_{xy} spectra. However, since the spectral feature of FE_1 is not Lorentzian, we evaluate the density of the magnetoexcitons from the difference of the density of the free carriers to that of total e-h pairs.

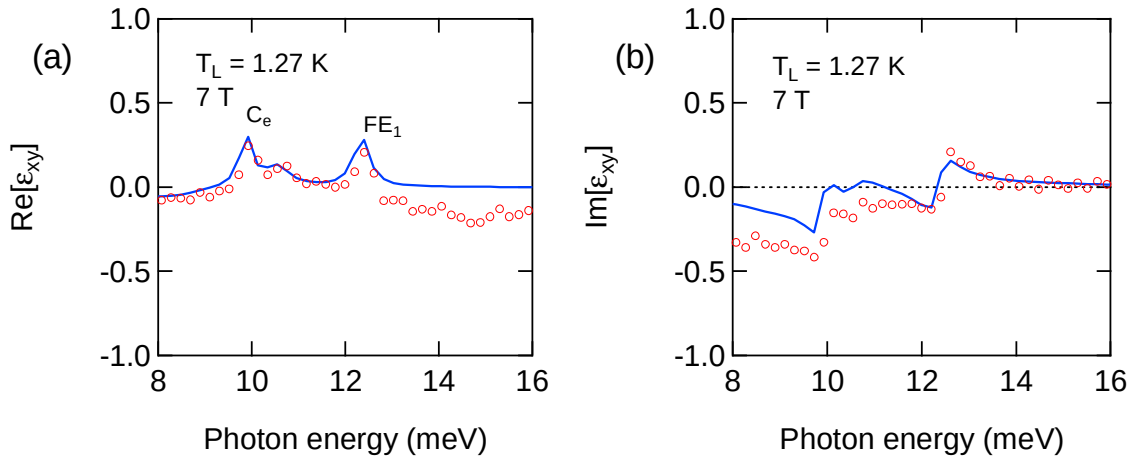

Figure 6.16: (a) The real part and (b) the imaginary part of ϵ_{xy} under 7 T. The delay time was fixed at 5 ns and the pump power was 5.3 μJ/cm^2. Blue solid lines are the multi Lorentzian fits by using eq. 6.5.

For the high density spectra, the identification by multi-Lorentzian fit is difficult due to the spectral broadening. Therefore, we evaluate the density of the free carriers from the height scaling of the peak C_e in imaginary part of ϵ_{xy} spectra due to the dispersion of C_e can be evaluated clearly in imaginary part of ϵ_{xy}. Figure 6.17(a) shows again the imaginary part of ϵ_{xy} under 7 T. The heights of the C_e are shown by the arrows at each pump power. Figure 6.17(b) shows the densities of the total e-h

pairs (black line), the free carriers (blue line), and the magnetoexcitons (red line). The density of the magnetoexciton is the different from the density of the total e-h pairs to that of the free carriers.

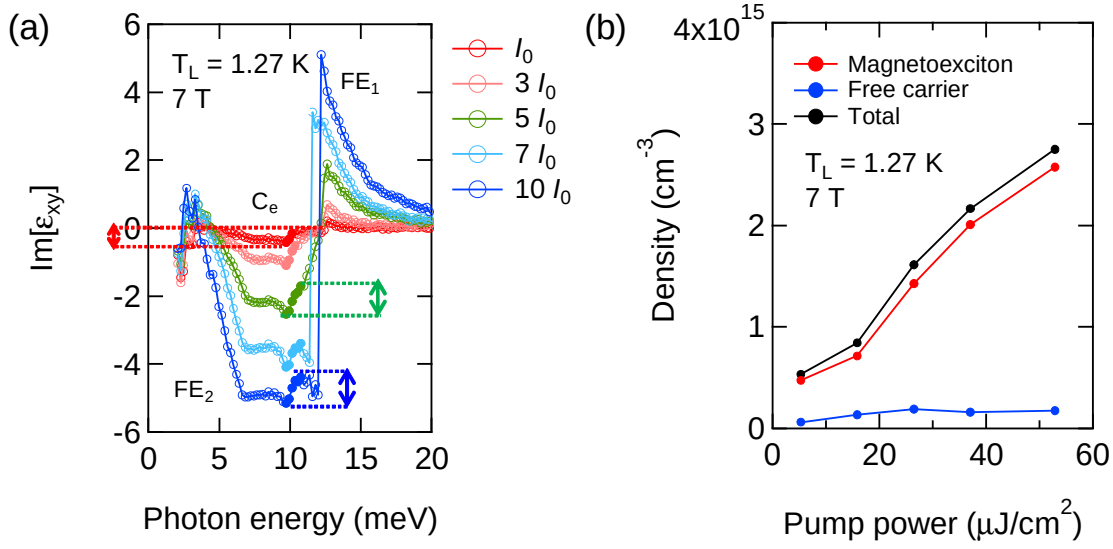

Figure 6.17: (a) The imaginary part of ϵ_{xy} under 7 T of different pump power with $I_0 = 5.3\ \mu$J/cm^2. The closed circles represent the height of the C_e. (b) The densities of total e-h pairs (black), the free carriers (blue), and the magnetoexcitons (red) as a function of the pump power.

From Fig. 6.17(b), the accumulated density of the magnetoexcitons is evaluated as 2.6×10^{15} cm^{-3}. For this density, the critical temperature of BEC is estimated to 0.6 K with the mass of 0.90 m_0 at 7 T which is estimated from the increase of the in-plane mass $M_{00} = 2\hbar^2/E_0 l_B^2$ by the magnetic field [35]. Assuming that the temperature of the magnetoexciton is 2.3 K which is estimated at relatively low excitation density (Fig, 6.9), the density of 2.6×10^{15} cm^{-3} gives the phase space density of 0.14. In this study, the maximum density of magnetoexciton was limited by the output power of OPA which is used as the optical pump. Therefore, further increase of the density of the magnetoexciton is expected by improving the output power of OPA. When we consider the case of two dimensional system, the mass of the magnetoexciton increases with the magnetic field [35]. Since the spin degeneracy of the excitons can be lifted by applying the magnetic field above 3 T, we examined the density of magnetoexciton under 4 T. Figure 6.18 shows the excitation power dependence of the Faraday rotation spectra and the ellipticity spectra under 4 T at 1.27 K.

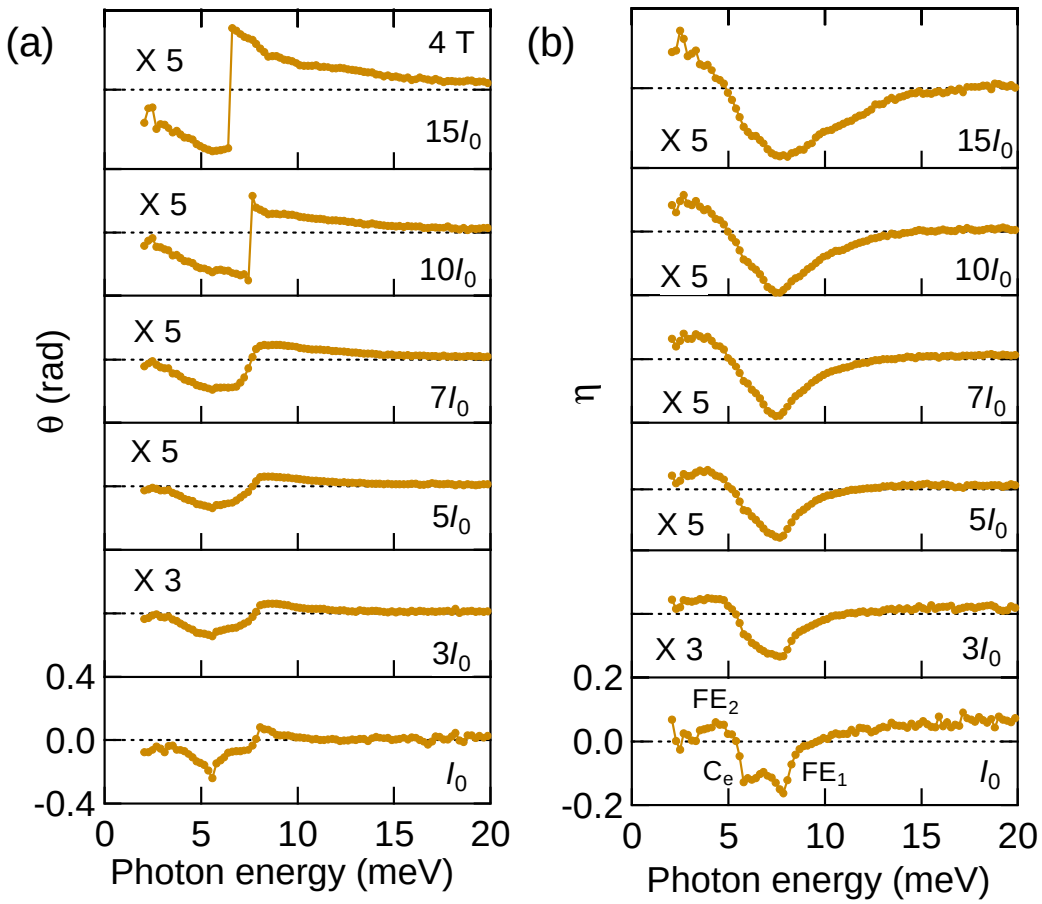

Figure 6.18: (a) The Faraday rotation spectra and (b) the ellipticity spectra under 4 T. The delay time was fixed at 5 ns and the lowest pump power I_0 was 5.3 μJ/cm^2.

Under 4 T, the peaks C_e and FE_1 exist at 5.8 and 7.9 meV, respectively. In a manner similar to the case of 7 T, we determined the ϵ_{xy} spectra and evaluated the density of the magnetoexcitons. Figure 6.19(a) and (b) represent the real part and (b) imaginary part of ϵ_{xy} determined from the Faraday rotation angle and ellipticity, respectively.

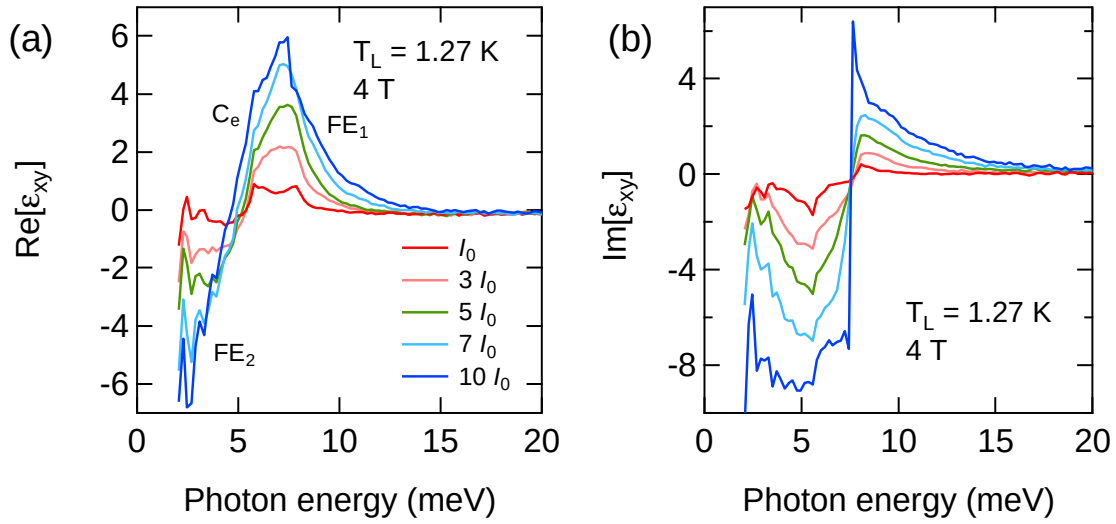

Figure 6.19: (a) The real part and (b) the imaginary part of ϵ_{xy} which is determined from the Faraday rotation angle and ellipticity spectra (Fig. 6.18).

Figure 6.20(a) shows the imaginary part of ϵ_{xy} under 4 T with different pump power. $I_0 = 5.3\ \mu\mathrm{J/cm^2}$. The closed squares denote the height of the peak $\mathrm{C_e}$. Then, the densities of the total e-h pairs, the free carriers, and the magnetoexcitons are evaluated as shown in Fig. 6.20(b) by using the same procedure with the case of 7 T. The maximum density of the magnetoexcitons achieved with current setup is estimated as $2.8 \times 10^{15}\ \mathrm{cm^{-3}}$. With this density under 4 T, the critical temperature of BEC is estimated to 0.9 K with the mass of 0.63 m_0 and the phase space density is calculated to be 0.25 with the e-h temperature of 2.3 K. Here, an ambiguity exists regarding the mass of the magnetoexciton. If the optical mass of the magnetoexciton is heavier than that of excitons under zero magnetic field, the total e-h pair density from sum rule might be underestimated. Since the spectral weight at high excitation regime is almost contributed by the magnetoexcitons, with the magnetoexciton mass of 0.63 m_0, the density of the magnetoexciton should be estimated about one order higher than present evaluation. Therefore, the determination of the optical mass of the magnetoexciton is crucial. To determine the mass of the magnetoexcitons, detailed investigations are required such as the rigorous evaluation by the absorbed photon flux of the optical pump with the reflection measurement.

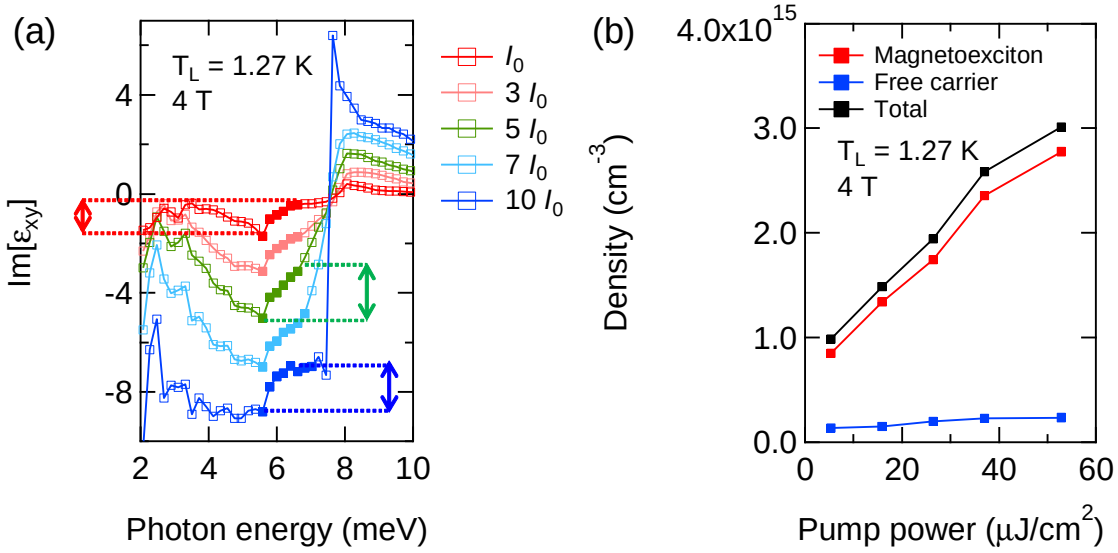

Figure 6.20: (a) The imaginary part of ϵ_{xy} under 4 T of different pump power with $I_0 = 5.3$ μJ/cm^2. The closed squares represent the height of the C_e. (b) The densities of total e-h pairs (black), the free carriers (blue), and the magnetoexcitons (red) as a function of the pump power.

The obtained maximum densities of the magnetoexcitons under 7 and 4 T are plotted in Fig. 6.21. Under the uniaxial stress, the accumulation of the relatively high density magnetoexcitons of 2.8×10^{15} cm^{-3} was realized without suffering from the formation of EHD. As shown by blue line in Fig. 6.21, the increase of critical temperature for the exciton BEC is expected under the magnetic field of 4 T by lifting the spin degeneracy. Under the magnetic field of 7 T, the critical temperature reduces due to the increase of the mass of the magnetoexcitons. With the density of 2.8×10^{15} cm^{-3}, the critical temperature of the exciton BEC is expected as 0.9 K. We also plot the exciton Mott density under zero magnetic field estimated from the Thomas-Fermi screening and the Bohr radius of excitons 106 Å as $N_{\mathrm{Mott}} = (0.23/a_B)^3$ [64]. The exciton Mott transition is expected to occur at the density 3 times larger than the realized magnetoexciton density. In reality, the exciton Mott density under the strong magnetic field should increase because of the shrinkage of Bohr radius of the magnetoexciton, which would further extend the BEC region to the higher density side. The investigation of the Mott transition under such a strong magnetic field is also crucially intriguing although we did not reach such high density condition in this study due to the limitation of the experimental condition.

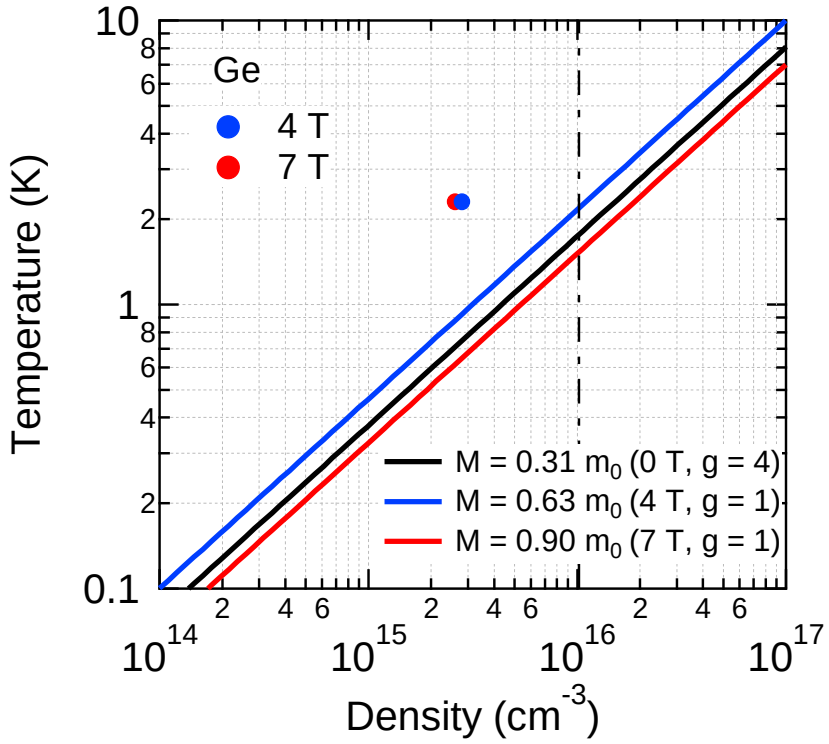

Figure 6.21: Experimental results in the phase diagram. Red and blue circles represent maximum density of the magnetoexcitons under 7 T and 4 T, respectively. Black, red, and blue solid lines represent the critical temperature of the magnetoexciton BEC under 0, 7, and 4 T. Black dotted-dashed line is the critical curve of the Mott transition.

6.9 Summary

In this Chapter, we performed the OPTP spectroscopy on the photoexcited e-h system in uniaxially-stressed Ge. For homogeneous distribution of photoexcited e-h system, we used the optical pump of the wavelength of 1450 or 1500 nm which is generated by OPA. By applying the uniaxial stress to the crystal along <111> direction, the formation of EHD was suppressed and the intra-transition of the magnetoexcitons is observed at low temperature. Furthermore, we investigated the high density region at low temperature by using OPTP spectroscopy to clarify the accumulation of the magnetoexcitons. However, in the case of the strong magnetic field regime and high density regime, the direct relation between the differential transmission spectra and absorption spectra becomes meaningless. Therefore, to investigate the high density region under the magnetic field, we performed the measurements of the Faraday rotation angle and the ellipticity spectra. From the polarization measurement, we calculated the off-diagonal component of the dielectric function

ϵ_{xy}. By using the sum rule for the real part of ϵ_{xy}, we evaluated the total e-h pair density. For the cyclotron resonance, we evaluated the density of the free carriers by the height scaling. From the difference of the total density to the free carrier density, the density of the magnetoexcitons was evaluated as 2.6×10^{15} cm^{-3} and 2.8×10^{15} cm^{-3} under 7 T and 4 T, respectively. In the case of 4 T, the phase space density of the magnetoexciton is calculated to be 0.25. Both electrons and holes should stay in the lowest Landau-level in the observed excitation density region. In such condition, the survey of the Mott transition is also highly intriguing from the viewpoint of excitonic insulator, which remains as a future work.

Chapter 7

Summary and Outlook

7.1 Summary

In this study, we performed the OPTP spectroscopy in the photoexcited e-h system in uniaxially-stressed Si and Ge to clarify their properties at low temperature. Also, for the spectroscopy study in such extreme conditions, we developed several experimental techniques. The achievements of this study are summarized as follow;

1 We investigated the magnetic field dependence on the excitons in Si. By using OPTP spectroscopy, the magnetic field effect on the excitons has been elucidated and the lifetime of the excitons in Si was determined by the quasi-CW OPTP spectroscopy. By using the quasi-CW pulse which is modulated by AOM as the optical pump, we developed the OPTP spectroscopy scheme, which can be utilized to the investigation of long temporal dynamics from sub-microseconds to milliseconds. Also, by the observation of intra-exciton transition, the lifetime of spin-forbidden exciton is measured directly.

2 We investigated the intermediate density region at low temperature in uniaxially-stressed Si. To perform the OPTP spectroscopy under an uniaxial stress, we developed the anvil cell. From the reduction of the SPR frequency of the EHD, we confirmed the e-h pair density inside EHD decrease from 3×10^{18} cm^{-3} to 3×10^{17} cm^{-3}, indicating that the more than 300 MPa of the uniaxial stress is applied successfully. Furthermore, the survival of the cold excitons is observed at 1.6 K. Through the spectral analysis with the EMT and multi-Lorentzian functions, the density of the excitons is estimated. Then, the excitons of 3×10^{15} cm^{-3} are evaluated to accumulate at such low temperature under an uniaxial stress and the magnetic field. In this condition, the phase space density is estimated to be 0.28.

3 We investigated the magnetoexcitons and the cyclotron resonance of the free carriers under the magnetic field in uniaxially-stressed Ge. By applying the uniaxial stress, the suppression of EHD and the intra-exciton transition are observed at 1.6 K. We evaluated the density of the magnetoexciton from the off-diagonal component of the dielectric function which was obtained by measurement the

polarization of the THz electric field. From the experimental result, the accumulation of the magnetoexcitons of 2.8×10^{15} cm^{-3} is evaluated under 4 T at the magnetoexciton temperature of 2.3 K. With this density, the critical temperature is estimated to 0.9 K, which is very close to the realized lowest temperature in present.

7.2 Outlook

In this study, the survival of the excitons at low temperature was realized by applying the uniaxial stress and the density of the excitons are investigated quantitatively.

From the experiment, the density of the magnetoexciton in uniaxially-stressed Ge was evaluated as 2.8×10^{15} cm^{-3} under 4 T at the magnetoexciton temperature of 2.3 K. With this density, the critical temperature of the exciton BEC is estimated to 0.9 K. This temperature may be realized. To verify the exciton BEC in Si, the realization of lower temperature below 0.7 K is required. To perform the OPTP measurement, we used optically-transparent windows at the cryostat. These windows prevent the cooling temperature because the radiations of bodies outside the sample chamber cannot be blocked. Indeed, by blocking the windows by aluminum sheet, the temperature reached at lower temperature. Therefore, the survey of materials which is transparent at only the used wavelength region is required.

Furthermore, high density region of e-h system in Ge under the magnetic field is crucially fascinating in terms of e-h BCS (excitonic insulator). In the metallic state above Mott density, within the presence of Coulomb correlation between the electron and the hole, by assumption of the pairing between the electron with momentum of $\mathbf{k}$ and the hole with momentum of $-\mathbf{k}$, the energy gap at the Fermi energies of the electron and the hole is predicted in a manner similar to the BCS theory. To elucidate this theme, a quantitative spectrum analysis under high density regime or the gain measurement are required.

Appendix A

Diffusion of excitons

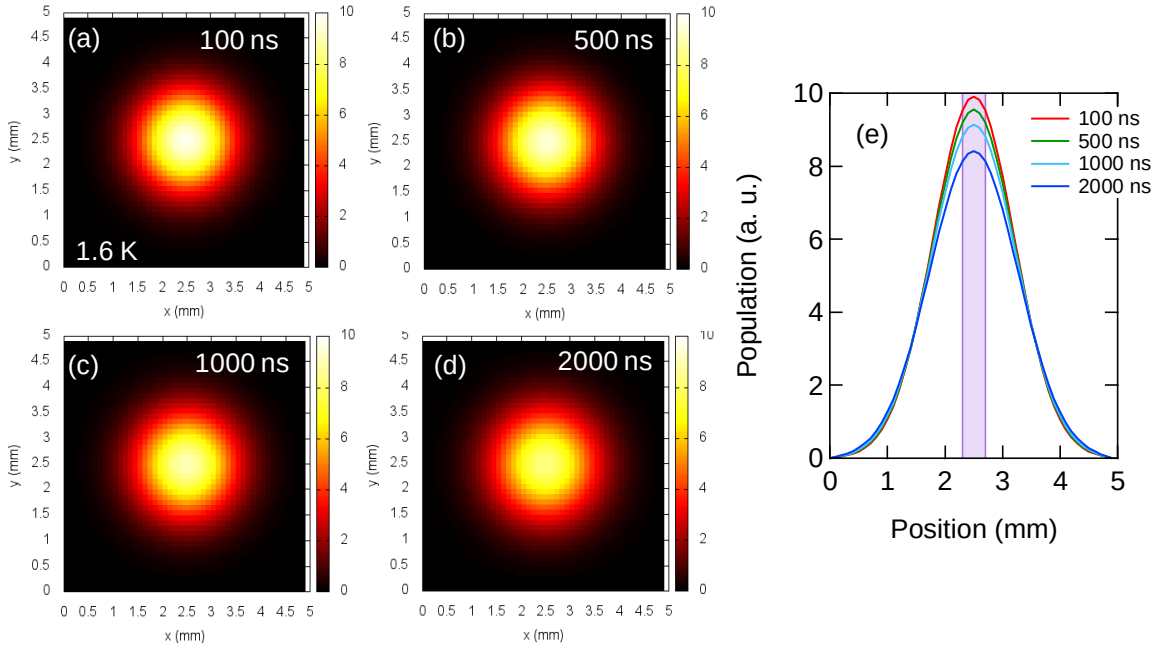

Figure A.1: Simulation of exciton diffusion at 1.6 K. (a)-(d) The in-plane distribution of excitons at different delay time. (e) Exciton population at x = 2.5 mm with different delay time. Shaded area represents the probe regime of 3 THz.

In the observation of long temporal dynamics such as the indirect excitons, the diffusion of exciton also be the origin of the temporal decay of the THz absorption. In this appendix, we consider the effect of the exciton diffusion.

The diffusion equation is written by

$$\frac{\partial f(r,t)}{\partial t} = D(T)\frac{\partial^2 f(r,t)}{\partial r^2} \ , \tag{A.1}$$

where $D(T)$ is the temperature-dependent diffusion coefficient of excitons. Here, we use the value of $D(T) = 300\ \mathrm{cm}^2 K^{1/2} \times T^{-1/2}$ which is reported by Tamor *et al.* [50].

From the temperature dependence of the diffusion coefficient, the effect of exciton diffusion be raised at low temperature. Therefore, we performed the simulation of exciton diffusion at 1.6 K by using eq. A.1. Figures (a)-(d) show the distribution of the photoexcited excitons at 100, 500, 1000, and 2000 ns after the optical pump. Here, we assumed the initial state as a Gaussian distribution with the radius of 2mm following to experimental condition. To evaluate the influence of diffusion on our experiment, we evaluate the decrease of the exciton density in the THz probe region. Figure (e) shows the cross-sections at y = 2.5 mm at each delay time. Since the energy of intra-exciton transition exists at 3 THz, we consider the spot size of the frequency of 3 THz as shown by shaded area in Fig. (e). Then the density loss of the excitons by diffusion is only 8 % at the delay time of 1 μs. This value does not impinge to our discussion. Therefore, we neglected the influence of the diffusion of the excitons in this study for the simplicity.

Reference

[1] N. F. Mott, The transition to metallic state. *Phil. Mag.*, **6**, 287 (1961).

[2] L. V. Keldysh and A. N. Kozlov, Collective Properties of Excitons in Semiconductors. *Sov. Phys. JETP*, **27**, 521 (1961).

[3] T. Suzuki and R. Shimano, Time-Resolved Formation of Excitons and Electron-Hole Droplets in Si Studied Using Terahertz Spectroscopy. *Phys. Rev. Lett.*, **103**, 057401 (2009).

[4] N. O. Lipari and A. Baldereschi, Energy Levels of Indirect Excitons in Semiconductors with Degenerate Bands. *Phys. Rev. B*, **3**, 2497 (1971).

[5] N. O. Lipari and M. Altarelli, Theory of Indirect Excitons in Semiconductors. *Phys. Rev. B*, **15**, 4883 (1977).

[6] W. F. Brinkman and T. M. Rice, Electron-Hole Liquids in Semiconductors. *Phys. Rev. B*, **7**, 1508 (1973).

[7] P. Vashishta and R. K. Kalia, Universal behavior of exchange-correlation energy in electron-hole liquid. *Phys. Rev. B*, **25**, 6492 (1982).

[8] P. Vashishta, S. G. Das, and K. S. Singwi, Thermodynamics of the Electron-Hole Liquid in Ge, Si, and GaAs. *Phys. Rev. Lett.*, **33**, 911 (1974).

[9] J. R. Chelikowsky and M. L. Cohen, Nonlocal pseudopotential calculations for the electronic structure of eleven diamond and zinc-blende semiconductors. *Phys. Rev. B*, **14**, 556 (1976).

[10] D. E. Aspnes and A. A. Studna, Direct observation of the E_0 and $\mathrm{E}_0 + \Delta_0$ transitions in silicon. *Sol. Stat. Commun.*, **11**, 1375 (1972).

[11] T. P. McLean, *Progress in Semiconductors*, Vol. 5 (A. F. Gibson, ed.) Heywood, London 1960.

[12] J. C. Hensel and G. Feher, Cyclotron Resonance Experiments in Uniaxially Stressed Silicon: Valence Band Inverse Mass Parameters and Deformation Potentials. *Phys. Rev.*, **129**, 1041 (1963).

[13] K. L. Shaklee and R. E. Nahory, Valley-Orbit Splitting of Free Excitons? The Absorption Edge of Si. *Phys. Rev. Lett.* **24**, 942 (1970).

[14] S. Zwerdling, B. Lax, L. M. Roth, and K. J. Button, Exciton and Magneto-Absorption of the Direct and Indirect Transitions in Germanium. *Phys. Rev.*, **114**, 80 (1959).

[15] S. H. Groves, C. R. Pidgeon, and J. Feinleib, Infrared Magnetoelectroreflectance in Ge, GaSb, and InSb. *Phys. Rev. Lett.*, **17**, 643 (1966).

[16] I. Balslev, Influence of Uniaxial Stress on the Indirect Absorption Edge in Silicon and Germanium. *Phys. Rev.*, **143**, 636 (1966).

[17] C. Herring and E. Vogt, Transport and Deformation-Potential Theory for Many-Valley Semiconductors with Anisotropic Scattering. *Phys. Rev.*, **101**, 944 (1956).

[18] S. M. Kelso, Energy- and stress-dependent hole masses in germanium and silicon. *Phys. Rev. B*, **25**, 1116 (1982).

[19] G. Dresselhaus, A. F. Kip, and C. Kittel, Cyclotron Resonance of Electrons and Holes in Silicon and Germanium Crystals. *Phys. Rev.*, **98**, 368 (1955).

[20] J. C. Hensel and K. Suzuki, Quantum resonances in the valence bands of germanium. II. Cyclotron resonances in uniaxially stressed crystals. *Phys. Rev. B* **9**, 4219 (1974).

[21] C. D. Jeffries, L. V, Keldysh, Modern problems in condensed matter sciences, volume 6, Electron hole droplets in semiconductors North-Holland Publishing Company, 1983.

[22] P. Vashishta, P. Bhattacharyya, and K. S. Singwi, Electron-hole liquid in many-band systems. I. Ge and Si under large uniaxial strain. *Phys. Rev. B*, **10**, 5108 (1974).

[23] A. H. Simon, F. M. Steranka, and J. P. Wolfe, Electron-hole liquid in germanium under high <111> stress. *Phys. Rev. B*, **40**, 4003 (1989).

[24] A. Forchel, B. Laurich, J. Wagner, W. Schmid, and T. L. Reinecke, Systematics of electron-hole liquid from studies of silicon with varying uniaxial stress. *Phys. Rev. B*, **25**, 2730 (1982).

[25] S. M. Kelso, Calculation of properties of the electron-hole liquid in uniaxially stressed Ge and Si. *Phys. Rev. B*, **25**, 7631 (1982).

[26] D. Labrie, V. A. Karasyuk, M. K. Nissen, Ya E. Pokrovskii, and M. L. W. Thewalt, Observation of autodissociating excited states of excitonic molecules. *Phys. Rev. B*, **47**, 1628 (1993).

[27] D. Labrie and T. Timusk, Far-infrared absorption spectrum of excitons in [111]-stressed germanium: High-stress limit. *Phys. Rev. B*, **27**, 3605 (1983).

[28] A. V. Chernenko and V. B. Timofeev, Stabilization of electron-hole liquid in uniaxially strained germanium in a strong magnetic field. *JETP*, **85**, 593 (1997).

[29] G. Feher, Electron Spin Resonance Experiments on Donors in Silicon. I. Electronic Structure of Donors by Electron Nuclear Double Resonance Technique, *Phys. Rev.*, **114**, 1219 (1959).

[30] V. B. Timofeev, V. D. Kulakovskii, and I. V. Kukushkin, Spin aligned exciton gas in uniaxially compressed Ge. *Physica B+C*, **117 − 118**, 327 (1983).

[31] R. J. Elliott and R. Loudon, Theory of the absorption edge in semiconductors in a high magnetic field. *J. Phys. Chem. Solids*, **15**, 196 (1960).

[32] M. Yamanaka, K. Muro, and S. Narita, Far-INfrared Magnetoabsorptions of Free and Bound Excitons in Highly [111]-Stressed Germanium. *J. Phys. Soc. Japan*, **44**, 1222 (1978).

[33] L. I. Schiff and H. Snyder, Theory of the Quadratic Zeeman Effect. *Phys. Rev.*, **55**, 59 (1939).

[34] I. V. Lerner and Yu. E. Lozovik, Mott exciton in a quasi-two-dimensional semiconductor in a strong magnetic field. *Zh. Eksp. Teor. Fiz.*, **78**, 1167 (1980). [*Sov. Phys. JETP.*, **51**, 588 (1980).]

[35] A. B. Dzyubenko, Intraexcitonic transitions in two-dimensional systems in a high magnetic field. *JETP Lett.*, **66**, 617 (1997).

[36] T. Ohyama, Far-infrared Magnetoabsorption of Exciton System in Silicon. *Phys. Rev. B*, **23**, 5445 (1981).

[37] H. Navarro and T. Timusk, Far-infrared Study of the Zeeman Effect of Indirect Excitons in Germanium. *Phys. Rev. B*, **25**, 1141 (1982).

[38] N. O. Lipari, M. Altarelli, and E. Tosatti Interpretation of far-infrared absorption spectra in germanium. *Solid State Commun.*, **21**, 979 (1977).

[39] H. Haug and S. W. Koch Quantum Theory of the Optical and Electronic Properties of Semiconductors. World Scientific Fifth Edition (2009).

[40] T. C. Killian, 1S-2S spectrum of a hydrogen Bose-Einstein condensate. *Phys. Rev. A*, **61**, 033611 (2000).

[41] Q. Wu and X. C. Zhang, 7 terahertz broadband GaP electro-optic sensor. *Appl. Phys. Lett.*, **70**, 1784 (1997).

[42] A. Leitenstorfer, S. Hunsche, J. Shah, M. C. Nuss, and W. H. Knox, Detectors and sources for ultrabroadband electro-optic sampling: Experiment and theory. *Appl. Phys. Lett.*, **74**, 1516 (1999).

[43] A. N. Pikhtin, V. T. Prokopenko, and A. D. Yas'kov, *Sov. Phys. Semicond.*, **10**, 1224 (1976).

[44] M. Born and E. Wolf, 7th Ed., Cambridge University Press

[45] A. Yariv and P. Yeh, Photonics, 6th Ed., Oxford University Press

[46] M. Tajima, Determination of boron and phosphorus concentration in silicon by photoluminescence analysis. *Appl. Phys. Lett.*, **32**, 719 (1978).

[47] R. B. Hammond, D. L. Smith, and T. C. McGill, Temperature Dependence of Silicon Luminescence Due to Splitting of the Indirect Ground State. *Phys. Rev. Lett.*, **35**, 1535 (1975).

[48] D. Labrie, M. L. W. Thewalt, I. J. Booth, and G. Kirczenow, Detailed Ground- and Excited-State spectroscopy of Indirect Free Excitons. *Phys. Rev. Lett.*, **61**, 1882 (1988).

[49] S. B. Nam, D. C. Reynolds, C. W. Litton, R.J. Almassy, and T. C. Collins, Free-Exciton Energy Spectrum in GaAs. *Phys. Rev. B*, **13**, 761 (1976).

[50] M. A. Tamor and J. P. Wolfe, Drift and Diffusion of Free Excitons in Si. *Phys. Rev. Lett.*, **44**, 1703 (1980).

[51] R. B. Hammond and R. N. Silver, Temperature dependence of the exciton lifetime in high-purity silicon. *Appl. Phys. Lett.*, **36**, 68 (1980).

[52] A. Haug, Auger recombination of electron-hole drops. *Sol. Stat. Commun.*, **25**, 477 (1978).

[53] P. L. Gourley and J. P. Wolfe, Properties of the electron-hole liquid in Si: Zero stress to the high-stress limit. *Phys. Rev. B*, **24**, 5970 (1981).

[54] W. Schmid, Formation and decay of electron-hole drops in Si. *Sol. Stat. Commun.,* **19**, 347 (1976).

[55] P. L. Gourley and J. P. Wolfe, Experimental determination of equilibrium constants for excitonic systems in stressed, ultrapure silicon. *Phys. Rev. B*, **25**, 6338 (1982).

[56] G. B. Norris and K. K. Bajaj, Exciton-plasma Mott transition in Si. *Phys. Rev. B*, **26**, 6706 (1982).

[57] T. Suzuki and R. Shimano, Cooling dynamics of photoexcited carriers in Si studied using optical pump and terahertz probe spectroscopy. *Phys. Rev. B*, **83**, 085207 (2011).

[58] G. A. Niklasson, C. G. Granqvist, and O. Hunderi, Effective medium models for the optical properties of inhomogeneous materials. *Appl. Opt.*, **20**, 26 (1981).

[59] K. Kolwas, S. Demianiuk, and M. Kolwas, Optical excitation of radius-dependent plasmon resonances in large metal clusters. *J. Phys. B*, **29**, 4761 (1996).

[60] C. D. Lorenz and R. M. Ziff, Precise determination of the critical percolation threshold for the three-dimensional “Swiss cheese” model using a growth algorithm. *J. Chem. Phys.*, **114**, 3659 (2001).

[61] K. Yoshioka, T. Ideguchi, and M. Kuwata-Gonokami, Laser-based continuous-wave excitonic Lyman spectroscopy in Cu_2O. *Phys. Rev. B*, **76**, 033204 (2007).

[62] 佐藤勝昭、光と磁気　改訂版. 朝倉書店, (2001).

[63] H. S. Bennett and E. A. Stern, Faraday effect in solids. *Phys. Rev.*, **137**, A448 (1965).

[64] J. B. Krieger and M. Nightingale, Dielectric Screening and the Mott Transition in Many-Valley Semiconductors. *Phys. Rev. B*, **4**, 1266 (1971).

Acknowledgements

I would like to express a sincere gratitude to associate professor R. Shimano who patiently encouraged me during this study as a supervisor. I would like to most gratefully acknowledge him for his energetic support. I heartily thank assistant professor R. Matsunaga for being provided some suggestions in procedures of data analysis. I would like to thank all members of Shimano group, Mr. F. Sekiguchi, K. Shibagaki, G. Yumoto, Y. I. Hamada, Ms. K. Sameda for fruitful discussions. Especially, the development of the pressure anvil cell was done in collaboration with K. Shibagaki, Also I thank to former members, Dr. Y. Ikebe, T. Suzuki, Mr. T. Ogawa, S. Tsubota. Finally I would like to thank my family for warm encouragements.